

CAPITAL UNIVERSITY OF SCIENCE AND
TECHNOLOGY, ISLAMABAD



A Study of Fluid Flow through
Deformable Porous Material and
Tissue using Mixture Theory
Approach

by

Umair Farooq

A thesis submitted in partial fulfillment for the
degree of Doctor of Philosophy

in the

Faculty of Computing

Department of Mathematics

2022

**A Study of Fluid Flow through Deformable Porous
Material and Tissue using Mixture Theory
Approach**

By

Umair Farooq

(DMT 151008)

Dr. Sharidan Shafie, Associate Professor

Universiti Teknologi Malaysia, Johor, Malaysia

Dr. Abdul Rahman bin Mohd Kasim, Associate Professor

Universiti Malaysia Pahang, Malaysia

Dr. Muhammad Sagheer

(Thesis Supervisor)

Dr. Muhammad Sagheer

(Head, Department of Mathematics)

Dr. Muhammad Abdul Qadir

(Dean, Faculty of Computing)

**DEPARTMENT OF MATHEMATICS
CAPITAL UNIVERSITY OF SCIENCE AND TECHNOLOGY
ISLAMABAD**

2022

Copyright © 2022 by Umair Farooq

All rights reserved. No part of this thesis may be reproduced, distributed, or transmitted in any form or by any means, including photocopying, recording, or other electronic or mechanical methods, by any information storage and retrieval system without the prior written permission of the author.

This dissertation is dedicated to my parents and family.



CAPITAL UNIVERSITY OF SCIENCE & TECHNOLOGY ISLAMABAD

Expressway, Kahuta Road, Zone-V, Islamabad
Phone: +92-51-111-555-666 Fax: +92-51-4486705
Email: info@cust.edu.pk Website: <https://www.cust.edu.pk>

CERTIFICATE OF APPROVAL

This is to certify that the research work presented in the thesis, entitled “**A Study of Fluid Flow through Deformable Porous Material and Tissue using Mixture Theory Approach**” was conducted under the supervision of **Dr. Muhammad Sagheer**. No part of this thesis has been submitted anywhere else for any other degree. This thesis is submitted to the **Department of Mathematics, Capital University of Science and Technology** in partial fulfillment of the requirements for the degree of Doctor in Philosophy in the field of **Mathematics**. The open defence of the thesis was conducted on **February 24, 2022**.

Student Name : Umair Farooq (DMT-151008)

The Examining Committee unanimously agrees to award PhD degree in the mentioned field.

Examination Committee :

(a) External Examiner 1: Dr. Shamsul Qamar
Professor
COMSATS University, Islamabad

(b) External Examiner 2: Dr. Ahmad Zeeshan
Associate Professor
IIU, Islamabad

(c) Internal Examiner : Dr. Abdul Rehman Kashif
Associate Professor
CUST, Islamabad

Supervisor Name : Dr. Muhammad Sagheer
Professor
CUST, Islamabad

Name of HoD : Dr. Muhammad Sagheer
Professor
CUST, Islamabad

Name of Dean : Dr. Muhammad Abdul Qadir
Professor
CUST, Islamabad

AUTHOR'S DECLARATION

I, **Umair Farooq (Registration No. DMT-151008)**, hereby state that my PhD thesis entitled, '**A Study of Fluid Flow through Deformable Porous Material and Tissue using Mixture Theory Approach**' is my own work and has not been submitted previously by me for taking any degree from Capital University of Science and Technology, Islamabad or anywhere else in the country/ world.

At any time, if my statement is found to be incorrect even after my graduation, the University has the right to withdraw my PhD Degree.



(Umair Farooq)

Dated: February, 2022

Registration No : DMT-151008

Plagiarism Undertaking

I solemnly declare that research work presented in this thesis titled "**A Study of Fluid Flow through Deformable Porous Material and Tissue using Mixture Theory Approach**" is solely my research work with no significant contribution from any other person. Small contribution/help wherever taken has been dully acknowledged and that complete thesis has been written by me.

I understand the zero tolerance policy of the HEC and Capital University of Science and Technology towards plagiarism. Therefore, I as an author of the above titled thesis declare that no portion of my thesis has been plagiarized and any material used as reference is properly referred/cited.

I undertake that if I am found guilty of any formal plagiarism in the above titled thesis even after award of PhD Degree, the University reserves the right to withdraw/revoke my PhD degree and that HEC and the University have the right to publish my name on the HEC/University website on which names of students are placed who submitted plagiarized work.

(Umair Farooq)

Registration No: DMT 151008

List of Publications

It is certified that following publication(s) have been made out of the research work that has been carried out for this thesis:-

1. **Umair Farooq** and J. I. Siddique, "Non-Newtonian Flow in Deformable Porous Media: Modeling and Simulations of Compression Molding Processes," *Journal of Porous Media*, vol. 23, pp. 465-476, 2020.
2. **Umair Farooq** and J. I. Siddique, "Compressive stress relaxation behavior of articular cartilage and its effects on fluid pressure and solid displacement due to non-Newtonian flow.," *Computer Methods in Biomechanics and Biomedical Engineering*, vol. 24, pp. 1-12, 2020.

Umair Farooq

(DMT151008)

Acknowledgement

I would like to thank my advisor Dr. Muhammad Sagheer for his guidance, suggestions, mentoring and assistance. His support and patient in preparing this dissertation were remarkable.

Special thanks goes to Drs. Javed Iqbal Siddique and Muhammad Afzal for their suggestions and moral support. I would like to thank my fellow students: Aftab Ahmed and Usman Ali. I would also like to thank my friend and family who helped and supported me. I would specially like to thank my parents, brothers and sister for all their guidance and emotional support.

Of course, I would like to deeply thank my wife and children for their support.

Umair Farooq

Abstract

This dissertation is an attempt to analyze the phenomenon involved in the flow of various fluids through deformable porous media. In particular, problems are modeled using continuum mixture theory approach. First, our focus would be on the study of compression molding process. A mathematical model has been developed to study non-Newtonian fluid flow through preimpregnated pile. The governing equation for solid volume fraction is solved numerically to highlight the rheological effects of fluid flow. Graphical illustrations indicate that shear-thinning and shear-thickening fluids induce the increase in solid volume fraction. But, final state of solid volume fraction is homogeneous for shear-thickening fluid as compared to the shear-thinning fluid. Furthermore, ion-induced deformation of articular cartilage due to non-Newtonian fluid flow is investigated. Ionic effects are incorporated with solid stress for biphasic modeling of tissue. Normalized quantities are used to non-dimensionalize the equations for ion-concentration, fluid pressure and solid displacement. First, analytical solution for ion-concentration has been presented. Coupled system of equations for solid displacement and fluid pressure produces complexity. This complexity is handled using numerical technique; Method of Lines. Numerical results indicate that the shear-thickening fluid induces more solid deformation but less fluid pressure as compared to the shear-thinning fluid. In addition to this, a mathematical model has been developed to study rheological effects on compressive stress-relaxation behavior of soft biological tissue. Biphasic mixture theory is incorporated with strain-dependent permeability. Suitable quantities are used to non-dimensionalize the coupled system of equations of solid displacement and fluid pressure. Numerical results show that the solid deformation increases with increase in power-law index. Results also indicate that linear permeability induces more deformation as compared to the strain-dependent nonlinear permeability. Finally, based on the geometry of previous problem, a mathematical model has been developed to study deformation of the biological tissue due to flow of electrically conducting fluid from it. In the presence of Lorentz forces, biphasic mixture theory is incorporated with strain-dependent permeability. Complexity of governing equations is treated numerically. Graphical illustrations show

that solid displacement decreases but fluid pressure increases by increasing the strength of magnetic parameter. These results are more profound for the fast rate of compression as compared to the slow rate of compression.

Contents

Author's Declaration	iv
Acknowledgement	vii
Abstract	viii
List of Figures	xiii
List of Tables	xvii
Symbols	xviii
1 Introduction	1
1.1 Introduction	1
1.1.1 Problem Statement	2
1.1.2 Objective and Scope	3
1.1.3 Significance of Study	3
1.2 Historical Background	3
1.3 Thesis Outline	18
2 Preliminaries	20
2.1 Introduction	20
2.2 Porous Material	20
2.3 Porosity	21
2.4 Darcy's Law	22
2.4.1 Permeability	23
2.5 Cell	23
2.6 Tissue	24
2.7 Magnetohydrodynamics	25
2.8 Preimpregnated Materials	26
2.9 Heaviside Step Function	26
2.10 Fluid and Its Classification	26
2.11 Mixture Theory	29

2.12	Power-law Fluid Modeling for a Biphasic Mixture of Solid Phase and a Fluid Phase	32
2.13	Numerical Method	35
2.13.1	Method of Lines	35
2.13.2	<i>pdepe</i>	38
3	Non-Newtonian Flow in Deformable Porous Media: Modeling and Simulations of Compression Molding Processes	39
3.1	Introduction	39
3.2	Mathematical Modeling in Eulerian formalism	40
3.3	Lagrangian One-Dimensional Model	44
3.4	Non-Dimensionalization	46
3.5	Pressure and Velocity Driven Dynamics	48
3.6	Results and Discussion	51
3.7	Conclusion	60
4	Ion-induced Swelling Behavior of Articular Cartilage due to Non- Newtonian flow and its Effects on Fluid Pressure and Solid Dis- placement	62
4.1	Introduction	62
4.2	Model Development	63
4.3	One-Dimensional Mathematical Model	66
4.4	Non-dimensionalization	68
4.5	Solution Procedure	71
4.6	Results and Discussion	75
4.6.1	Ion Concentration Profile	75
4.7	Conclusion	80
5	Compressive Stress Relaxation Behavior of Articular Cartilage and its Effects on Fluid Pressure and Solid Displacement due to non-Newtonian Flow	83
5.1	Introduction	83
5.2	Mathematical Formulation	84
5.3	Initial and Boundary Conditions	90
5.4	Non-Dimensionalization	90
5.5	Solution Procedure	93
5.6	Results and Discussion	94
5.7	Concluding Remarks	101
6	Flow-Dependent Compressive Stress-Relaxation Behavior of Ar- ticular Cartilage with MHD Effects	103
6.1	Introduction	103
6.2	Mathematical Formulation	104
6.3	Non-Dimensionalization	112
6.4	Solution Procedure	113

6.5	Results and Discussions	115
6.6	Conclusion	121
7	Conclusion and Future Work	123
7.1	Conclusion	123
7.1.1	Non-Newtonian Flow in Deformable Porous Media: Modeling and Simulations of Compression Molding Processes . . .	124
7.1.2	Ion-induced Swelling Behavior of Articular Cartilage due to Non-Newtonian flow and its Effects on Fluid Pressure and Solid Displacement	124
7.1.3	Compressive Stress Relaxation Behavior of Articular Cartilage and its Effects on Fluid Pressure and Solid Displacement due to non-Newtonian Flow	125
7.1.4	Flow-Dependent Compressive Stress-Relaxation Behavior of Articular Cartilage with MHD Effects	125
7.2	Future Direction	126
	Bibliography	127
A	Magnetohydrodynamics (MHD) Equations for a Biphasic Mixture of Solid Phase and a Fluid Phase	147

List of Figures

2.1	Schematic diagram of a porous material [146].	21
2.2	Types of animal tissue [148].	25
2.3	Schematic diagram of a power law fluid presented in a generic graph of shear stress τ against gradient du/dy [8].	28
2.4	A comparison between MOL and analytical solution of the parabolic PDE (2.39). Exact (solid line) and numerical (dashed line) are plotted to compare two solutions.	37
3.1	Evolution of a system. Eulerian model is formulated in the reference frame, the x -axis. The origin $x = 0$ corresponds to the piston position at time $t = 0$. L^* represents the initial height of preimpregnated (prepreg) layers, and $s(t)$ be the piston position at time $t > 0$	42
3.2	Pressure applied to a piston as a function of dimensionless T	49
3.3	Velocity of a piston V as a function of the dimensionless time T	50
3.4	Solid volume fraction ϕ against space variable Y using $P_1(T)$ when $n = 1$	50
3.5	Solid volume fraction ϕ against space variable Y and time T using $V_3(T)$ when power-law index $n = 1$	51
3.6	Solid volume fraction ϕ against space variable Y and time T using $P_1(T)$ when power-law index $n = 0.90$	52
3.7	Solid volume fraction ϕ against space variable Y and time T using $P_1(T)$ for power-law index $n = 1.1$	52
3.8	Solid volume fraction ϕ against space variable Y and time T using $P_2(T)$ for power-law index $n = 0.90$	53
3.9	Solid volume fraction ϕ against space variable Y and time T using $P_2(T)$ for power-law index $n = 1.1$	53
3.10	Solid volume fraction ϕ against space variable Y and time T using $P_3(T)$ for power-law index $n = 0.90$	54
3.11	Solid volume fraction ϕ against space variable Y and time T using $P_3(T)$ for power-law index $n = 1.1$	55
3.12	Solid volume fraction ϕ against space variable Y and time T using $V_1(T)$ for power-law index $n = 0.80$	55
3.13	Solid volume fraction ϕ against space variable Y and time T using $V_1(T)$ for power-law index $n = 1.3$	56
3.14	Solid volume fraction ϕ against space variable Y and time T using $V_2(T)$ for power-law index $n = 0.90$	57

3.15	Solid volume fraction ϕ against space variable Y and time T using $V_2(T)$ for power-law index $n = 1.1$	57
3.16	Solid volume fraction ϕ against space variable Y and time T using $V_3(T)$ for power-law index $n = 0.90$	58
3.17	Solid volume fraction ϕ against space variable Y and time T using $V_3(T)$ for power-law index $n = 1.1$	58
4.1	Schematic diagram of a rectangular strip of cartilage specimen under continuous supply of salt solution. This geometry shows the cartilage dimensions (h , w and ℓ) along the planar coordinates \bar{x} , \bar{y} and \bar{z} respectively.	63
4.2	Interstitial Fluid Pressure $p(x, t)$ against distance x when power law index $n = 1.0$ at time $t = 0.25$	74
4.3	Theoretical prediction of the ion concentration as a function of distance x at time $t = 0.1, 0.3, 1.0, 4$. Exact (solid line) and numerical (dashed line) solution are plotted for ion-concentration to compare two solutions.	76
4.4	Solid displacement $u(x, t)$ against distance x for various power-law indices at time $t = 0.1$	77
4.5	Solid displacement $u(x, t)$ against distance x for permeability parameters $m = 0, 1$ when power-law index $n = 0.7$ at time $t = 0.1$	77
4.6	Solid displacement $u(x, t)$ against distance x for permeability parameters $m = 0, 1$ when power-law index $n = 1.5$ at time $t = 0.1$	78
4.7	Solid displacement $u(x, t)$ against distance x when power law index $n = 0.7$ at times $t = 0.1, 1.0$	78
4.8	Solid displacement $u(x, t)$ against distance x when power law index $n = 1.5$. at times $t = 0.1, 1.0$	79
4.9	Interstitial Fluid Pressure $p(x, t)$ against distance x when power-law index $n = 0.7$ at times $t = 0.1, 1.0$	80
4.10	Interstitial Fluid Pressure $p(x, t)$ against distance x when power law index $n = 1.5$ at times $t = 0.1, 1.0$	80
5.1	Illustration of a test related to confined compression stress-relaxation. During time $0 \leq \bar{t} \leq t_0$, a ramp compression is applied at the cartilage surface which is confined on the lateral surface, so that deformation occurs only in the \bar{x} direction.	84
5.2	Graphical representation of a ramp displacement.	85
5.3	Solid displacement $u(x, t)$ against distance x when power-law index $n = 1.0$ at time $t = 0.5$	94
5.4	Dimensionless Solid displacement $u(x, t)$ profile vs distance x for power law index $n = 0.5, n = 1$ and $n = 1.5$ during the fast rate of compression for linear permeability ($m = 0$) at time $t = 1$	96
5.5	Dimensionless Solid displacement $u(x, t)$ profile vs distance x for power law index $n = 0.5, n = 1$ and $n = 1.5$ during the slow rate of compression for linear permeability ($m = 0$) at time $t = 1$	96

5.6	Solid displacement vs distance for various permeability parameters when $n = 0.5$ during fast rate of compression ($R^2 = 0.25$)	97
5.7	Solid displacement vs distance for various permeability parameters when $n = 1.5$ during fast rate of compression ($R^2 = 0.25$).	97
5.8	Dimensionless Fluid Pressure $p(x, t)$ profile vs distance x for power law index $n = 0.5$, $n = 1$ and $n = 1.2$ during the fast rate of compression ($R^2 = 0.5$) for linear permeability ($m = 0$) at time $t = 0.01$	98
5.9	Dimensionless Fluid pressure $p(x, t)$ profile vs distance x for power law index $n = 0.5$, $n = 1$ and $n = 1.2$ during the slow rate of compression ($R^2 = 1.1$) for linear permeability ($m = 0$) at time $t = 0.01$	98
5.10	Solid displacement versus distance for power law index $n = 0.5$ for linear permeability ($m = 0$) at $t = 0.1, 0.4$ during fast rate of compression.	99
5.11	Solid displacement versus distance for power law index $n = 1.3$ for linear permeability ($m = 0$) at $t = 0.1, 0.4$ during fast rate of compression.	99
5.12	Fluid Pressure versus distance for power law index $n = 0.5$ for linear permeability ($m = 0$) at $t = 0.1, 0.4$ during fast rate of compression.	100
5.13	Fluid Pressure versus distance for power-law index $n = 1.3$ for linear permeability ($m = 0$) at $t = 0.1, 0.4$ during fast rate of compression.	100
6.1	Schematic representation of one-dimensional confined compression used for the stress-relaxation test.	104
6.2	Graphical representation of a ramp displacement.	105
6.3	Solid displacement as a function of x at time $t = 0.25$ during fast rate of compression ($R^2 = 0.25$) when $M = 0$	115
6.4	Solid displacement as a function of x for different values of M during fast rate of compression ($R^2 = 0.25$) at $t = 0.25, 0.5, 1.0$ when $m = 0$	116
6.5	Solid displacement as a function of x for different values of M during slow rate of compression ($R^2 = 4$) at $t = 0.25, 0.5, 1.0$ when $m = 0$	117
6.6	Solid displacement as a function of x for various values of permeability parameter m during fast rate of compression ($R^2 = 0.25$) at $t = 0.25, 0.5$ when $M = 0.2$	117
6.7	Solid displacement as a function of x for various values of permeability parameter m during slow rate of compression ($R^2 = 4$) at $t = 0.25, 0.5$ when $M = 0.2$	118
6.8	Fluid pressure as a function of x for various values of magnetic parameter M during fast rate of compression ($R^2 = 0.25$) at $t = 0.1$ when $m = 0$	119
6.9	Fluid pressure as a function of x for various values of magnetic parameter M during slow rate of compression ($R^2 = 1.2$) at $t = 0.01$ when $m = 0$	119

6.10	Fluid pressure as a function of x for various values of time t during fast rate of compression ($R^2 = 0.25$) when $M = 0.1$	120
6.11	Fluid pressure as a function of x for various values of time t during slow rate of compression ($R^2 = 1.1$) when $M = 0.1$	120

List of Tables

2.1	Power-law fluid model	29
2.2	Maximum absolute error between MOL solution and exact solution of parabolic PDE (2.39) for different spatial nodes at time $t = 1.5$. .	38

Symbols

\mathbf{b}	net body force
C	molar concentration of sodium chloride (NaCl)
C_o	step size in NaCl concentration on cartilage sample
D	Diffusion coefficient of salt in soft tissue
H_A	aggregate modulus of solid
$H(t)$	unit step function
h	thickness of tissue specimen
\mathbf{I}	identity tensor
κ	hydraulic permeability of articular cartilage
κ_o	undeformed permeability
ℓ	length of cartilage specimen
M	dimensionless magnetic parameter
m	permeability perimeter
n	power law index
p	interstitial fluid pressure
r	ratio of fluid volume fraction to solid volume fraction
\mathbf{T}^f	stress tensor of fluid phase
\mathbf{T}^s	stress tensor of solid phase
t	time
u	solid displacement
V_v	volume of void space in a porous material
V_T	Total volume of porous material
\mathbf{v}^f	velocity of fluid phase

\mathbf{v}^s	velocity of solid phase
w	width of cartilage specimen
α	solid to liquid volume ratio
α_c	coefficient of isotropic chemical contraction
ϕ	solid volume fraction
ϕ_p	porosity
ρ^β	density of β phase
λ_s, μ_s	Lame's stress constants

Chapter 1

Introduction

1.1 Introduction

In this dissertation, flow-induced deformation in a deformable porous media is investigated using continuum mixture theory approach. Our focus was on the study of the compression molding process, ion-induced swelling and stress relaxation behavior of articular cartilage. In this study, deformable porous materials such as preimpregnated pile and articular cartilage are modeled as nonlinear material composed of a fluid and a solid phase. Apart from continuum mixture theory approach to model multiphase systems, there are many theoretical frameworks such as pore scale network modeling, thermomechanics, membrane theory, finite elasticity, the bundle of tubes approach, growth and remodeling and viscoelasticity were devised to study the fluid flow in porous materials. Humphrey [1] has given an excellent description of these theories in a review paper. He also mentioned the past successes in biomechanics of soft biological tissues and identifies future work in this area. He emphasized on the need for comprehensive and new theoretical frameworks, including computational approaches for modeling rheological fluid flow through biological tissues by considering it as a porous material.

Contemporary studies [2–4] describe the behavior of rheological complex fluid flow through a porous media. From these studies, several attempts have been made

to study non-Newtonian fluid flow through porous media [5–7]. Non-Newtonian fluid flow involves a variety of highly complex phenomena and proper description requires sophisticated mathematical modeling. Further complications are added to the phenomenon due to the non-Newtonian fluid flow through porous media. Sochi [8] highlighted applications of non-Newtonian fluid flow in porous media such as filtration of polymer solutions, removal of fluid pollutants from soil, and enhanced oil recovery from underground reservoirs.

Continuum mixture theory is used to develop mathematical models for flow of non-Newtonian and electrically conducting fluids through porous materials given in this thesis. It is worth mentioning here that Siddique and Aderson [9, 10] were the first ones to develop the power-law fluid model in combination with the mixture theory approach. Keeping in view the importance of non-Newtonian fluid in medicine and industry, the purpose of this dissertation is to examine the rheological effects on different classes of porous media. In the following, we have presented the problem statement, objective and scope with significance of the study. This is followed by a detailed discussion of each chapter in Section 1.3.

1.1.1 Problem Statement

In this dissertation, mathematical models have been developed for flow of fluids through deformable porous media by using continuum mixture theory with various laws of Physics, i.e., conservation of mass, conservation of momentum and Darcy, etc. In particular, models are formulated for flow of non-Newtonian and electrically conducting fluids through articular cartilage and preimpregnated materials. Biphasic mixture theory is used to handle mixture of fluid and solid which gives the system of dimensional partial differential equations (PDEs) in terms of solid volume fraction, fluid pressure and solid deformation. Suitable normalized parameters are used to non-dimensionalize the governing systems of equations. Moreover, MATLAB built-in function *pdepe* (partial differential equation parabolic elliptic) and Method of Lines are employed to solve these equations. Graphical illustrations

have been presented for power-law index, permeability parameter and magnetic parameter.

1.1.2 Objective and Scope

The aim of this research is to develop and analyze theoretical mathematical models that describe the effects of flow of non-Newtonian and electrically conducting fluids through deformable porous materials. In particular, this permits us to connect solid deformation of deformable porous material with the fluid flow. It has also been intended to use knowledge gained from previous studies based on models that were developed using continuum mixture theory approach. In this regard, mathematical models have been formulated to analyze fluid flow through preimpregnated pile and articular cartilage. Solution to these models can be achieved by using numerical methods because of the complexity of equations. This theoretical study can be used to explore various industrial and biological applications involving fluid flow in porous materials.

1.1.3 Significance of Study

The phenomenon of solid deformation in porous materials due to fluid flow is of particular significance due to its role in agricultural and geophysical processes (for example, flooding and land sliding), and modern technological applications (for example, cleaning, medical diagnosing and filtering). Furthermore, by considering the various fluid models and the articular cartilage as a porous material, study encompasses the industry as well as biomechanics.

1.2 Historical Background

Porous material deforms when fluid flows through it. Due to deformation, properties of porous material such as permeability and porosity change which ultimately

change the passage of fluid flow through porous material. This procedure creates a complex coupling between fluid and porous material. This phenomenon can be observed in various industrial and biological applications such as compression molding [11], mechanical properties of asphalt concrete [12], fluidized beds [13], capillary rise [9] and deformation of tissue due to fluid flow [14], etc. Usually, this phenomenon can be modeled mathematically using continuum mixture theory. Basic assumption of mixture theory is that each constituent of a mixture is continuous and present at each point of mixture at each instant of time. Fick [15] was the first one who laid down the foundation of mixture theory. Stefan [16] and Darcy [17] extended the work of Fick. Truesdell and Noll [18] improved the previous work on mixture theory by using basic principles of continuum mixture and included equation of conservation of mass for different constituents of mixture. In fact, theory of Truesdell described the momentum and mass transfer between the different constituents of the mixture. Muller [19] extended the mixture theory for Newtonian fluid in thermodynamics version and developed the entropy and energy equation for a mixture. Atkin and Craine [20] presented revolutionary work in the review paper by deriving the entropy inequality, momentum, and energy equations along with the equation of conservation of mass. It is worth mentioning here that Bowen [21] and Bedford and Drumheller [22] have given comprehensive review on mixture theory. Moreover, Rajagopal and Tao [23] have derived different conservation laws and analyzed several examples using mixture theory in a famous book on mechanics of mixtures. All of the above mentioned studies were lacking the application to non-Newtonian fluid flow in a porous media. Non-Newtonian fluid flow in porous materials has various biological and industrial applications, such as compression molding process [24], oil recovery process [25], petroleum engineering [26] and ion-induced swelling behavior of soft tissue [27]. Deformation in porous materials due to non-Newtonian flow can be handled by using continuum mixture theory approach. For understanding the non-Newtonian fluid flow in detail, previous studies need attention.

Due to complications, almost all the experimental and theoretical studies encompass the one-dimensional flow of non-Newtonian fluid. Savins [28] presented a

summary on non-Newtonian fluid flow through diverse types of porous media. For different types of non-Newtonian fluids, Scheidegger [29] and Bird *et al.* [30] presented many rheological models. Gogarty [31] contributed the great work on flow of non-Newtonian fluid through porous media and showed experimentally that permeability decreases with pseudoplastic fluid flow and stabilizes with flow. He also showed that for a given porous media, high shear rate exists at the lower permeability and caused low effective viscosity. Using lubrication assumption, Ikoku and Ramey [32], and Odeh and Yang [33] were first one to give analytical solutions for a slightly compressible non-Newtonian unsteady fluid flow. Ikoku and Ramey [34], Lund and Ikoku [35], Ikoku [36], Gencer and Ikoku [37] and Vongvuthipornchai and Raghavan [38] have applied their solutions to different complicated problems. During recovery operations, Poolen and Jargon [39] have investigated the injection of non-Newtonian fluid into a reservoir using power-law model. In particular, fluid considered is shear-thinning fluid. Equations presented are for radial, linear and steady-state flow. Nonlinear equations are obtained after mathematical manipulation. Graphical illustrations are used to show finite difference solutions.

Kefayati *et al.* [40] used a power-law index to develop a lattice Boltzmann mathematical model for the flow of thermal incompressible non-Newtonian fluids through porous media. Results are obtained for porous cavity and also comparison has been presented with previous studies. Yadav and Verma [41] developed a model for the flow of Newtonian as well as non-Newtonian fluids through the specially designed cylindrical pipe. They used Brinkman and Stoke's equation, and Eringen equation to model the problem. The effects of various parameters such as viscosity ratio, micropolar parameter and permeability parameter on the flow rate and linear flow velocity are illustrated graphically. Comparison has been presented with the previous studies. Cheng *et al.* [42] used non-Newtonian rheology and theory of electrokinetic transport to model non-Darcy fluid flow through porous media. Numerical results show that effect of various parameters such as yield stress, capillary radius and zeta potential is significant at high-pressure gradient as compared to low-pressure gradient. The Non-Newtonian flow-foam behavior in porous materials has been studied experimentally by Omirbekov *et al.* [43]. They observed

that apparent viscosity of foam increases with increase in permeability of porous material. Above mentioned studies can be further extended for magnetohydrodynamics fluids. We now turn our attention to the specific type of porous material, i.e., deformable porous material.

As deformable porous material deforms due to flow. In various fields, deformable porous material arises including soil science [44–46], paper and printing [47, 48], geophysics [49], snow physics [50] and chemistry [51]. Biot’s [52] work on soil settlement describes an early mathematical model of deformable porous media. As due to fluid flow, solid deformation occurs in deformable media. So, he used Darcy’s law to describe fluid flow coupled with a linear elasticity model to observe solid deformation. He developed a mathematical model based on one-dimensional as well as two-dimensional solid consolidation and solutions were obtained for permeable [53] and impermeable [54] rectangular loads. Process of a roll applicator is used for coating flows in the printing and paper industry which has been mathematically modeled by Chen and Scriven [47]. Their model not only addresses the Newtonian fluid flow driven by external or capillary pressure in the deformable receiving porous medium but also treats the effects of trapped air and air compression in the substrate. Manzoli *et al.* [55] used finite elements to mathematical model injection of fluid at high pressure in deformable porous material. Model handled the high speed flow of fluid with deformation of material. Comparison has been presented with analytical solution. Mou *et al.* [56] discussed the effects of heat and mass transfer on the deformable porous media. Complex model was developed using momentum balance equation and stress differential equations. Results were obtained using finite element method and comparison with experiments has been presented. Bui and Nguyen [57] developed computational based and mesh-free numerical technique to study fluid flow in a deformable porous material. Their proposed model can handle the seepage flows. Predicted results show excellent agreement with analytical and experimental results. We now turn our attention to the process which incorporates fluid flow through deformable porous material.

An important process called compression molding is used for manufacturing of composite materials such as plastic, fiberglass, concrete and reinforced concrete and mud bricks. Manufacturing of composite material is more an art than engineering [58, 59]. Flow of fluid in deformable porous material is involved in this process. Several fibers are preimpregnated with a certain quantity of fluid, distributed in one-directional or multidirectional piles. Moreover, these piles are placed in porous mold. The mixture of deformable porous material and fluid is heated and then compressed. Piston is used to compress the deformable material that produces fluid flow due to squeezing in the pile which pushes the fluid out of the pile which in turn increases solid volume fraction [60–62]. To understand process of compression molding, fibre-reinforced composites need attention.

Fibre-reinforced composites have received attention in the last couple of decades due to their excellent mechanical properties, lower carbon footprint, and economic fuel consumption. For typical automotive components where low cost, fast cycle time, and large volume are desired, thermoplastic resin and chopped reinforcing fibres are increasing in popularity [63–65]. Usually, these types of materials are made using resin transfer molding, compression molding, and injection molding methods [66, 67]. Of these methods, compression molding is a suitable method for the manufacturing of composite materials as it offers the great potential to maintain longer fibers [68–70]. For the fibre-reinforced charge, there are two formats in the compression molding method, i.e., (1) sheet charge, and the bulk charge. In sheet charge, mats are formed by using dispersed chopped fibers on the resin sheets. Moreover, a single or twin screw low shear plasticator is used to make bulk charge; the required size of bulk comes out from the plasticator is collected and placed in die for the compression molding process. Computer-aided engineering (CAE), a numerical simulation has received attention due to increase use of fiber-reinforced components. In the last three decades, many researchers used CAE simulations to study fiber-reinforced polymer materials. Osswald and Charles [71] developed the model for the compression molding process. The model consists of the boundary element equations and on the assumption that fluid is isothermal

Newtonian. The accuracy of the numerical results is discussed by comparing them with experimental results.

Advani [72] developed CAE simulation for compression molding process. Numerical results are verified by comparing them with experimental results. Due to these remarkable research activities, a computer program Cadpress [73] was developed. Cadpress used hydrodynamic model [74], which was appropriate for sheet molding compound (thermoset resin+ discontinues fibre). Ahmed and Alexandrou [75] investigated the compression molding of viscoelastic polymers using Eulerian-Lagrangian approach. Equations of motion considered for analysis were two-dimensional and unsteady. Constitutive behavior of the polymers is described by White-Metzner model. Method of mixed Galerkin finite elements is used to obtain a solution of the problem. Smith *et al.* [76] modeled manufacturing of plastic components using compression molding and injection processes. Galerkin finite element method and isothermal Hele-Shaw flow analysis are employed to form nonlinear equations for the polymer melt pressure field and, Newton-Raphson method is used to solve these equations. Kim *et al.* [77] analyzed compression molding process of center-gated disc by developing physical model and numerical analysis. Numerical results showed that with the rise in melt temperature birefringence becomes smaller and significantly affected by mold temperature and flow rate. Dweib and Bradaigh [78] investigated extensional as well as shearing behavior under compression molding of glass mat-thermoplastic material using a model specifically developed for no-slip wall conditions. Compression molding is modeled on assumptions that it is a combination of shearing and extensional flow and two shear and extensional velocities were determined. Allen and Jain [79] investigated the manufacturing of precision optics using compression molding of glass aspherical lenses. Finite element method not only used to create numerical models but also used for analyzing molding processes. Experimental results predicted that this process can be used for production of precision optical components. Comparison of predicted results with experimental results shows that the finite element method can be used as a tool for process analysis.

Compression molding process is used to manufacture sheet molding compounds. Meyer *et al.* [80] adopted direct bundle simulation (on a specimens having double curved geometry) to model this process. Behrens [81] described the manufacturing of glass mat thermoplastics using compression molding. Their work handled the temperature distribution and interaction between materials involved in this process. Jayavardhan *et al.* [82] discussed the manufacturing of glass microballoon using compression molding. They observed that the increase of filler content decreases the tensile strength. Jeong *et al.* [83] discussed the manufacturing of carbon fiber reinforces plastic using process of preimpregnated compression molding. However, this process produces defects involving voids and micro grooves. To avoid these defects, their main focus would be on the manufacturing of a roof panels using vacuum-assisted preimpregnated compression molding. Wei *et al.* [84] used Phan-Thien-Tanner model to study polymer melt flow in compression molding process. Shear-thinning of polymer has been described by using analytical stress solution. Experiments are conducted to check the validity of solution. Chuaynukul *et al.* [85] presented the comparison between solution casting and compression molding methods. They used both methods for the preparation of fish and bovine gelatins. Comparison shows that gelatins films made from casting method had higher yellowness, water-vapor barrier and extensibility as compared to those films made from process of compression molding.

Compression molding of deformable porous material preimpregnated with liquid is difficult to analyze. As material deforms due to which permeability of material changes, so mixture theory is the suitable choice for analyzing the process. Farina *et al.* [11] used mixture theory to investigate the compression molding process in which flow in the deformable porous material is involved. In this problem, piston is used to compress preimpregnated layers of deformable porous material. First, the problem was modeled using the Eulerian frame and then the problem is formulated in Lagrangian formalism. Dynamics of the system is controlled either by applied pressure on the piston or by the velocity of the piston. Moreover, mixture theory is also applicable to soft biological tissues as these tissues behave like deformable porous material.

The journey of studying soft biological tissues using mixture theory is dated back to the work of Kenyon [86–88], who investigated the radial flux of Newtonian fluid flow through a porous cylinder following a mathematical model of fluid flow through arterial wall. Similarly, Jayaraman [89] investigated theoretically water transport in arterial wall with the assumption of constant permeability. Jain and Jayaraman [90] studied the similar problem by considering the two layers for Newtonian fluid flux through an artery. Similarly, Klanchar and Tarbell [91] investigated the water transport in arterial tissue under the assumption that permeability of arterial tissue is strain-dependent. Holmes *et al.* [92] formulated the kinematics for visco-elastic response of articular cartilage during loading circumstances. They reported a nonlinear diffusive interaction between the fluid and porous solid phases of the soft tissue during flow. In modeling governing dynamics, they considered interaction under uni-axial stress relaxation in compression. They employed biphasic mixture theory in which strain-dependent permeability was incorporated that was found in an earlier experimental study. Mow *et al.* [93–97] extended his work and apply mixture theory on articular cartilage by considering the cartilage composed of two phases: deformable porous material and synovial fluid. Ateshian *et al.* [98] investigated the role of surface porosities and interstitial fluid pressurization on the boundary friction of cartilage. They developed a theoretical model of a boundary friction for soft biological tissue (articular cartilage). Their model gives the insight of fluid pressure inside the tissue during confined compression. Results gave an excellent agreement by comparing theoretical proposed model with experimental results.

Based on the previous study, the behavior of a cavity during an injection of Newtonian fluid into soft biological tissue is considered [99]. Due to high pressure, fluid flows into the tissues which are near to cavity. However, it is absorbed by lymphatics and capillaries. The absorption of the fluid depends on the local pressure. Tissue is modeled by considering it as a deformable porous material. Governing equations for solid displacement and fluid pressure are solved analytically and numerically. Barry and Aldis [100] studied the behavior of biological tissues due to fluid flow. Flow-induced deformation due to pressure difference

is analyzed for finite and as well as infinitesimal deformations. Solution is obtained for one-dimensional compression and use experimental data for comparison. Matthew [101] used mixture theory to model lungs. Similarly, Oomens *et al.* [102] used mixture theory to model skin by considered it to be a mixture of fluid phase and a solid phase. A nonlinear system is obtained after mathematical manipulation. A numerical technique is employed to solve the system of equation describing the skin. Cornea [103] is modeled by considering it to be biphasic mixture of a solid phase and a fluid phase Mathematical manipulation gives integral solution, which shows that rate of swelling depends on the cornea permeability and swelling pressure. Comparison of experimental and numerical results is also given. For a future direction, experiment is suggested to test the validation of the given theory. All the studies described above were subject to the assumption that tissue is a biphasic mixture of solid and fluid, however, a revolutionary idea was presented by Lai *et al.* [104] for articular cartilage to develop a triphasic mixture theory by including ion phase in addition to solid-fluid phases, representing anion and cation of NaCl salt.

Triphasic theory is formed by combination of two theories; biphasic mixture theory and physico-chemical theory. Gu *et al.* [105] investigated ion transport and osmotic flow using the triphasic theory in a steady diffusion process through charged hydrated cartilage tissue and examined that solvent would flow from positive osmosis (i.e. high salt concentration side) to negative osmosis (i.e. low concentration side), when the constant charge density within the cartilage separating the two electrolyte solution was less than a critical value. Sun *et al.* [106] developed a mixed finite element formulation for charged hydrated soft tissue using triphasic mechano-electrochemical theory. Cation and anion, electrochemical potentials for water and solid displacement are considered as degrees of freedom. Newton-Raphson is used to tackle the nonlinear terms. Implicit Euler backward method is employed to solve Ordinary Differential Equations. One-dimensional free swelling and stress relaxation problems are investigated using finite element formulation. Convergence and accuracy of formulation for one-dimensional problems are compared with finite difference techniques. Comparison with other methods shows the

excellent agreement of results of finite element formulation.

Recent studies suggest that variation of molecular level within the cartilage tissue causes the degeneration of tissue [107]. Thus, it is important to understand the material properties of articular cartilage and interaction among collagen-proteoglycan matrices. Their physical parameters can be studied by examining the swelling dynamics of biological tissue. Various studies have been reported that tissue shrinkage or expansion resulting from changes in ionic strength of articular cartilage due to bathing solution [108, 109]. It is a well known established fact that swelling of the cartilage is due to the ion imbalance between interstitial fluid, cartilage and proteoglycans molecules which are enriched with negative charge. Elmore and co-authors [110] discussed the imperfect elasticity of cartilage and reported the change in deformation in tissue due to increase in cation concentration. Myers *et al.* [27] studied ion-induced deformation of cartilage for constant permeability using continuum mixture theory. In particular, a set of experiments were performed for isometric tension as well as free swelling states on a rectangular strip of cartilage subject to change in salt concentration of the bathing solution. This study extended biphasic theory by adding the ion-concentration term in the solid stress equation and reported that deformation of articular cartilage is inhomogeneous and anisotropic in nature. Myers *et al.* [14] investigated the behavior of a sample of soft tissue using triphasic theory due to change in ion-concentration in and around the tissue. Under certain assumptions, the governing equations were reduced to coupled partial differential equations which were given in spherical, cylindrical and Cartesian geometries involving solid deformation and ion-concentration. Their work predicted a lower ion concentration for Cartesian geometries as compared to earlier work of Myers *et al.* [27]. They made a comparison between theoretical and experimental work for Cartesian geometry which deals with changing the ion-concentration of NaCl salt solution shower on a strip of soft biological tissue. Gu *et al.* [111] presented a triphasic mixture theory for biological tissues. They modeled charged hydrated tissue by considering it as a mixture consists of three phases, i.e., ion-phase, solvent phase (non-charged) and a solid phase (charged). Result of their theory shows that various forces are involved in flow of solvent and

ions through the soft tissues: 1) An electric force; 2) an electrochemical force; and 3) mechanochemical force. They also show that various material properties are govern the transport rates of solvent and ions from the soft tissues. They have also presented the fluid velocity field, stress and strain for an infinitesimal thick tissue sample during diffusion process. Numerical results have been presented for exchange of ions through the soft tissue.

Ricken *et al.* [112] presented a triphasic model for a biological tissue. They modeled the tissue as it consists of water, nutrients and a solid phase. Equation of growth is found by using theory of porous media by determining the factors on which mass exchange depends, i.e., local ratio of nutrients and state of stress. After presenting the detailed model using mathematical calculation, governing equation for large deformations is presented. Also various numerical examples have been examined. Gu *et al.* [113] developed a triphasic theory to study the behavior of soft biological tissues containing various types of polyvalent ions. They used their theory to model the transport of ions and fluid through tissues. Frijns *et al.* [114] extended the triphasic theory to quadriphasic theory in which cations and anions are included as separate phases along with solid and fluid phase to observe shrinking and swelling behavior of the intervertebral disc. Recently, Cyron and Humphrey [115] used mixture theory to study soft biological tissues. They have reviewed approaches to model tissues, i.e., hybrid approach, continuum theory approach and mechano-regulated approach. They have also discussed mechanobiological stability, a new approach to model soft tissues. They have also discussed future direction for a modeling of soft biological tissues. Latorre and Humphrey [116] formulated the mechanobiologically modeling using mixture theory approach. This model used to analyze the steady-state and time independent responses of soft biological tissues. Governing equations that characterize mechanobiologically model, can be expressed in terms of nonlinear and time-independent algebraic equations. Solution to these equations gives the long-term results of tissue growth. Truster and Masud [117] developed a computational approach using mixture theory approach to model soft biological tissues. They have considered the problems of soft tissue engineering. They have considered two cases: 1) growth at fixed volume; 2)

growth at fixed density to analyze the various types of tissues. Numerical study is employed to study the effects of various parameters. Pourjafar *et al.* [118] have numerically studied the linear stability of two-dimensional flow of viscous fluids through channel. Viscoelastic bio-material layer is used to line the channel. Model is developed using biphasic mixture theory to handle solid-fluid interaction. Basic solution is obtained which was analyzed by using linear stability analysis. After mathematical manipulation, eigenvalue problem has been obtained, which was tackled using numerical technique. Numerical simulations show that anisotropy has no effect on stability of viscous fluid flow. However, inhomogeneity causes critical effect on Reynolds number. Due to importance of non-Newtonian fluid, Aftab *et al.* [119] investigated the behavior of a spherical cavity during an injection of non-Newtonian fluid. Governing equations are obtained in terms of fluid pressure and solid displacement. Numerical results predicted that shear-thinning fluid exhibits more fluid pressure and induces more solid deformation as compared to shear-thickening fluid. Increase in the solid deformation increases the absorption of the non-Newtonian power-law fluid in the biological tissue. Results are compared with Newtonian fluid to magnify the effects. Farooq and Siddique [120] used mixture theory to study the effects of permeability parameter and power-law index on the articular cartilage due to non-Newtonian fluid flow. Results were presented for solid deformation and fluid pressure. Graphical illustrations show that strain-dependent nonlinear permeability induces less solid deformation as compared to the linear permeability. Moreover, authors [121–125] used mixture theory to model cancer, tumor growth and remodeling of soft biological tissue. Now we turn our attention to the process of magnetohydrodynamics (MHD).

In magnetohydrodynamics process, magnetic fields can induce forces in a moving conductive fluid, which in turn changing the magnetic field itself. In 2011, Eldable and co-workers [126] presented revolutionary work by developing a model for the flow of non-Newtonian fluid (bi-viscosity) through porous media under an applied magnetic field. Model is based on the assumptions that porous material is homogeneous, isotropic and linear elastic solid. Various laws of Physics are

combined to form governing equations in terms of fluid velocity and solid displacement. Fourier series has been used to solve these equations analytically. Graphs are obtained to show the effects of interaction between solid phase and a fluid phase, non-Newtonian parameters and magnetic field on the fluid flow.

Following this work, Siddique and Kara [127] discussed the capillary rise of MHD fluid into deformable porous material. Due to capillary suction, fluid begins to imbibe in a dry and undeformed sponge type porous material. They showed that the force that induces a stress gradient is the pressure gradient across the evolving sponge and causes solid deformation. Problem is formulated into nonlinear moving domain problem and transformed to a fixed domain problem using appropriate coordinates. Method of Lines approach has been employed to solve the nonlinear equations. Graphical illustrations show that solid deformation decreases and capillary rise of fluid reduces due to magnetic effects.

Naseem *et al.* [128] investigated the problem of infiltration of the MHD fluid into a deformable porous material. Mathematical model has been developed using mixture theory approach. A nonlinear free boundary problem has been obtained after mathematical manipulation. Due to the capillary rise action of the fluid, the driving force of pressure gradient across the porous material produces stress gradient which in turn generates solid deformation in the material. Method of Lines approach is used to solve governing equations. Graphical comparison with Newtonian fluid shows that uniform magnetic field slows down the capillary rise process.

Sreenadh *et al.* [129] studied the problem of Couette flow of a Jeffrey fluid in the channel. Under an applied magnetic field, the channel under consideration is bounded below by a moving rigid plate and by a finite layer of a deformable porous material. The governing equations for velocity field and solid displacement are obtained after mathematical manipulation. These equations are not only solved in the porous flow regions but also in the free flow. Graphical results are used to analyze the effects of viscosity parameter, magnetic parameter, Jeffrey parameter, shear stress, mass flux, displacement and upper plate velocity.

Aftab *et al.* [130] investigated the interaction of electrically conducting fluid and biological tissue. In the presence of uniform magnetic field, a mathematical model has been developed to observe deformation in the tissue due to fluid flow. The biological tissue has been modeled on the assumptions that it is deformable porous material and consists of two phases, i.e., solid phase and a fluid phase. The driving force is the high cavity pressure that generates fluid flow through the biological tissue. Mixture theory is employed to develop the mathematical model on the assumption that permeability of the tissue is nonlinear strain-dependent and deformation of the solid is very small. Governing equations for fluid pressure and solid deformation are obtained after mathematical manipulation. Method of Lines approach has been employed to solve governing equation for fluid pressure, whereas trapezoidal rule has been employed to solve governing equation for solid deformation in the tissue. Graphical results show the effects of magnetic parameter on the solid deformation and fluid pressure.

Usman and Javed [131] studied the biomechanical response of soft biological tissue, hydrated with an electrically conducting liquid. Uniform magnetic field is applied to biphasic mixture of fluid phase and a solid phase. Pressure applied on the tissue, and permeability of the tissue govern the solid deformation and rate of flow. Tissue is modeled on the assumption that constituents of the tissue are incompressible. Governing equations of solid displacement and fluid pressure are obtained after mathematical manipulation. Numerical solution is obtained for strain-dependent permeability, whereas analytical solution is given for constant permeability. Graphical illustration shows the effects of magnetic parameter on fluid pressure and solid displacement. We now turn our attention to the application of MHD.

In the last few decades, many authors discussed the applications of magnetic field to biological tissues. Magnetic and electric fields can induce currents in synovial joints and also in synovial fluid [132]. Magnetic fields can induce currents in the body and also can pass through the biological tissues. External applied field causes biological effects in various physiological systems [133]. The important application

of magnetic field in an artificial human joints has been presented by Bagwell *et al.* [134] through the model which incorporating bone in-growth into the porous implants. It has been a well-establishing fact that the external applied magnetic field has notable effects on physiological systems and can regenerate biological tissue.

Elco and Hughes [135] presented the idea of magnetohydrodynamic bearing and also analyzed two different types of bearing. They have considered axial induced current pinch with bearing of hydrostatic thrust. It has been shown that pinch effect can increase the load capacity. They have considered the second bearing and called it infinite inclined slider with an external applied magnetic field perpendicular to the slider's motion and parallel to the bearing's surface. For this type the electrical characteristics, load capacity and pressure distribution have been calculated. Yamamoto and Gondo [136] investigated the effect of externally applied magnetic fields on carbon steel. They showed that magnetization can increase the reactivity of carbon steel. It has been also proved that the coefficient of friction can also increase by applying the magnetic field. Due to an increase in the coefficient of friction, the resistance of the boundary films or the adsorbed films increases. Oils containing polar elements show enhancement in friction as compared to oils without polar substances. As it has been expected that molecules with polar substances are oriented with the magnetic field. In 1991, Tandon *et al.* [137] presented a possible application of the magnetohydrodynamics (MHD) for the physiological system. Mathematical model has been developed for the synovial joints subjected to the transverse magnetic field. Approximate solutions of the governing equation depend on three regions, i.e., two parallel regions of porous layers separated by third region of the thin film of synovial fluid. Results show that suitable adjustment of applied magnetic field can decrease the coefficient of friction between the joints and can help in normal articulation in arthritis. Yiwen *et al.* [138] discussed the various MHD applications in aeronautical engineering, i.e., MHD turbine engine, MHD acceleration wind tunnel and MHD power generation, etc. An excellent review on applications of MHD in biomechanics given by

Rashidi *et al.* [139]. In the following section, we furnish a brief description of each problem presented in this thesis.

1.3 Thesis Outline

A deformable porous material deforms when fluid flows through it. Due to deformation its permeability changes which affects the fluid flow. So we need continuum mixture theory to study the mixture of solid and fluid to examine the deformation in deformable porous material. We now present a brief introduction of each chapter in this thesis.

In Chapter 2, basic concepts and definitions are presented related to deformation of deformable porous material due to fluid flow. Basic equations of mixture theory are also presented which will be used to model problems in later chapters. Numerical methods are also discussed which are used to solve nonlinear PDEs which are obtained after mathematical modeling.

In Chapter 3, a mathematical model of compression molding of deformable porous material preimpregnated with non-Newtonian fluid is developed using mixture theory approach. In this process, piston is applied on top of pile to compress deformable material preimpregnated with non-Newtonian fluid. Moving domain problem is formulated using Eulerian frame of reference and then transformed to fixed domain problem using Lagrangian coordinates. The dynamics is controlled by pressure applied on the piston or velocity of piston. The unsteady solutions for the solid volume fraction as a function of time and space are presented. In particular, effect of power-law index on solid volume fraction is illustrated graphically.

The synovial fluid found in the cartilage tissue exhibits the behavior of non-Newtonian fluid as it contains the hyaluronic acid (hyaluronan), lateral patellar groove (LPG) and many other traces of different macromolecular components. So,

it is important to discuss its effects on biological tissues. In Chapter 4, we discuss ion-induced swelling behavior of soft tissue due to non-Newtonian fluid flow and its effects on solid displacement and fluid pressure. Mathematical model is developed using mixture theory approach. Modified Darcy's law, conservation of mass for both phases and Navier-Stokes equations are combined to form governing equations in terms of solid displacement and fluid pressure. Governing equations are solved numerically to highlight the effects of power-law index and time.

In Chapter 5, we investigated the behavior of soft tissue which is bathed in power-law fluid under stress relaxation in compression. Ramp displacement is imposed on the surface of hydrated articular cartilage. Fluid pressure and deformation of soft tissue are examined for the slow and fast rate of compression. A linear mixture theory is employed to develop a mathematical model to get governing equations in term of solid displacement and fluid pressure. Equations are solved numerically to highlight the effects of power-law index and permeability parameter.

In chapter 6, a mathematical model for compressive stress-relaxation of articular cartilage has been developed for the deformation of the solid phase of the cartilage due to the flow of the electrically conducting fluid from it. The model is based on the biphasic mixture theory which incorporates the nonlinear strain-dependent permeability. The system of coupled partial differential equations was developed for the fluid pressure and solid deformation for the slow and fast rate of compression in the presence of the Lorentz forces. The resulting system is solved numerically using Method of Lines (MOL) and graphs are produced to highlight the effects of the magnetic parameter on fluid pressure and solid displacement.

In chapter 7, conclusion and future direction are presented.

Chapter 2

Preliminaries

2.1 Introduction

This chapter begins with a brief overview of basic definitions and important concepts which will be helpful in understanding the fluid flow through porous material. The details of basic equations of mixture theory including balance laws and kinematic relations are also given in this chapter. In the end, we present details of numerical methods used to solve the governing equations obtained after modeling of different problems.

2.2 Porous Material

A porous material is a material containing pores, empty or void spaces. Skeletal portion of this material is called the "frame" or "matrix". Moreover, porous material is usually characterized by void fraction (porosity). Other properties associated with such materials are low density, thermal conductivity, chemical stability and electrical conductivity [140]. Due to excellent chemical and physical properties, porous materials have been extensively used in various applications such as adsorbent, thermal insulation, molecular sieves, gas separation and water purification, etc [141–145]. Due to these important properties, it is essential to

model the problems involving porous materials.

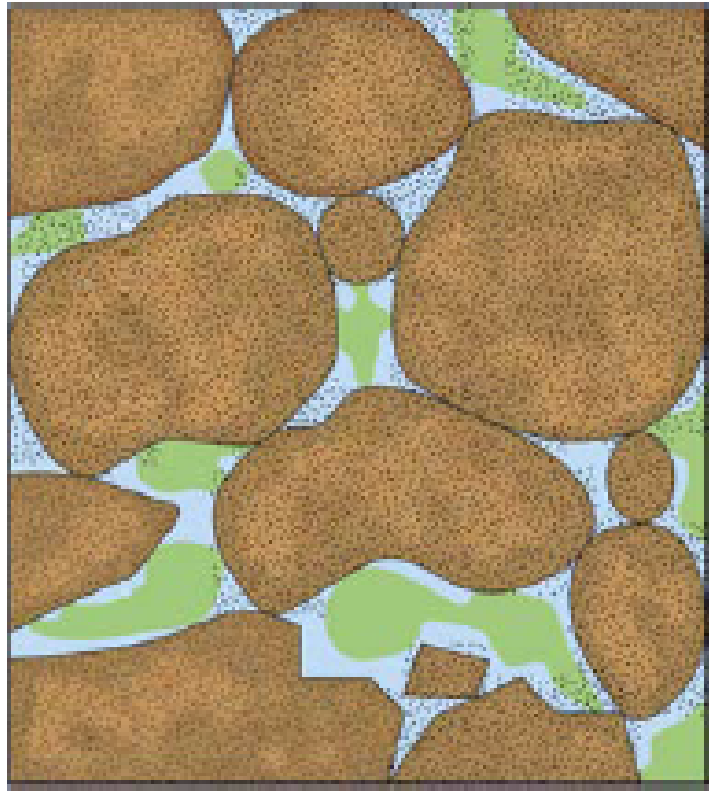


FIGURE 2.1: Schematic diagram of a porous material [146].

Porous materials are generally classified into two main categories: rigid and deformable porous materials. Rigid porous materials are those materials which do not deform when fluid flows through them such as a brick, wood and pipe, etc. On the other hand, deformable porous materials are those materials which deform when fluid flows through them. Examples of such materials include articular cartilage, foam and sponge, etc.

2.3 Porosity

Measure of void or empty spaces in a material is called porosity which is a fraction of the volume of empty spaces over the total volume, between 0% and 100%, or

as a number between 0 and 1. Mathematically

$$\phi_p = \frac{V_v}{V_T}, \quad (2.1)$$

where V_v is the volume of void space and V_T is the total volume of porous material, including the skeletal as well as empty components. Moreover, due to less porosity, biological tissue like articular cartilage is said to be less porous than a sponge. The porosity of the porous material can be tested in many ways e.g., imbibition, gas expansion method, water evaporation method, optical and computerized tomography (CT) scanning method.

2.4 Darcy's Law

Darcy's law is actually an equation that describes the flow of fluid through permeable medium (porous medium). Based on the experimental results, Henry Darcy [147] formulated the famous Darcy's law which describes the flow of water through aquifers. Ignoring the gravitational forces, Darcy's law is stated that the total discharge Q' of fluid from a porous media is directly proportional to permeability $\bar{\kappa}$ of porous material, cross sectional area A of a porous media, and total pressure drop ΔP and inversely proportional to length L over which the pressure drop is taking place and dynamic viscosity of fluid μ . Mathematically, Darcy's law can be written as

$$Q' = -\bar{\kappa} \frac{A \Delta P}{L \mu}. \quad (2.2)$$

The negative sign indicates that fluid flows from high potential energy level (or high pressure) to low potential energy level (or low pressure). Now for a more generalized form of Darcy's law for unit length, we divide both sides of the equation (2.2) by the area A to get

$$\phi_E = -\bar{\kappa} \frac{\Delta P}{\mu}, \quad (2.3)$$

where ϕ_E is the discharge per unit area. Darcy's law is analogous to Ohm's law in electromagnetism, Fourier's law in heat conduction and Fick's law in diffusion

theory. Darcy's law deals with the homogeneous and isotropic porous media and is valid for low Reynolds numbers. Indeed, Darcy's law can be easily extended for multi-phase flows [146].

2.4.1 Permeability

Permeability is defined as the ability of a porous material to allow a fluid to pass through it. It is denoted by the symbol \bar{k} . The permeability of a porous material depends on the porosity and the structure of porous material.

If the porous material has connective pores then it is more permeable as compared to porous material having unconnected pores. Permeability is measured in Darcy (d), named after the French Engineer Henry Darcy. However, the SI unit of permeability is m^2 , but unit Darcy (d) is widely used in geology, physics and petroleum engineering. 1 Darcy is almost equals to $10^{-12} m^2$. Permeability can be written mathematically as

$$\bar{k} = -\mu \frac{\phi_E}{\Delta P}, \quad (2.4)$$

where ϕ_E is the discharge of fluid per unit area, μ is the dynamic viscosity of the fluid flowing through the porous material and ΔP is the applied pressure difference. Moreover, negative sign indicates that fluid flow from high pressure to low pressure.

It is worth mentioning that the term permeability has different meanings in different fields such as transportation, chemistry, electromagnetism and soil mechanics.

2.5 Cell

The word cell derives from the Latin word *cella* which means small room. Cell is the basic biological, functional and structural unit of all living organism. Cell is

the building blocks and smallest unit of life.

The study of cells and their functions is called cellular or cell biology. Cell is made of cytoplasm present within a membrane, consisting of bio-molecules such as nuclear acids and proteins. Organism can be classified on the basis of cell, multicellular (including animals and plants) or unicellular consisting of a single cell including bacteria.

2.6 Tissue

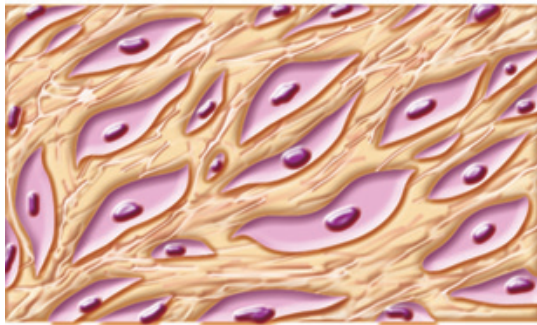
The word tissue comes from the French word "tissu" which means something that is "woven". Tissue is used to describe a group of cells found together in an organism having an identical structure that achieve the same tissue's function and makes up the organs in the animal body such as the articular cartilage, lungs, brain, and heart, etc.

On the basis of structure, animal's tissues are classified into four types: nervous, muscle, connective and epithelial. Histology is a branch of biology in which we study animal and human tissues and called histopathology if it in connection with any disease.

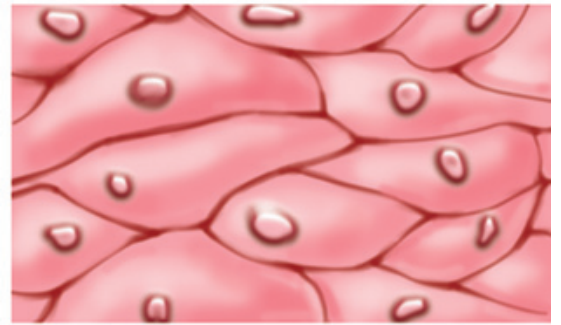
Moreover, soft tissues are those which surround, support and connect other organs of the animal body, such as the synovial membranes, fibrous tissues, tendons, fascia, nerves and ligaments. Soft tissue like articular cartilage composed of ground substance, elastin, collagen and exhibit properties of porous material which make them amenable to the physical and mathematical analysis.

Humphrey [1] mentioned and discussed different theoretical frameworks available in literature for modeling different biological tissues. Among these, mixture theory is one of widely used and well-accepted theory, in which biological tissue is modeled by considering it porous material and consist of two phases i.e., solid and fluid. Figure 2.2 shows types of animals tissues, i.e., Connective, Epithelial and Muscle and Nervous tissues.

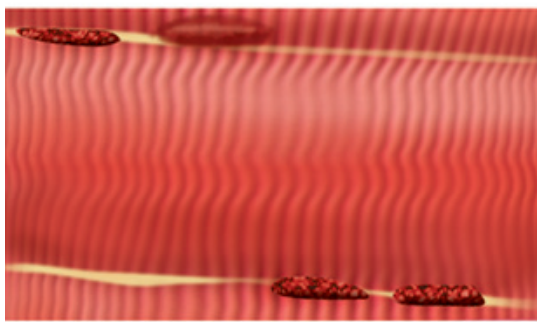
Four types of tissue



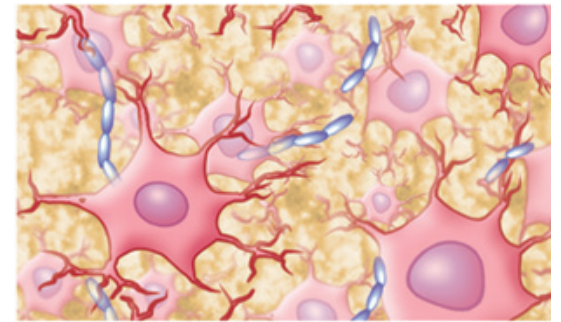
Connective tissue



Epithelial tissue



Muscle tissue



Nervous tissue

FIGURE 2.2: Types of animal tissue [148].

2.7 Magnetohydrodynamics

Magnetohydrodynamics (MHD) is a branch of Fluid Dynamics that deals with the dynamics of the magnetic field in an electrically conducting fluid, i.e., electrolytes, plasmas, salt water, electrolytes and liquid metals. Swedish physicist Hannes Alfvén was the first one who laid down the foundation of this field. The coupling of Navier-Stokes equations with Maxwell equations is used to describe the dynamics of MHD system. Initially, MHD was applied to model the problems of geophysics and astrophysics, however, its applications are now encompassing many other branches of science such as magnetobiology, magnetochemistry and bioelectromagnetism, etc. Moreover, applied magnetic fields have significant effects on industrial as well as physiological systems. It has been verified experimentally that

external applied magnetic field regenerates the biological tissue and also stimulates the function of tissues [149, 150]. Recently, many hazardous diseases such as tumors and cancer are treated by using an applied magnetic field [151, 152]. It is worth mentioning that the human body contains a magnetic field, which can assist in drug targeting and cell isolation for clinical purposes under suitable applied magnetic field [153].

2.8 Preimpregnated Materials

Preimpregnated materials are composite materials in which a number of fibers is pre-impregnated with a thermoset resin matrix or thermoplastic in a certain ratio. Due to unique properties, preimpregnated materials can be cured under high pressures and temperatures. Common resins include epoxy, urea-formaldehyde, alkyds, phenolic and silicone, etc.

2.9 Heaviside Step Function

The Heaviside step function is also called Unit step function, usually represented by $\theta(x)$ or $H(x)$. Oliver Heaviside was an English physicist and mathematician, who developed the idea of this function on the bases of signal that turns on at a specific time and stays on indefinitely. Mathematically, Heaviside step function can be written as

$$H(x) = \begin{cases} 0, & x \leq 0 \\ 1, & x > 0 \end{cases} \quad (2.5)$$

2.10 Fluid and Its Classification

A fluid is a substance that has no fixed shape and deforms easily under an applied stress. Petrol, syrup, ketchup, air and water are some examples of fluids. Viscosity

and density are two intrinsic properties of fluid which govern the behavior of fluid flow. Viscosity of fluid is a measure of its resistance to gradual deformation by tensile stress or shear stress. It corresponds to the measurement of internal thickness of fluid. For example, honey has a higher viscosity than petrol whereas density determines that how much mass of a substance is present and how much space is covered by it. Generally, density is defined as mass per unit volume.

Fluids are classified on the basis of viscosity. Sir Isaac Newton was an English physicist and mathematician, who in the late seventeenth century stated the Newton's law of viscosity which states that shear stress in a fluid is directly proportional to the velocity gradient, i.e. time rate of strain. Such types of fluids are called Newtonian fluids. Mathematically, Newton's law of viscosity can be written as

$$\tau = \mu \frac{du}{dy} \quad (2.6)$$

where τ is the shear stress, μ is viscosity and du/dy is the rate of shear deformation. All those fluids which do not obey the Newton's law of viscosity are called non-Newtonian fluids. An ostwald-de waele or the power-law model, is a generalized fluid model for which the shear stress, τ , is given as

$$\tau = \bar{K} \left(\frac{du}{dy} \right)^n \quad (2.7)$$

where \bar{K} is the flow consistency index and n is the power law index. On the basis of value of power law index n , Ostalwald-de waele fluids can be subdivided into three types. Shear-thinning or Pseudoplastic ($n < 1$) are those time independent fluids whose behavior is Newtonian at low shear rates then there viscosity decreases with increasing shear rate. Shear-thinning fluids are ubiquitous in biological or industrial processes.

Examples of shear-thinning fluids are styling gel (composed of vinylpyrrolidone copolymer and water), blood, paints and ketchup. Shear-thickening or dilatant ($n > 1$) are those non-Newtonian time independent fluid whose viscosity increases

with increases in shear rate. A Common household example of dilatant fluid is oobleck (solution of water and cornstarch).

Figure 2.3 shows the behavior of shear-thinning, Newtonian and shear-thickening fluids as a function of rate of strain and stress. The profile of Newtonian fluid shows linear behavior as compared to shear-thinning and shear-thickening fluids.

Profile of shear-thickening fluid shows concave up behavior, whereas, shear-thinning fluid shows concave down behavior. Table 2.1 shows power-law fluid model. Shear-thinning fluid corresponds to power-law index $n < 1$, Newtonian fluid corresponds to the power-law index $n = 1$, whereas, shear-thickening fluid corresponds to the power-law index $n > 1$.

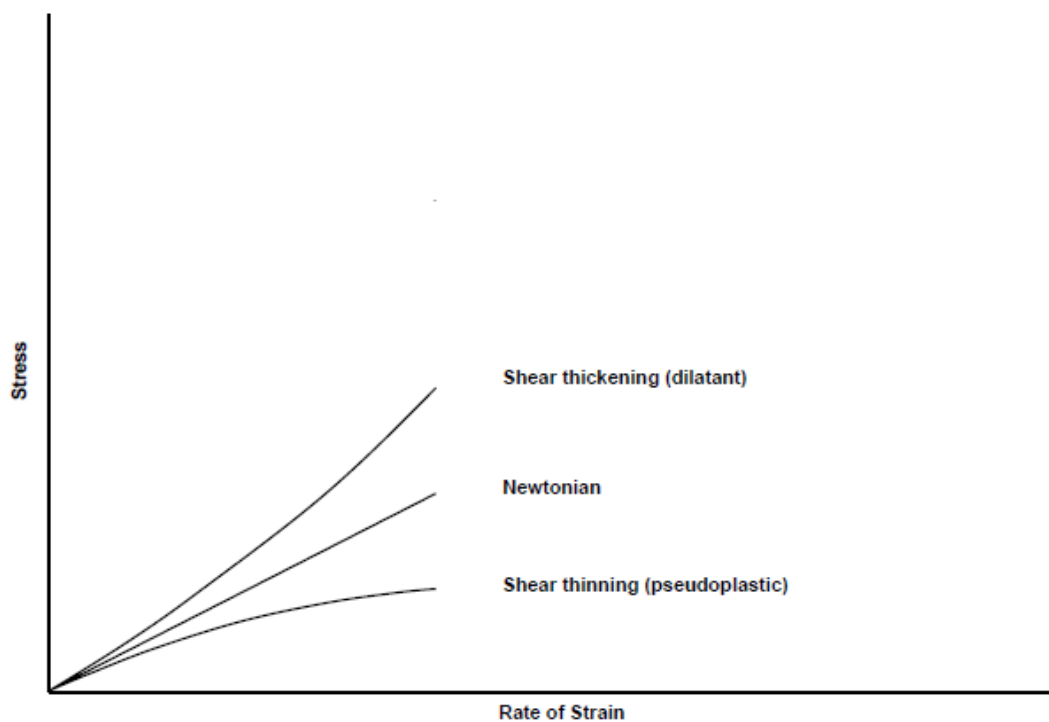


FIGURE 2.3: Schematic diagram of a power law fluid presented in a generic graph of shear stress τ against gradient du/dy [8].

Non-Newtonian fluid is used for manufacturing of specific bulletproof military suit. There is some type of non-Newtonian fluid present inside the suit, which keeps its fluid state while the soldier moves or stands still, but will convert into solid state when the bullet hits.

TABLE 2.1: Power-law fluid model

Power-law index n	Type of fluid
$= 1$	Newtonian Fluid
< 1	Pseudoplastic or shear-thinning fluid
> 1	Dilatant or shear-thickening fluid

It is also used for the manufacturing of special sport shoes. In these shoes, interior portion is filled with a specific type of non-Newtonian fluid which retains its fluid state in normal pressure, but converts into solid state in high pressure to prevent the feet from injury. So the non-Newtonian fluids find many applications in military, industry, bio-fluids, automobile, food processing, polymer solutions, and solid suspensions, etc.

In the following, we give a brief description of the continuum mixture theory which is a main building block of this thesis.

2.11 Mixture Theory

Mixture is a material that is made by mixing two or more substances together without any chemical process. Mixture whether man-made or natural exists in the form of colloids, suspension and solutions. Moreover, the desideratum for the continuum mixture theory arises whenever processes involve constituents mass exchanges or relative motions between the constituents of mixture. These phenomenon can be found in both biological as well as in industrial settings and can be analyzed using mixture theory. Epstein and Marcelo [154] stated the basic assumptions of mixture theory are (i) at any instant of time, all constituents of mixture are present at each point of spatial domain and (ii) the mixture obeys basic principals of mass and momentum balances. The basics of balance laws and kinematics for the mixture of n constituents is presented below.

Consider a mixture that consists of $n \geq 2$ immiscible constituents which are supposed to occupy each point in space at each instant of time. Moreover, motion of

the n constituents of mixture is described by n equations

$$\mathbf{x} = \chi^\varphi(\mathbf{X}^\varphi, t), \quad (2.8)$$

where $\varphi = 1, 2, 3, 4, \dots, n$ and \mathbf{X}^φ represents the typical material point belonging to the reference configuration of the φ^{th} constituent. At any time t , \mathbf{x} represents the typical point in the configuration occupied by the mixture.

The inverse function of χ^φ can be represented as

$$\mathbf{X}^\varphi = \zeta^\varphi(\mathbf{x}, t). \quad (2.9)$$

The mass density, ρ , of the mixture can be expressed as

$$\rho = \sum_{\varphi=1}^n \rho^\varphi, \quad (2.10)$$

where ρ^φ represents the mass density of the φ^{th} constituent of the mixture. The volume fraction ϕ^φ of the φ^{th} constituent of mixture is expressed as

$$\phi^\varphi = \frac{\rho^\varphi}{\rho_p^\varphi}, \quad (2.11)$$

where in homogenous state, density for φ^{th} constituent is represented by ρ_p^φ . The volume fractions must satisfy the following equation for a saturated mixture

$$\sum_{\varphi=1}^n \phi^\varphi = 1. \quad (2.12)$$

Moreover, a velocity field \mathbf{v}^φ associated with each constituent of a mixture expressed in material description as

$$\mathbf{v}^\varphi = \frac{\partial \mathbf{X}^\varphi}{\partial t}. \quad (2.13)$$

The Eulerian description of the velocity field is given by the relation

$$\mathbf{v}^\varphi = v^\varphi(\mathbf{x}, t). \quad (2.14)$$

Now we introduce a mean velocity of the mixture which is the sum of individual mass flows equals to the flow of total mass so that

$$\rho \mathbf{v} = \sum_{\varphi=1}^n \rho^{\varphi} \mathbf{v}^{\varphi}. \quad (2.15)$$

It is worth mentioning here that mean velocity of the mixture is considered as the velocity of center of mass of constituents. However, it is noted that \mathbf{v} has no physical significance and can be replaced by a diffusion velocity expressed as

$$\mathbf{u}^{\varphi} = \mathbf{v}^{\varphi} - \mathbf{v}. \quad (2.16)$$

Now for φ^{th} constituents of the mixture, material time derivative $\frac{D^{\varphi}}{Dt}$ for the arbitrary scalar function ψ is expressed as [20, 155]

$$\frac{D^{\varphi} \psi}{Dt} = \frac{\partial \psi}{\partial t} + (\mathbf{v}^{\varphi} \cdot \nabla) \psi. \quad (2.17)$$

For a mixture as a whole, material time derivative can be written as

$$\frac{D \psi}{Dt} = \frac{\partial \psi}{\partial t} + (\mathbf{v} \cdot \nabla) \psi. \quad (2.18)$$

Moreover, we turn our attention to the conservation of mass and the linear momentum for the mixture. Conservation of mass is given by Atkin and Craine [20] for the φ^{th} component of mixture is

$$\frac{\partial \rho^{\varphi}}{\partial t} + \nabla \cdot (\rho^{\varphi} \mathbf{v}^{\varphi}) = \rho^{\varphi} \Phi^{\varphi}, \quad (2.19)$$

where $\rho^{\varphi} \Phi^{\varphi}$ is the mass supply rate of the φ^{th} constituent of the mixture.

Similarly, conservation of linear momentum for φ constituent of mixture is

$$\frac{\partial}{\partial t} (\rho^{\varphi} \mathbf{v}^{\varphi}) + \nabla \cdot (\rho^{\varphi} \mathbf{v}^{\varphi} \otimes \mathbf{v}^{\varphi}) = \nabla \cdot \mathbf{T}^{\varphi} + \rho^{\varphi} \Phi^{\varphi} \mathbf{v}^{\varphi} + \boldsymbol{\pi}^{\varphi} + \rho^{\varphi} \mathbf{b}^{\varphi}, \quad (2.20)$$

where T^{φ} is the stress tensor, $\rho^{\varphi} \mathbf{b}^{\varphi}$ the body force, $\boldsymbol{\pi}^{\varphi}$ is the internal interaction force. Articular cartilage is binary mixture of fluid and solid (i.e. $\varphi = f, s$),

under certain assumptions, conservation of mass (2.19) and conservation of linear momentum (2.20) will be used to develop mathematical model of binary mixture of fluid and solid. The simplified form of balance (2.19) under certain assumptions is given by Fusi and Farina [155]

$$\frac{\partial \rho}{\partial t} + \text{div}(\rho \mathbf{v}) = 0. \quad (2.21)$$

Similarly, simplified form of linear momentum (2.20) is written as

$$\rho \frac{D\mathbf{v}}{Dt} = \rho \mathbf{b} + \text{div} \mathbf{T}. \quad (2.22)$$

The assumptions that have been used in above two equations are $\sum_{\varphi=1}^n (\boldsymbol{\pi}^{\varphi} + \rho^{\varphi} \Phi^{\varphi} \mathbf{v}^{\varphi}) = 0$ and $\sum_{\varphi=1}^n \rho^{\varphi} \Phi^{\varphi} = 0$. It is worth mentioning that only conservation of linear momentum and mass for the mixture are presented here. Moreover, rotational and thermal effects are not considered in this study.

2.12 Power-law Fluid Modeling for a Biphasic Mixture of Solid Phase and a Fluid Phase

Consider the binary mixture of a deformable porous material and non-Newtonian fluid. Problem is modeled using continuum mixture approach. Basic assumption of mixture theory is that each constituent of mixture is continuous and present at each point in the mixture. Further assumption is that solid elastic matrix is isotropic and homogeneous and also assume that fluid in a biphasic mixture is viscous and non-Newtonian which follows power-law model. The apparent density for the constituents of the mixture is written as

$$\rho^{\beta} = \lim_{dV \rightarrow 0} \frac{dm^{\beta}}{dV}, \quad (2.23)$$

where $\beta = s$ represents solid phase, whereas $\beta = f$ represents fluid phase, dm^{β} be the mass of β phase in small volume dV . The relative porosity ϕ^{β} and true

density ρ_T^β of the β phase of the biphasic mixture are written as

$$\phi^\beta = \lim_{dV^\beta \rightarrow 0} \frac{dV^\beta}{dV}, \quad (2.24)$$

$$\rho_T^\beta = \lim_{dV^\beta \rightarrow 0} \frac{dm^\beta}{dV^\beta}, \quad (2.25)$$

where dV^β represents small volume of the β phase. Using relations (2.24) and (2.25) into equation (2.23), we get a equation which defined relation between porosity and density as

$$\rho^\beta = \phi^\beta \rho_T^\beta. \quad (2.26)$$

The relation between volume fractin of the solid phase ϕ^s and volume fraction of fluid phase ϕ^f can be defined as [99]

$$\phi^s + \phi^f = 1. \quad (2.27)$$

Similarly, relation for density of the solid phase ρ^s and density of the fluid phase ρ^f with density of mixture ρ is written as [99]

$$\rho^s + \rho^f = \rho. \quad (2.28)$$

Conservation of balance of linear momentum for solid and fluid phases can be written as

$$\rho^\beta \left(\frac{\partial \mathbf{v}^\beta}{\partial t} + (\mathbf{v}^\beta \cdot \nabla) \mathbf{v}^\beta \right) = \nabla \cdot \mathbf{T}^\beta + \rho^\beta \mathbf{b}^\beta + \boldsymbol{\pi}^\beta, \quad (2.29)$$

where $\beta = s$ represents the solid phase and $\beta = f$ represents the fluid phase, $\mathbf{T}^\beta = -\phi^\beta p \mathbf{I} + \boldsymbol{\sigma}^\beta$ represents stress tensor for the β phase, \mathbf{I} is the identity

tensor, ϕ^β represents volume fraction of β phase. Conservation of balance of mass for the solid and a fluid phase can be written as [99]

$$\frac{\partial \rho^s}{\partial t} + \nabla \cdot (\rho^s \mathbf{v}^s) = 0, \quad (2.30)$$

$$\frac{\partial \rho^f}{\partial t} + \nabla \cdot (\rho^f \mathbf{v}^f) = -\gamma \bar{p}, \quad (2.31)$$

where \mathbf{v}^s , \mathbf{v}^f are the velocities, and ρ^s , ρ^f are the densities of solid and fluid phases, respectively, \bar{p} be the fluid pressure and γ is a constant of proportionality which depends upon the permeability of the walls and lymphatics in the tissue. Moreover, the term $-\gamma \bar{p}$ appearing in equation (2.31) depends upon the loss of liquid mass which is proportional to the fluid pressure \bar{p} while it passed through lymphatics and capillaries. Using the equation (2.26) into the equations (2.30) and (2.31), we get

$$\frac{\partial \phi^s}{\partial t} + \nabla \cdot (\phi^s \mathbf{v}^s) = 0, \quad (2.32)$$

$$\frac{\partial \phi^f}{\partial t} + \nabla \cdot (\phi^f \mathbf{v}^f) = -\frac{\gamma \bar{p}}{\rho_T^f}. \quad (2.33)$$

Adding equations (2.32) and (2.33) along use of relation (2.27), yields

$$\nabla \cdot \mathbf{v}^c = -\frac{\gamma \bar{p}}{\rho_T^f} \quad (2.34)$$

where

$$\mathbf{v}^c = \mathbf{v}^s \phi^s + \mathbf{v}^f \phi^f, \quad (2.35)$$

is defined to be composite or macroscopic velocity of the biphasic mixture. The equation of diffusive resistance for non-Newtonian power law fluid can be written

as [9]

$$\boldsymbol{\pi}^s = -\boldsymbol{\pi}^f = K(\mathbf{v}^f - \mathbf{v}^s) \left| \mathbf{v}^f - \mathbf{v}^s \right|^{n-1} - \bar{p} \nabla \phi^s, \quad (2.36)$$

where n corresponds to the power law index with $n < 1$ for Pseudoplastic or shear-thinning fluids, $n > 1$ for dilatant or shear-thickening fluids, and K represents coefficient of diffusive resistance. Substituting $n = 1$, in equation (2.36), gives the relation for the Newtonian fluid [99] and substituting velocity of solid phase $\mathbf{v}^s = 0$, and solid volume fraction $\phi^s = \text{constant}$, yields relation for the rigid non-Newtonian fluid case. On substituting equation (2.36) in equation (2.29), the momentum balance equation for the solid phase takes the following form

$$\rho^s \left(\frac{\partial \mathbf{v}^s}{\partial t} + (\mathbf{v}^s \cdot \nabla) \mathbf{v}^s \right) = \nabla \cdot \mathbf{T}^s + \rho^s \mathbf{b}^s + K(\mathbf{v}^f - \mathbf{v}^s) \left| \mathbf{v}^f - \mathbf{v}^s \right|^{n-1} - \bar{p} \nabla \phi^s. \quad (2.37)$$

Similarly, the momentum balance equation (2.29) for the fluid phase takes the following form

$$\rho^f \left(\frac{\partial \mathbf{v}^f}{\partial t} + (\mathbf{v}^f \cdot \nabla) \mathbf{v}^f \right) = \nabla \cdot \mathbf{T}^f + \rho^f \mathbf{b}^f - K(\mathbf{v}^f - \mathbf{v}^s) \left| \mathbf{v}^f - \mathbf{v}^s \right|^{n-1} + \bar{p} \nabla \phi^s \quad (2.38)$$

2.13 Numerical Method

In this section, we present the numerical technique Method of Lines and the MATLAB solver *pdepe* which will be utilized to solve the resulting nonlinear partial differential equations.

2.13.1 Method of Lines

The Method of Lines (MOL) is a numerical technique in which space derivatives are discretized using finite elements or finite differences and leaving the time variable continuous. This technique gives the system of coupled ODEs with same number of initial boundary values which can be solved using suitable ODE solvers. The salient features of MOL include: numerical stability, computational efficiency,

reduced computational time and reduced programming effort, which evidently justify the uses of MOL. In order to illustrate MOL, we present a solution of simple partial differential equation

$$\frac{\partial u}{\partial t} = 3 \frac{\partial^2 u}{\partial x^2}, \quad (2.39)$$

$$0 < x < 2, \quad t > 0,$$

subject to following initial and boundary conditions

$$u(x, 0) = 50, \quad (2.40)$$

$$u(0, t) = 0, \quad (2.41)$$

$$u(2, t) = 0, \quad (2.42)$$

admitting the analytical solution

$$u(x, t) = \sum_{k=0}^{\infty} \frac{200}{\pi} \frac{1}{2k+1} e^{-3(2k+1)^2 \pi^2 t/4} \sin\left(\frac{(2k+1)\pi x}{2}\right). \quad (2.43)$$

We discretize the space derivative appearing in equation (2.39) by using central finite differences

$$\frac{du_j}{dt} = 3 \frac{u_{j+1} - 2u_j + u_{j-1}}{dx^2}, \quad j = 1, 2, 3, \dots, N, \quad (2.44)$$

where the value of u_0 and u_{N+1} can be found from boundary conditions (2.41)-(2.42) [156] and

$$x_j = jdx, \quad (2.45)$$

$$dx = \frac{2}{N}, \quad (2.46)$$

$$u_j = u(x_j, t). \quad (2.47)$$

The value of initial condition at each node can be calculated from the equation (2.42) as

$$u(x_j, 0) = 0. \quad (2.48)$$

Thus, we have obtained a system of N ordinary differential equations (2.44) with initial conditions given in equation (2.48), which is solved using well established MATLAB's ODE solver *ode45*. In Figure 2.4, we present a graphical comparison between numerical (MOL) and exact solution of parabolic PDE (2.39) at time $t = 1.5$. Graphical results show the excellent agreement between the two solutions which validate our proposed numerical scheme.

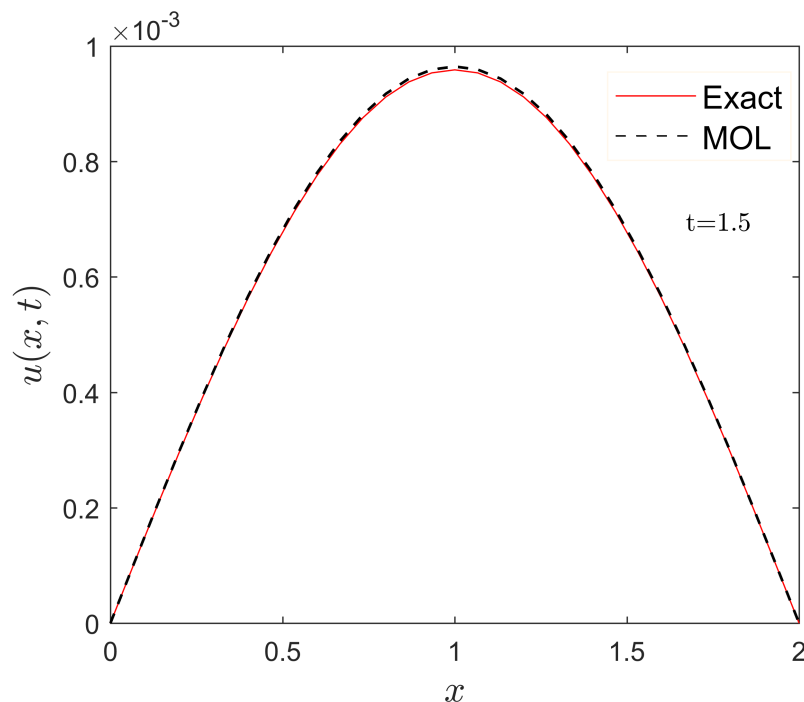


FIGURE 2.4: A comparison between MOL and analytical solution of the parabolic PDE (2.39). Exact (solid line) and numerical (dashed line) are plotted to compare two solutions.

In addition to this, we also present a table in which absolute error between numerical and exact solutions for different number of nodes is given. The absolute error between MOL and exact solution in Table (2.2) for different number of spatial nodes N at time $t = 1.5$ justifies MOL numerical scheme.

TABLE 2.2: Maximum absolute error between MOL solution and exact solution of parabolic PDE (2.39) for different spatial nodes at time $t = 1.5$.

Number of Nodes	Error= $\max(\text{MOL-Exact})$
150	1.4943×10^{-4}
400	5.3229×10^{-5}
600	3.4852×10^{-5}

2.13.2 *pdepe*

The *pdepe* (MATLAB built-in solver) is used to solve initial-boundary value problems usually in single spatial variable. *pdepe* stands for parabolic-elliptic partial differential equation. The function *pdepe* is based on the Method of Lines which uses finite differences for discretizing the spatial derivatives to convert the PDEs into coupled ODEs and leaving the time derivative continuous. The resulting ODEs are then integrated by MATLAB ODE solver *ode15s*. Aftab *et al.* [119] used *pdepe* for the numerical study of non-Newtonian flow-induced deformation in a biological tissue. However, for nonclassical boundary conditions and complex geometries *pdepe* proves to be inadequate and a more sophisticated code MOL is needed.

Chapter 3

Non-Newtonian Flow in Deformable Porous Media: Modeling and Simulations of Compression Molding Processes

3.1 Introduction

In this chapter, a mathematical model of non-Newtonian flow in a deformable porous media has been developed using continuum mixture theory to understand the process of compression molding. In the compression molding, a piston operates on the top of a pile to compress deformable porous material which is preimpregnated with non-Newtonian fluid. The Eulerian coordinate system has been used to model the moving domain problem in terms of solid volume fraction, which was transformed to fixed domain problem using Lagrangian coordinates.

The dynamics of this problem can be controlled either by velocity of piston or pressure applied on the piston. The governing nonlinear equation for solid volume fraction is treated numerically to highlight the effects of various parameters. Numerical results indicate that shear-thinning fluids induce sudden increase in

solid volume fraction ϕ but bring the material to a final state where ϕ is greatly inhomogeneous. Shear-thickening fluid induces increase in solid volume fraction but the final state of ϕ is homogeneous. It is worth mentioning here that the first mathematical model of power-law fluid in combination with mixture theory for capillary rise into a deformable porous material is presented by Siddique and Anderson [9] and current chapter is also based on it. Later on, Aftab *et al.* [119] developed a similar model for soft biological tissues.

In Section 3.2, mathematical model of compression molding process for moving domain using mixture theory approach with the help of Eulerian coordinates has been presented. Section 3.3 deals with the transformation of moving domain to fixed domain by using Lagrangian coordinates. This is followed by the non-dimensionalization of governing equation in Section 3.4. Boundary conditions between deformable porous material and non-Newtonian fluid are presented in Section 3.5. Results and discussion is given in Section 3.6 which is followed by the conclusion in Section 3.7.

3.2 Mathematical Modeling in Eulerian formalism

In the compression molding process, we consider a non-Newtonian flow through deformable porous material. Deformable porous material used in compression molding process is isotropic and homogeneous. Moreover, continuity equation and conservation of momentum is written for both fluid and solid phases. The density of each phase is assumed constant which allows us to write the continuity equation of each phase as

$$\frac{\partial \phi^f}{\partial t} + \nabla \cdot (\phi^f \mathbf{v}^f) = 0, \quad (3.1)$$

and

$$\frac{\partial \phi^s}{\partial t} + \nabla \cdot (\phi^s \mathbf{v}^s) = 0, \quad (3.2)$$

where ϕ^f and ϕ^s are fluid and solid volume fractions, respectively, \mathbf{v}^f is the velocity of fluid phase and \mathbf{v}^s is the velocity of solid phase in the mixture. The conservation of linear momentum for small deformation and velocity can be written as [11]

$$\nabla \cdot (P\mathbf{I} + \mathbf{T}') = 0, \quad (3.3)$$

where P is pore pressure of non-Newtonian fluid, \mathbf{I} is an identity tensor, and \mathbf{T}' is the excess stress, which is positive in compression. Darcy's law for power-law fluid can be written as [9]

$$\mathbf{v}^f - \mathbf{v}^s = \left(-\frac{\bar{\kappa}(\mathbf{F})}{\phi^f \mu} \nabla P \right)^{\frac{1}{n}}, \quad (3.4)$$

where n is power law index, μ is viscosity of non-Newtonian fluid filled in deformable porous media and $\bar{\kappa}$ is the permeability tensor which depends on the deformation gradient \mathbf{F} of solid phase defined as

$$\mathbf{F}_{ij} = \frac{\partial x_i}{\partial \xi_j}, \quad (3.5)$$

where \vec{x}_i are the actual coordinates and $\vec{\xi}_j$ are the coordinates in reference configuration when pile is not compressed. We now consider the composite velocity \mathbf{v}^c in terms of solid velocity \mathbf{v}^s and liquid velocity \mathbf{v}^f as

$$\mathbf{v}^c = \phi^s \mathbf{v}^s + \phi^f \mathbf{v}^f, \quad (3.6)$$

where $\phi^s + \phi^f = 1$. Note that for the rest of the derivation, we use the following notations $\phi^s = \phi$ and $\phi^f = 1 - \phi$.

Combining (3.1) and (3.2) and using the relations $\phi^s + \phi^f = 1$ and equation (3.6), we obtain

$$\nabla \cdot \mathbf{v}^c = 0. \quad (3.7)$$

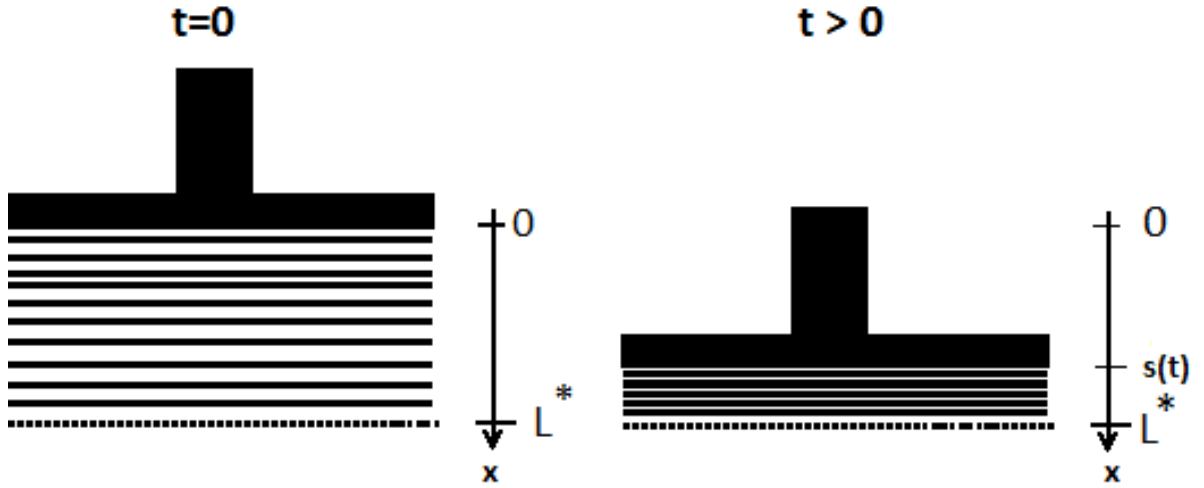


FIGURE 3.1: Evolution of a system. Eulerian model is formulated in the reference frame, the x -axis. The origin $x = 0$ corresponds to the piston position at time $t = 0$. L^* represents the initial height of preimpregnated (prepreg) layers, and $s(t)$ be the piston position at time $t > 0$.

Now we transform our problem in one dimension setting by considering the motion of the piston along x -axis as shown in Figure 3.1. Suppose $L(t)$ and $s(t)$ be the height and position of piston at any time t with respect to principal direction x . Mathematically, $s(t)$ can be written as

$$s(t) = L^* - L(t), \tag{3.8}$$

where L^* is initial height of preimpregnated layers. The equations (3.2) and (3.7) can be written in the component form as

$$\frac{\partial \phi}{\partial t} - \frac{\partial}{\partial x} [(1 - \phi)v^f] = 0, \tag{3.9}$$

$$\frac{\partial v^c}{\partial x} = 0. \tag{3.10}$$

Note that equation (3.10) shows that composite velocity v^c is space independent. The momentum balance (3.3) can be written in component form as

$$\frac{\partial \sigma}{\partial x} + \frac{\partial P}{\partial x} = 0, \tag{3.11}$$

where $\sigma = (\mathbf{T})_{xx}$. Moreover, Darcy's law (3.4) can be written in component form as

$$v^f - v^s = \left(-\frac{\bar{\kappa}(\phi)}{(1-\phi)\mu} \frac{\partial P}{\partial x} \right)^{\frac{1}{n}}, \quad (3.12)$$

where $\bar{\kappa} = (\bar{\kappa})_{xx}$. Now, the deformation gradient F can be written in one dimensional form as

$$\mathbf{F} = \frac{\partial x}{\partial \xi} = \frac{\phi^*}{\phi}, \quad (3.13)$$

where ϕ^* is the initial solid volume fraction and ϕ is the solid volume fraction at any time t . Note that the relation for stress tensor σ is taken from [157], which depends on solid volume fraction ϕ

$$\sigma(\phi) = 0.3[\exp(25\phi) - \exp(10)]. \quad (3.14)$$

The permeability relation considered in [158] is written as

$$\bar{\kappa}(\phi) = 1.5 \times 10^{-8} \exp(-15\phi). \quad (3.15)$$

After some mathematical manipulation, equation (3.6), with the help of equations (3.11) and (3.12) is written as

$$v^f = v^c + \phi \left(\frac{\bar{\kappa}(\phi)}{(1-\phi)\mu} \frac{\partial \sigma}{\partial x} \right)^{\frac{1}{n}}, \quad (3.16)$$

which on substituting into (3.9) with the help of (3.10) allows us to write the following partial differential equation

$$\frac{\partial \phi}{\partial t} = \frac{\partial}{\partial x} \left[\phi \left(\frac{\bar{\kappa}(\phi)}{(1-\phi)\mu} \sigma'(\phi) \frac{\partial \phi}{\partial x} \right)^{\frac{1}{n}} (1-\phi) \right] - v^c \frac{\partial \phi}{\partial x}, \quad (3.17)$$

where

$$\sigma'(\phi) = \frac{d\sigma}{d\phi}.$$

It is worth mentioning that equation (3.17) is subject to a moving domain. Moving domain problem is difficult to handle numerically. Therefore, our aim in the next section is to transform equation (3.17) to a fixed domain using the Lagrangian transformation.

3.3 Lagrangian One-Dimensional Model

The problem developed in the previous section is nonlinear and is characterized by a moving domain that gives rise to several mathematical difficulties. Therefore, we consider the set of Lagrangian coordinates fixed on the solid skeleton. Let ξ be the independent variable that labels the solid particles and $x = x(\xi, t)$ be the position of particle at any time t . Initially, at time $t = 0$, height of prepreg is L^* and $0 \leq \xi \leq L^*$. In Lagrangian model, it is convenient to consider void ratio r , defined as ratio of volume fraction of infiltrated liquid to volume fraction of solid, which can be written mathematically as

$$r = \frac{1 - \phi}{\phi}. \quad (3.18)$$

The stress and permeability relations (3.14) and (3.15) can be written in terms of void ratio r as

$$\sigma(r) = 0.3 \left[\exp\left(\frac{25}{1+r}\right) - \exp(10) \right], \quad (3.19)$$

and

$$\bar{\kappa}(r) = 1.5 \times 10^{-8} \exp\left(-\frac{15}{1+r}\right). \quad (3.20)$$

Obviously, using material coordinates on the solid skeleton, we transform the moving domain $s(t) \leq x \leq L^*$ occupied by the prepreg to fixed domain, $0 \leq \xi \leq L^*$. Deformation gradient \mathbf{F} can be written in terms of void ratio r as

$$\mathbf{F} = \frac{\partial x}{\partial \xi} = \frac{\phi^*}{\phi} = \frac{r+1}{r^*+1}, \quad (3.21)$$

where

$$r^* = \frac{1 - \phi^*}{\phi^*}.$$

Using relation (3.21) with the chain rule of derivative, we can write

$$\frac{\partial(\cdot)}{\partial x} = \frac{\partial \xi}{\partial x} \frac{\partial(\cdot)}{\partial \xi} = \frac{r^* + 1}{r + 1} \frac{\partial(\cdot)}{\partial \xi}. \quad (3.22)$$

Darcy's law (3.12) can be modified as

$$v^f - v^s = \left(-\frac{r^* + 1}{r} \frac{\bar{\kappa}}{\mu} \Sigma(r) \frac{\partial r}{\partial \xi} \right)^{\frac{1}{n}}, \quad (3.23)$$

where

$$\Sigma(r) = \left| \frac{d\sigma(r)}{dr} \right|. \quad (3.24)$$

Note that we have considered the derivative of stress σ with respect to void ratio r in the above equation. We write equation (3.17) in a specific way to transform in Lagrangian coordinates as

$$\frac{\partial \phi}{\partial t} + v^s \frac{\partial \phi}{\partial x} + (v^c - v^s) \frac{\partial \phi}{\partial x} = \frac{\partial}{\partial x} \left[\phi \left(\frac{\bar{\kappa}(\phi)}{(1 - \phi)\mu} \sigma'(\phi) \frac{\partial \phi}{\partial x} \right)^{\frac{1}{n}} (1 - \phi) \right]. \quad (3.25)$$

Combining equations (3.6), (3.11), (3.12) and (3.25), we get

$$\begin{aligned} \left(\frac{d\phi}{dt} \right)_s + \left(\frac{\bar{\kappa}(\phi)}{(1 - \phi)\mu} \sigma'(\phi) \frac{\partial \phi}{\partial x} \right)^{\frac{1}{n}} (1 - \phi) \frac{\partial \phi}{\partial x} \\ = \frac{\partial}{\partial x} \left[\phi \left(\frac{\bar{\kappa}(\phi)}{(1 - \phi)\mu} \sigma'(\phi) \frac{\partial \phi}{\partial x} \right)^{\frac{1}{n}} (1 - \phi) \right], \end{aligned} \quad (3.26)$$

where the notation of total derivative $(\frac{d}{dt})_s$ is used. Now taking into account equations (3.18), (3.22), (3.24) and (3.26), we can write

$$\begin{aligned} \frac{\partial r}{\partial t} + \frac{r(r^* + 1)}{(1 + r)^2} \frac{\partial r}{\partial \xi} \left(\frac{\bar{\kappa}(r)}{r\mu} (r^* + 1) \Sigma(r) \frac{\partial r}{\partial \xi} \right)^{\frac{1}{n}} \\ = -(r^* + 1)(1 + r) \frac{\partial}{\partial \xi} \left[\frac{r}{(1 + r)^2} \left(\frac{\bar{\kappa}(r)}{r\mu} \Sigma(r) (r^* + 1) \frac{\partial r}{\partial \xi} \right)^{\frac{1}{n}} \right]. \end{aligned} \quad (3.27)$$

The appropriate boundary conditions for present problem are written as [11]

$$\frac{\partial r}{\partial \xi}(0, t) = 0, \quad (3.28)$$

and

$$r(L^*, T) = \sigma^{-1}(P_0(t)), \quad (3.29)$$

above equation corresponds to the pressure driven dynamics.

For velocity driven dynamics, right boundary condition can be taken as

$$\begin{aligned} & \frac{\partial r(L^*, t)}{\partial \xi} \\ &= -\frac{\mu}{\Sigma(r(L^*, t))\bar{\kappa}(r(L^*, t))} \frac{r(L^*, t) + 1}{r^* + 1} v_p(t). \quad (\text{velocity driven dynamics}) \end{aligned} \quad (3.30)$$

We propose an initial condition of the following form

$$r(\xi, 0) = \exp\left(\frac{-\xi}{2} + 0.9\right). \quad (3.31)$$

Note that governing equation (3.27) in terms of Lagrangian coordinates describes the changes in void ratio r and ultimately in solid volume fraction ϕ via equation (3.18). It is important to note that equation (3.27) can be reduced to Newtonian fluid case [11], when we set power law index n to be 1. However, our focus in this study is non-Newtonian case where we will consider $n \neq 1$.

3.4 Non-Dimensionalization

The following set of normalized quantities are utilized to non-dimensionalize the governing equation (3.27),

$$Y = \frac{\xi}{L^*}, \quad (3.32)$$

$$T = \frac{t}{t_c}, \quad (3.33)$$

$$\psi(r) = \frac{r+1}{r^*+1} \frac{\Sigma(r)\bar{\kappa}(r)}{\Sigma(r^*)\bar{\kappa}(r^*)}, \quad (3.34)$$

$$V(t) = v_p(t)/V_{ref}, \quad (3.35)$$

$$T_f = \frac{t_f}{t_c}, \quad (3.36)$$

where $V_{ref} = \frac{L^*}{t_c}$, $t_c = \frac{\mu L^*}{r^*+1} \frac{1}{\Sigma(r^*)\bar{\kappa}(r^*)}$ and $\psi(r)$ is a positive smooth function for $r \geq 0$. In order to carry out numerical simulation, we assume that initial height $L^* = 6 \times 10^{-3}$ m, viscosity $\mu = 10$ Pas and initial solid volume fraction $\phi^* = 0.4$ (i.e., $r^* = 1.5$) [11]. Following Farina *et al.* [11], we consider $t_c = 146.5$ sec, $V_{ref} = 4.095 \times 10^{-5} ms^{-1}$ and $T_f = 0.1$. Where T_f is the dimensionless time whereas t_c is the dimensional time. Using the dimensionless variables (3.32)-(3.36) in equation (3.27)-(3.30), we get the following non-dimensional problem

$$\begin{aligned} \frac{\partial r}{\partial T} = & -(61041.67)(-4.6875 \times 10^{-6})^{\frac{1}{n}} r^{1-\frac{1}{n}} (1+r)^{-2-\frac{2}{n}} \left(\frac{\partial r}{\partial Y} \right)^{1+\frac{1}{n}} \exp\left(\frac{10}{n(1+r)} \right) \\ & -(61041.67)(-4.6875 \times 10^{-6})^{\frac{1}{n}} (1+r) \exp\left(\frac{10}{n(1+r)} \right) \times \\ & \left[\left(1 - \frac{1}{n} \right) r^{-\frac{1}{n}} (1+r)^{-2-\frac{2}{n}} \left(\frac{\partial r}{\partial Y} \right)^{1+\frac{1}{n}} \right. \\ & + \left(-2 - \frac{2}{n} \right) r^{1-\frac{1}{n}} (1+r)^{-3-\frac{2}{n}} \left(\frac{\partial r}{\partial Y} \right)^{1+\frac{1}{n}} \\ & + \left(-\frac{10}{n} \right) r^{1-\frac{1}{n}} (1+r)^{-4-\frac{2}{n}} \left(\frac{\partial r}{\partial Y} \right)^{1+\frac{1}{n}} \\ & \left. + \left(\frac{1}{n} \right) r^{1-\frac{1}{n}} (1+r)^{-2-\frac{2}{n}} \left(\frac{\partial r}{\partial Y} \right)^{\frac{1}{n}-1} \frac{\partial^2 r}{\partial Y^2} \right], \quad (3.37) \end{aligned}$$

$$r(Y, 0) = \exp\left(\frac{-Y}{2} + 0.9 \right), \quad 0 \leq Y \leq 1, \quad (3.38)$$

$$\frac{\partial r(0, T)}{\partial Y} = 0, \quad (3.39)$$

$$r(1, T) = \sigma^{-1}(P(T)), \quad (3.40)$$

or

$$\frac{\partial r(1, T)}{\partial Y} = -\frac{L^* V_{ref} \mu}{\bar{\kappa}(r(1, T)) \Sigma(r(1, T))} \frac{1 + r(1, T)}{1 + r^*} V(T). \quad (3.41)$$

$P(T)$ and $V(T)$ are involved in the above equations and will be explained in the next section.

3.5 Pressure and Velocity Driven Dynamics

We use Matlab's function *pdepe* to solve one-dimensional parabolic and elliptic partial differential equation (3.37) together with the requisite periodic boundary conditions and initial conditions. It relies on the Method of Lines, where we discretize the space derivatives by using finite differences and leaving the time variable continuous. The resulting ODEs are then solved using *ode15* solver.

Following Farina *et al.* [11], we consider either the pressure or velocity driven dynamics at $x = L^*$. Various relations that we use in equations (3.40) and (3.41) for applied pressure $P(T)$ and velocity $V(T)$ are given below

$$P_1 = 1250000 \sin \left[\frac{25}{3} \pi T \right], \quad (3.42)$$

$$P_2 = 612500 [1 - \cos(15\pi T)], \quad (3.43)$$

$$P_3 = 61250000 T^2, \quad (3.44)$$

$$V_1 = 3 [1 - \cos(20\pi T)], \quad (3.45)$$

$$V_2 = 4.14 \sin \left[\frac{\pi}{4} (30T + 1) \right], \quad (3.46)$$

$$V_3 = \frac{471}{100} \sin \left[\frac{\pi}{2} (10T + 1) \right]. \quad (3.47)$$

Figure 3.2 shows various pressures (3.42)-(3.44) applied to the piston as a function of dimensionless time. Solid line corresponds to the pressure P_1 , dashed line corresponds to the pressure P_2 and dotted one corresponds to the P_3 . Profile of P_1 and P_2 increase with increase in time and then begin to decrease, increase in P_1 is more than P_2 . Graph shows that P_3 increases with increase in time.

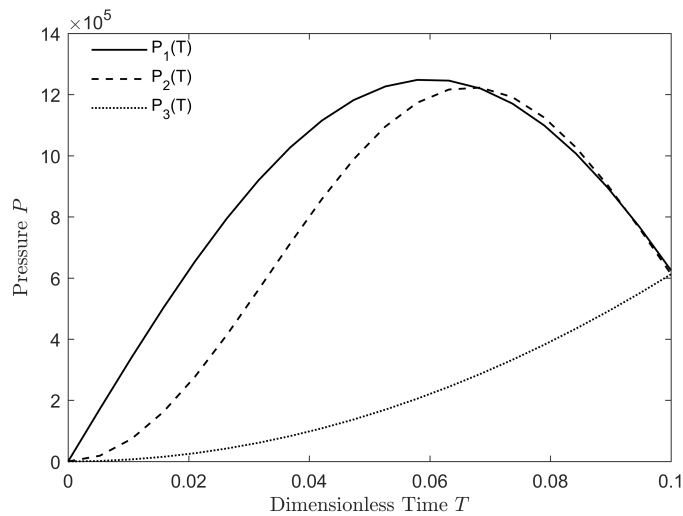


FIGURE 3.2: Pressure applied to a piston as a function of dimensionless T .

Figure 3.3 shows various piston velocities (3.45)-(3.47) as a function of dimensionless time. Solid line corresponds to the V_1 , dashed line corresponds to the V_2 and dotted one corresponds to the V_3 . Profile shows that V_1 increases from $T = 0$ to $T = 0.05$ and then begins to decrease and falls to zero at $T = 0.1$. Graphical results show that piston velocities V_2 and V_3 decrease with time and fall to zero at $T = 0.1$.

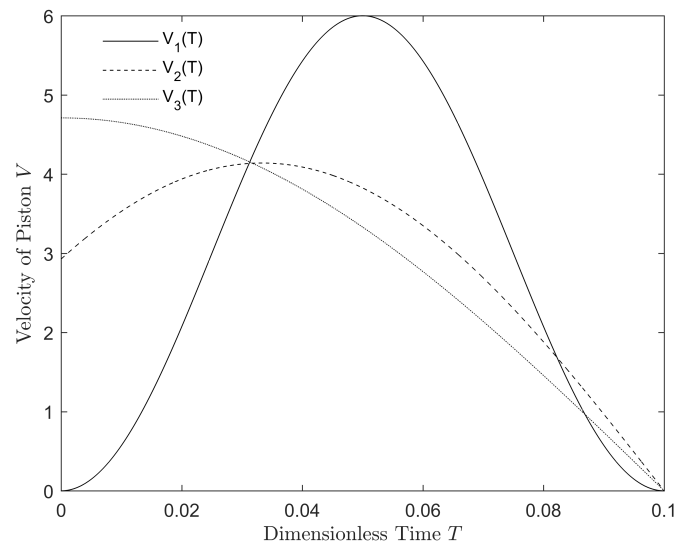


FIGURE 3.3: Velocity of a piston V as a function of the dimensionless time T .

Equations (3.42)-(3.47) have completed all the aspects of the problems. In Figure 3.4, solid volume fraction profile is plotted as a function of lagrangian coordinate Y . Using *pdepe*, equation (3.37) gives same results for solid volume fraction at different nodes for Y e.g., $N_Y = 20, 40, 80$ which shows the convergence of numerical technique.

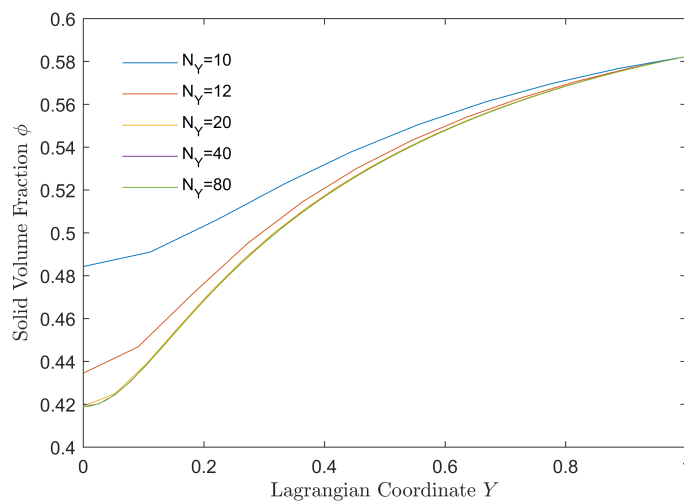


FIGURE 3.4: Solid volume fraction ϕ against space variable Y using $P_1(T)$ when $n = 1$

It is worth mentioning here that by substituting the power-law index $n = 1$ in equation (3.37), the graph of solid volume fraction ϕ for the velocity $V_3(T)$ reported by Farina [11], is recovered successfully as shown in Figure 3.5.

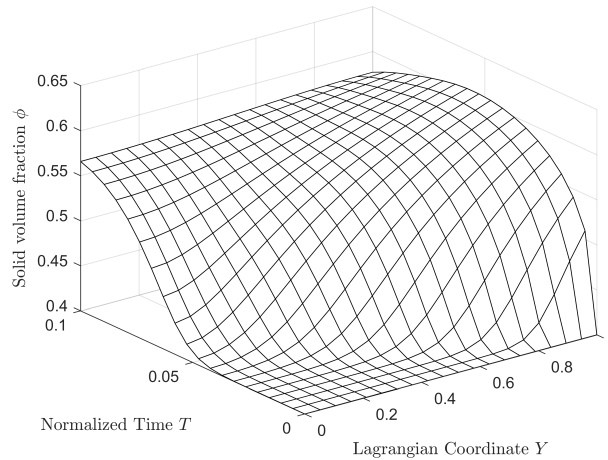


FIGURE 3.5: Solid volume fraction ϕ against space variable Y and time T using $V_3(T)$ when power-law index $n = 1$.

3.6 Results and Discussion

This section contains the output of our numerical simulations for different values of power-law index n . In particular, the effect of power-law index on solid volume fraction under pressure and velocity controlled dynamics is illustrated graphically. Graphical illustration show results for shear-thinning and shear-thickening fluids using various relations of piston pressures and piston velocities.

Figure 3.6 shows the evolution of the solid volume fraction $\phi(Y, T)$ for shear-thinning fluid ($n = 0.90$), when $P_1(T)$ (3.42) is used as a driving pressure. Initially, there is no change in ϕ , however, solid volume fraction ϕ rises with time at a constant rate and attains the maximum value of 0.58. At the start of the experiment, compression pushes the pile downward, which in turn pushes the fluid out of the pile. This is consistent with the fact that the viscosity of shear-thinning fluid decreases with increasing shear rate.

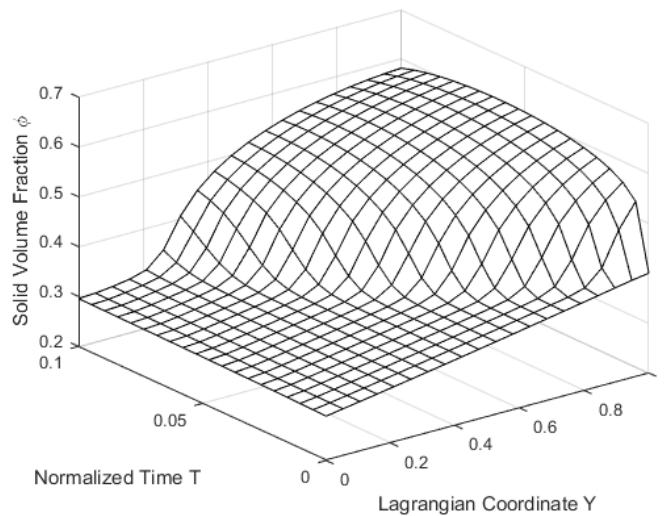


FIGURE 3.6: Solid volume fraction ϕ against space variable Y and time T using $P_1(T)$ when power-law index $n = 0.90$.

Figure 3.7 shows the evolution of the solid volume fraction $\phi(Y, T)$ for shear-thickening fluid ($n = 1.1$), when $P_1(T)$ is used as a driving pressure. Solid volume fraction ϕ grows with time, gives rise to homogeneous ϕ in a neighborhood of draining surface, i.e. $Y = 1$. Due to decrease in the pressure $P_1(T)$ from the middle of a procedure, increase in the solid volume fraction ϕ can be noted. This result is consistent with the fact that the viscosity of shear-thickening fluid increases with decrease in shear-rate.

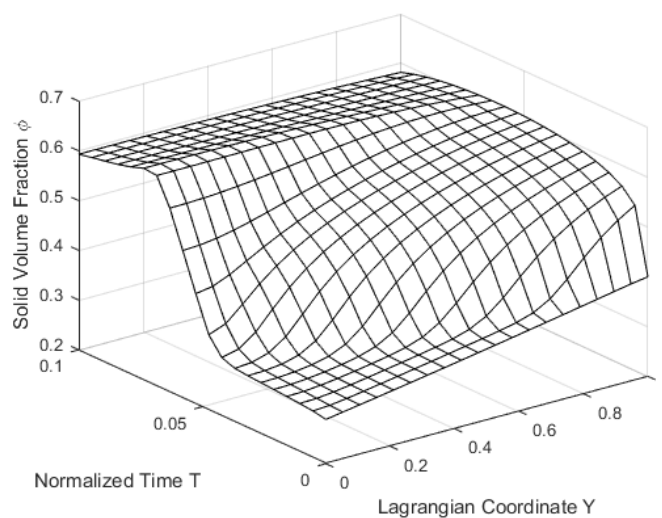


FIGURE 3.7: Solid volume fraction ϕ against space variable Y and time T using $P_1(T)$ for power-law index $n = 1.1$.

Figure 3.8 shows evolution of solid volume fraction ϕ for power-law fluid when the driving pressure $P_2(T)$ given by the relation (3.43) is used. When $n = 0.90$ (shear-thinning fluid), a linear behavior is observed initially, however, solid volume fraction ϕ attains maximum value 0.58 at final time $T = T_f$. It is noted that increase in solid volume fraction slows down before the end of procedure. This is due to the fact that decrease in the pressure $P_2(T)$, strain-rate gets smaller and ultimately viscosity of shear-thinning fluid increases.

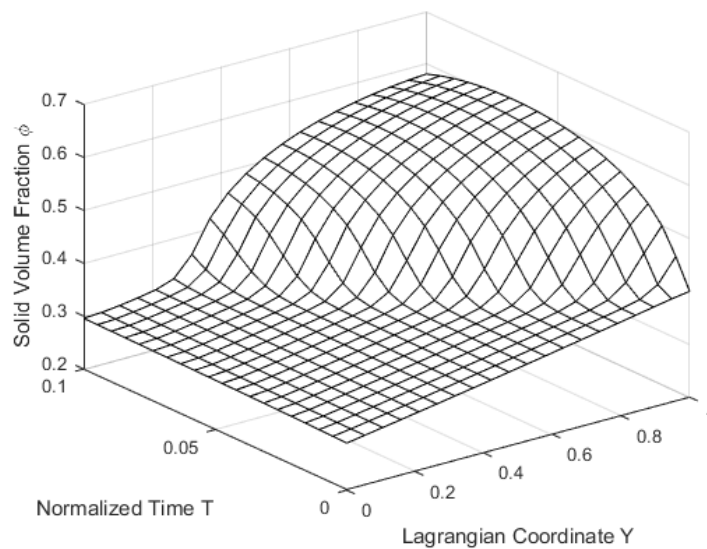


FIGURE 3.8: Solid volume fraction ϕ against space variable Y and time T using $P_2(T)$ for power-law index $n = 0.90$.

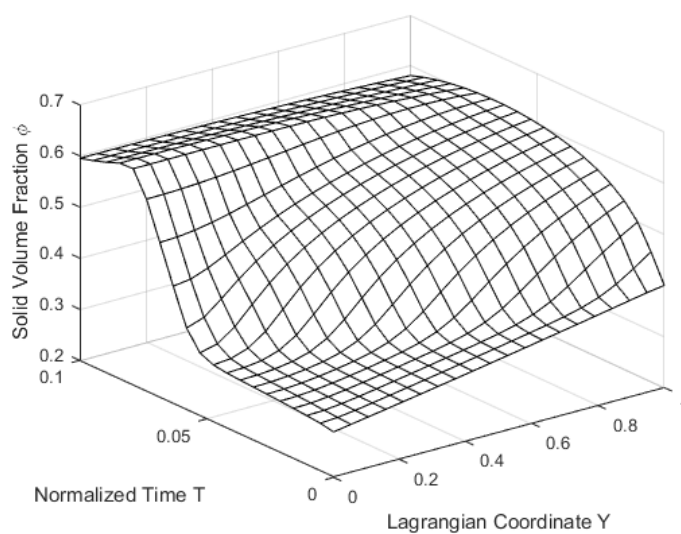


FIGURE 3.9: Solid volume fraction ϕ against space variable Y and time T using $P_2(T)$ for power-law index $n = 1.1$.

On the other hand, Figure 3.9 shows results when non-Newtonian fluid with index $n = 1.1$ (shear-thickening fluid) is considered. The solid volume fraction ϕ shows linear behavior near boundaries in both figures, whereas the maximum growth of ϕ can be observed from time $T = 0.05$ to $T = 0.08$. This is due to the fact that decrease in pressure $P_2(T)$, strain-rate gets smaller and viscosity of shear-thickening fluid decreases. Imbibition of fluid has been noted before the end of experiment.

Figure 3.10 and Figure 3.11 correspond to flow of power-law fluid through preimpregnated pile, for power-law indices $n = 0.90$ and $n = 1.1$, respectively, when pressure function $P_3(T)$ is utilized. For power-law index $n = 0.90$, initially smooth growth in solid volume fraction can be observed, which gradually increases to maximum value of 0.58 in a final state. As pressure $P_3(T)$ continuously increases from start to end of the procedure, and strain-rate becomes higher and higher. So, viscosity of shear-thinning fluid decreases and solid volume fraction increases. For power-law index $n = 1.1$, it reaches to maximum value of 0.59 and gives rise to an inhomogeneous solid volume fraction ϕ at $T = T_f$. It is consistent with the fact that increase in strain-rate increases the viscosity of shear-thickening fluid. Resistance in the flow has been occurred due to increase in viscosity of fluid.

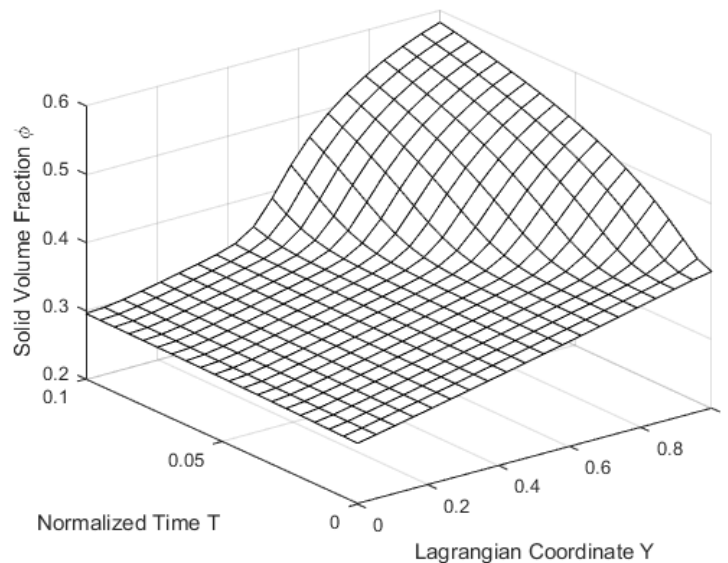


FIGURE 3.10: Solid volume fraction ϕ against space variable Y and time T using $P_3(T)$ for power-law index $n = 0.90$.

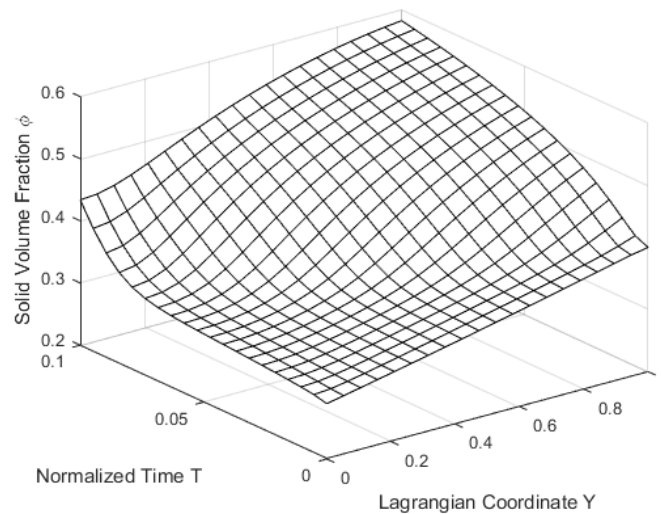


FIGURE 3.11: Solid volume fraction ϕ against space variable Y and time T using $P_3(T)$ for power-law index $n = 1.1$.

We now move on to discuss the velocity driven dynamics. Figure 3.12 shows an increase in solid fraction ϕ for the case when driving velocity V_1 is given by equation (3.47) for index $n = 0.80$ (shear-thinning fluid). There is no change in ϕ at the beginning, however, there is rapid increase of ϕ in a neighborhood of $Y = 1$.

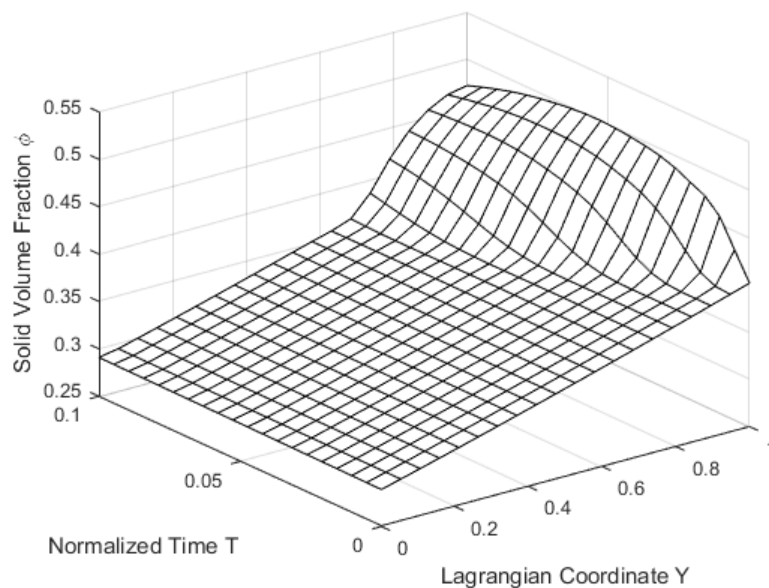


FIGURE 3.12: Solid volume fraction ϕ against space variable Y and time T using $V_1(T)$ for power-law index $n = 0.80$.

Figure 3.13 shows an increase in solid fraction $\phi(Y, T)$ for the case when driving velocity V_1 given by equation (3.45) is used for $n = 1.3$ (shear-thickening fluid).

From the upper extremities of the graph, an homogeneous solid volume fraction can be observed. During the compression molding process, imbibition of shear thickening fluid in porous deformable media can also be observed at $T = 0.05$ and $T = 0.08$.

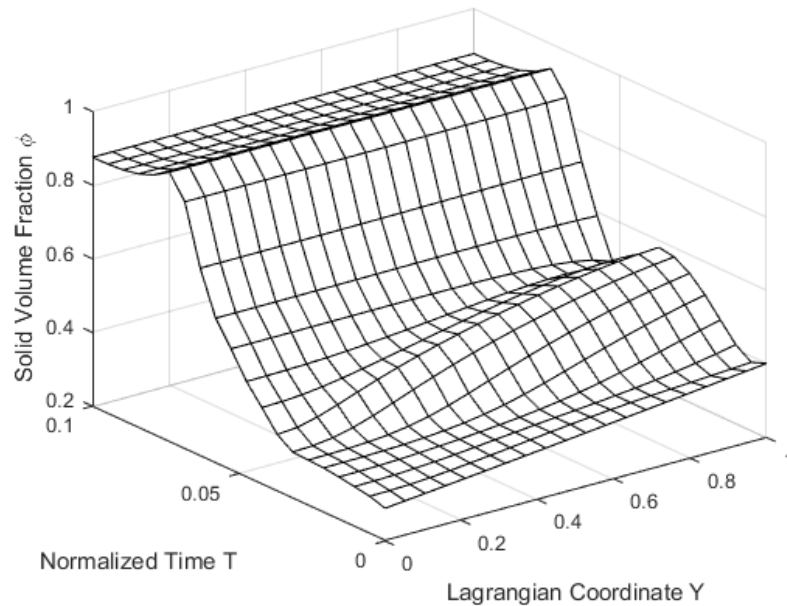


FIGURE 3.13: Solid volume fraction ϕ against space variable Y and time T using $V_1(T)$ for power-law index $n = 1.3$.

Figure 3.14 and Figure 3.15 correspond to the flow of power-law fluid through porous media, for power law index $n = 0.90$ and $n = 1.1$, respectively. In these figures velocity can be taken to be V_2 . The velocity of fluid not only alters the rate of growth of solid volume fraction ϕ but also vary the compression rate. For power-law index $n = 0.90$ (shear thinning fluid), there is increase in solid volume fraction ϕ at a constant rate, imbibition of fluid can be also observed at $T = T_f$. This is due to the fact that decrease in velocity $V_2(T)$, decreases the shear-rate and ultimately decreases the viscosity of shear-thinning fluid.

For the case of shear-thickening fluid, ($n = 1.1$), preimpregnated pile reaches an homogeneous solid volume fraction ϕ at $T = T_f$ which is shown in Figure 3.15. This is due to the fact that $V_2(T)$ increases with time and then begins to decrease, ultimately viscosity of shear-thickening fluid increases with decreasing shear-rate.

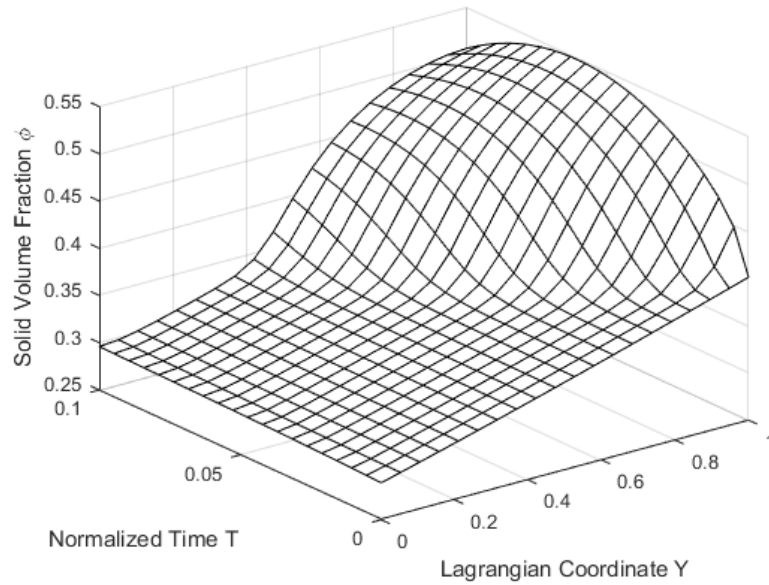


FIGURE 3.14: Solid volume fraction ϕ against space variable Y and time T using $V_2(T)$ for power-law index $n = 0.90$.

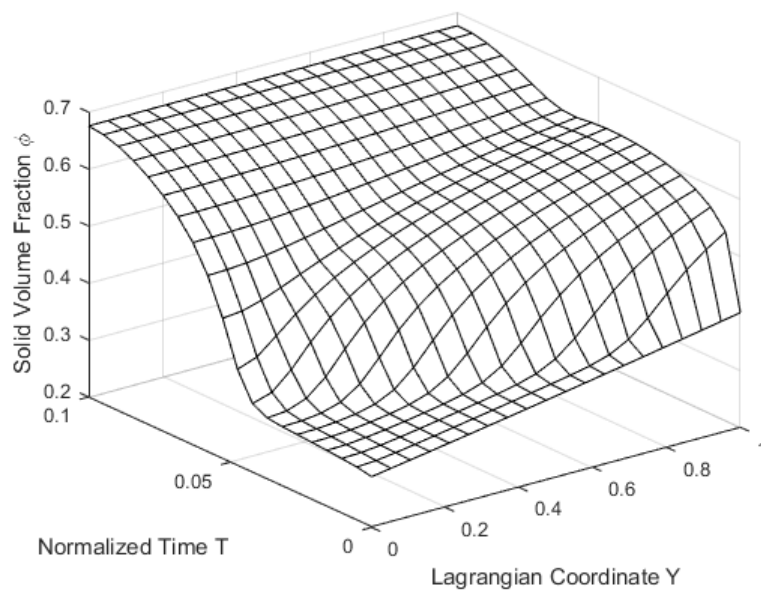


FIGURE 3.15: Solid volume fraction ϕ against space variable Y and time T using $V_2(T)$ for power-law index $n = 1.1$.

Figure 3.16 and Figure 3.17 correspond to flow of power-law fluid through pre-impregnated pile, for power-law indices $n = 0.90$ and $n = 1.1$, respectively, when pressure function $V_3(T)$ is utilized. For power-law index $n = 0.90$, initially smooth growth in solid volume fraction can be observed, which gradually increases to

maximum value of 0.52 in a final state, whereas for power-law index $n = 1.1$, pre-impregnated pile reaches an homogeneous ϕ at $T = T_f$.

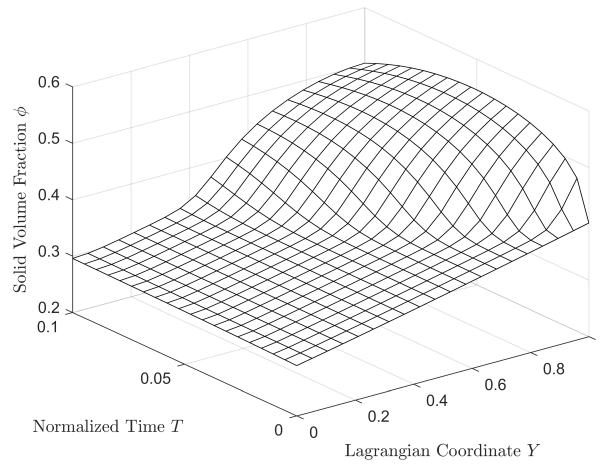


FIGURE 3.16: Solid volume fraction ϕ against space variable Y and time T using $V_3(T)$ for power-law index $n = 0.90$.

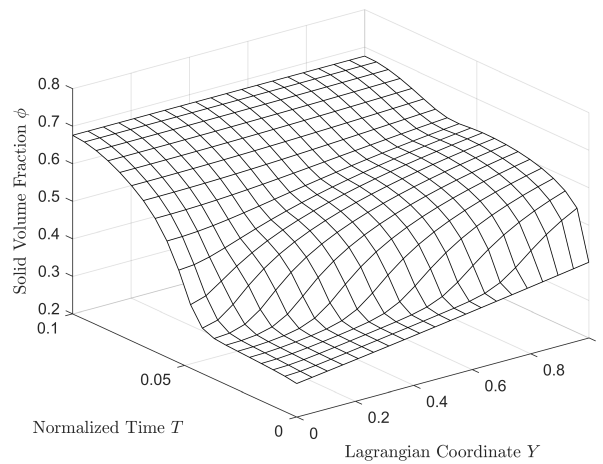


FIGURE 3.17: Solid volume fraction ϕ against space variable Y and time T using $V_3(T)$ for power-law index $n = 1.1$.

Figure 3.6 and Figure 3.12 show the comparison of solid volume fraction $\phi(Y, T)$ for shear-thinning fluid using $P_1(T)$ and $V_1(T)$, respectively. Exudation of fluid is much greater for the case of $P_1(T)$ as compared the to case of $V_1(T)$. This observation is due to the fact that viscosity of shear-thinning fluid decreases with increasing shear rates.

Figure 3.7 and Figure 3.13 show the comparison of solid volume fraction $\phi(Y, T)$ for shear-thickening fluid using $P_1(T)$ and $V_1(T)$, respectively. For the case of $P_1(T)$, solid volume increases but the overall increase is less as compared to the case of V_1 . Imbibition of fluid can be observed at the middle and at the end for the case of $V_1(T)$, whereas it can be observed at the end for the case of $P_1(T)$.

Figure 3.8 and Figure 3.14 show the comparison of solid volume fraction $\phi(Y, T)$ for shear-thinning fluid using $P_2(T)$ and $V_2(T)$, respectively. Negligible increase in the start, but homogenous volume fraction in the end can be observed for the case of $P_2(T)$ as compared to the case of $V_2(T)$. This is consistent with the fact that continuous decrease in the value of $V_2(T)$ decreases the shear-rate and ultimately increases the viscosity of shear-thinning fluid.

Figure 3.9 and Figure 3.15 show the comparison of solid volume fraction $\phi(Y, T)$ for shear-thickening fluid using $P_2(T)$ and $V_2(T)$, respectively. More increase in solid volume fraction $\phi(Y, T)$ can be noted for the case of $V_2(T)$ as compared to the case of $P_2(T)$. This is consistent with the fact that decrease in the value of $V_2(T)$ decreases the shear-rate and ultimately decreases the viscosity of fluid.

Figure 3.10 and Figure 3.16 show the comparison of solid volume fraction $\phi(Y, T)$ for shear-thinning fluid using $P_3(T)$ and $V_3(T)$, respectively. More increase in solid volume fraction can be observed for the case of $P_3(T)$ as compared to the case of $V_3(T)$. As value of $P_3(T)$ increases from $T = 0$ to $T = T_f$, ultimately shear-rate increases which decreases the viscosity of shear-thinning fluid and increases the exudation of fluid. Figure 3.11 and Figure 3.17 show the comparison of solid volume fraction $\phi(Y, T)$ for shear-thickening fluid using $P_3(T)$ and $V_3(T)$, respectively. Increase in solid volume fraction is significant for the case of $V_3(T)$ as compared to the case of $P_3(T)$. This is due to the fact that value of V_3 decreases from $T = 0$ to $T = T_f$, ultimately shear-rate decreases and ultimately decreases the viscosity of shear-thickening fluid.

We can notice for velocity V_1 , the simulations for shear thickening fluid correspond to an initial smooth contact between deformable porous material and piston are

more stressing for the material than velocity V_2 which corresponds to an impact between pre-impregnated pile and piston.

3.7 Conclusion

In this chapter, we have extended the work of Farina *et al.* [11] to non-Newtonian fluid using the continuum mixture theory approach keeping in mind an industrial process which is used for manufacturing of composite materials. The model presented here is identical to ones in previous works of Barry *et al.* [159], Preziosi *et al.*, [160], Anderson [161] and Siddique *et al.* [9], etc. We have shown the simulations, generated by dynamics controlled either by velocity of the piston or pressure applied to the piston.

Pressure Driven Dynamics

- In the case of shear-thinning fluid, compression gives rise to a sudden increase of solid volume fraction ϕ near the draining surface, which causes the preimpregnated pile to a final state in which ϕ is greatly inhomogeneous.
- In shear thickening fluids, there is an increase in solid volume fraction but compression brings the material into a final state in which ϕ is almost homogeneous. Results show imbibition of a shear-thickening fluid into a ‘pre-impregnated’ pile.

Velocity Driven Dynamics

- In the case of shear-thinning fluid, the compression of prepreg starts from the draining surface.
- For the case of shear-thickening fluid, we observe that the processes correspond to an initial smooth contact between prepreg and piston are more

stressing for the material than those corresponding to an impact between pile and piston.

Here, we have outlined the mathematical modeling of a compression molding process using power-law fluid that needs to be explored in many possible directions both experimentally and mathematically. There are many open questions that still need to be addressed, such as the inclusion of other non-Newtonian fluid models, along with comparison with experiments.

Chapter 4

Ion-induced Swelling Behavior of Articular Cartilage due to Non-Newtonian flow and its Effects on Fluid Pressure and Solid Displacement

4.1 Introduction

The aim of this chapter is to investigate the effects of the non-Newtonian fluid flow on the deformation of articular cartilage equilibrated in sodium chloride (NaCl) solution. A sample of articular cartilage is considered which is assumed to be thin, rectangular, isotropic, linearly elastic solid and from the midzone of the cartilage. In the presence of a charge due to the ion- concentration of the bathing solution, a mathematical model of this problem is developed and discussed using the biphasic mixture theory approach. Suitable normalized quantities are used to non-dimensionalize the governing set of equations in terms of ion-concentration, fluid pressure and solid displacement.

The analytical solution is provided for the ion-concentration, whereas for the case of fluid pressure and solid displacement, equations are solved numerically using the Method of Lines. The effects of various emerging parameters such as power-law index and time on the fluid pressure and solid displacement profiles are illustrated graphically.

In Section 4.2, a mathematical model is developed using biphasic mixture theory. One-dimensional mathematical model is presented in Section 4.3. Suitable dimensional parameters are used to non-dimensionalize the governing set of coupled equations in section 4.4. Section 4.5 is devoted to the solution methodology. The results along with discussions have been presented in Section 4.6 followed by the conclusion in Section 4.7.

4.2 Model Development

We consider a rectangular strip of bovine articular cartilage which is removed from the midzone of the tissue. Specimen dimensions are measured in a continuous supply of salt solution of non-Newtonian fluid as shown in Figure 4.1. The dimensions of the sample tissue are approximately $\ell = 1.5 \times 10^{-2}$ m, $w = 1.7 \times 10^{-3}$ m and $h = 2 \times 10^{-4}$ m [27]. The planar coordinates \bar{x} , \bar{y} , \bar{z} are taken along height, width and length directions, respectively.

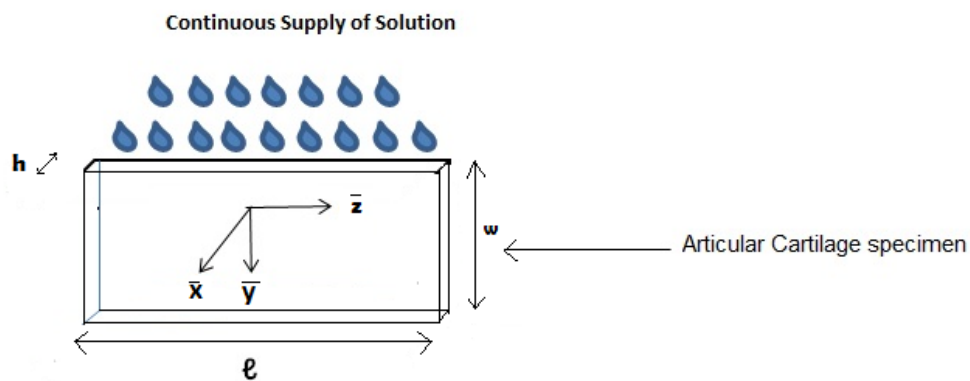


FIGURE 4.1: Schematic diagram of a rectangular strip of cartilage specimen under continuous supply of salt solution. This geometry shows the cartilage dimensions (h , w and ℓ) along the planar coordinates \bar{x} , \bar{y} and \bar{z} respectively.

Articular cartilage can be modeled like other biological tissues [162–164], as a mixture composed of interstitial fluid and permeable solid matrix [27, 96]. The mathematical model is developed using continuum theory of mixture on the assumptions that components of tissue are intrinsically incompressible, and that the solid organic matrix of cartilage is linearly elastic, homogeneous and isotropic. The basic idea behind the mixture theory is that each phase of mixture is continuous and occupies each point in the space at each instant of time. We also assume that fluid considered in this problem is a non-Newtonian that follows the power-law model. Viscosity of fluid is neglected except for its role in diffusional drag as interstitial fluid flows through the cartilage. The density of each phase is assumed to be constant which allows us to write the continuity equation of each phase as [165]

$$\frac{\partial \phi^\beta}{\partial t} + \nabla \cdot (\phi^\beta \mathbf{v}^\beta) = 0, \quad (4.1)$$

where $\beta = f, s$ corresponds to fluid and solid phase respectively, \mathbf{v}^β and ϕ^β is velocity and volume fraction of β phase respectively. The continuity equation for the biphasic mixture of fluid and solid phase is written as [165, 166]

$$\nabla \cdot \mathbf{v}^f = -\alpha \nabla \cdot \mathbf{v}^s, \quad (4.2)$$

where α is the ratio of solid volume fraction ϕ^s to fluid volume fraction ϕ^f . The Navier stokes equation for biphasic mixture of β phase can be written as

$$\rho \frac{D^\beta \mathbf{v}^\beta}{Dt} = \text{div } \mathbf{T}^\beta + \rho^\beta \mathbf{b}^\beta + \boldsymbol{\pi}^\beta, \quad (4.3)$$

where $\frac{D^\beta}{Dt}$ is the material time derivative, \mathbf{T}^β is partial stress, \mathbf{b}^β is the body force per unit mass and $\boldsymbol{\pi}^\beta$ is the local diffusive force of β phase. Using Newton's third law of motion for the local diffusive forces of solid and liquid phases implies that $\boldsymbol{\pi}^s = -\boldsymbol{\pi}^f$. Due to small mass, velocities and deformation, the influence of body force and inertial terms are negligible and momentum balance (4.3) reduces to

$$\nabla \cdot \mathbf{T}^\beta + \boldsymbol{\pi}^\beta = 0. \quad (4.4)$$

Following Myers *et al.* [27], solid stress along with contribution from ionic effects can be written as

$$\mathbf{T}^s = -\alpha\bar{p}\mathbf{I} + 2\mu_s\mathbf{e} + \lambda_s e\mathbf{I} + \alpha_c(2\mu_s + 3\lambda_s)\bar{C}\mathbf{I}, \quad (4.5)$$

where λ_s , μ_s are Lamé's constants for elastic solid matrix, \bar{p} is the interstitial fluid pressure, \mathbf{I} is an identity tensor, \mathbf{e} is the infinitesimal strain tensor of solid phase, $e = \text{trace}(\mathbf{e})$ and $\alpha_c(2\mu_s + 3\lambda_s)\bar{C}\mathbf{I}$ is the linear contribution of ion concentration. The fluid stress relation for linear biphasic model is given by [27]

$$\mathbf{T}^f = -\bar{p}\mathbf{I}. \quad (4.6)$$

The equation of diffusive resistance for non-Newtonian power-law fluid can be written as [9]

$$\boldsymbol{\pi}^s = -\boldsymbol{\pi}^f = K |\mathbf{v}^f - \mathbf{v}^s|^{n-1} (\mathbf{v}^f - \mathbf{v}^s), \quad (4.7)$$

where n corresponds to the power-law index and K represents coefficient of diffusive resistance. Now substituting equation (4.7) into equation (4.4), allow us to write the following relations

$$\boldsymbol{\nabla} \cdot \mathbf{T}^s + K |\mathbf{v}^f - \mathbf{v}^s|^{n-1} (\mathbf{v}^f - \mathbf{v}^s) = 0, \quad (4.8)$$

$$\boldsymbol{\nabla} \cdot \mathbf{T}^f - K |\mathbf{v}^f - \mathbf{v}^s|^{n-1} (\mathbf{v}^f - \mathbf{v}^s) = 0. \quad (4.9)$$

Using equation (4.6) into (4.9) gives

$$\boldsymbol{\nabla}\bar{p} + K |\mathbf{v}^f - \mathbf{v}^s|^{n-1} (\mathbf{v}^f - \mathbf{v}^s) = 0. \quad (4.10)$$

Combining equations (4.5) and (4.8), yields

$$-\alpha\boldsymbol{\nabla}\bar{p} + 2\mu_s\boldsymbol{\nabla}\cdot\mathbf{e} + \lambda_s\boldsymbol{\nabla}e + \alpha_c(3\lambda_s + 2\mu_s)\boldsymbol{\nabla}\bar{C} + K |\mathbf{v}^f - \mathbf{v}^s|^{n-1} (\mathbf{v}^f - \mathbf{v}^s) = 0. \quad (4.11)$$

Elimination of pressure term from equations (4.10) and (4.11), allows to write

$$K|\mathbf{v}^f - \mathbf{v}^s|^{n-1} (\mathbf{v}^f - \mathbf{v}^s) (1 + \alpha) + 2\mu_s \nabla \cdot \mathbf{e} + \lambda_s \nabla e + \alpha_c (3\lambda_s + 2\mu_s) \nabla \bar{C} = 0. \quad (4.12)$$

Until now, we have discussed the vector formulation. The section below is specifically designated for one-dimensional ion-induced deformation of cartilage.

4.3 One-Dimensional Mathematical Model

Following Myers *et al.* [27], we assume that solid displacement and flow field are one-dimensional. The liquid velocity is represented by $v^f(\bar{x}, \bar{t})$ and solid displacement by $\bar{u}(\bar{x}, \bar{t})$ of cartilage in the direction of thickness. Integrating conservation of mass (4.2) and using $v^s = \partial \bar{u} / \partial \bar{t}$ for solid velocity allows us to write the following equation

$$v^f = -\alpha \frac{\partial \bar{u}}{\partial \bar{t}}. \quad (4.13)$$

Using equation (4.13) in equation (4.12), for one dimensional case gives

$$-(1 + \alpha)^{n+1} K \left(\frac{\partial \bar{u}}{\partial \bar{t}} \right)^n + (\lambda_s + 2\mu_s) \frac{\partial^2 \bar{u}}{\partial \bar{x}^2} + \alpha_c (3\lambda_s + 2\mu_s) \frac{\partial \bar{C}}{\partial \bar{x}} = 0. \quad (4.14)$$

The permeability $\bar{\kappa}$ for power law fluid can be written as [96]

$$\bar{\kappa} = \frac{1}{K(1 + \alpha)^{n+1}}. \quad (4.15)$$

It is important to note that permeability for the Newtonian fluid case [165] can be recovered when we substitute $n = 1$ in the above equation. The another form of the permeability that was used in [165] is given as $\bar{\kappa} = k_0 \exp(m \partial \bar{u} / \partial \bar{x})$, where m and k_0 are material constants. The term $\partial \bar{u} / \partial \bar{x}$ is related to dilation or strain of cartilage. It is important to mention that value of permeability parameter m for articular cartilage ranges from 0 to 10. It is worth mentioning that $m \neq 0$ represents nonlinear permeability and $m = 0$ corresponds to constant permeability.

Combination of equations (4.14) and (4.15) gives

$$\left(\frac{\partial \bar{u}}{\partial \bar{t}}\right) = \bar{\kappa}^{1/n} \left(H_A \frac{\partial^2 \bar{u}}{\partial \bar{x}^2} + \alpha_c(E) \frac{\partial \bar{C}}{\partial \bar{x}} \right)^{\frac{1}{n}}, \quad (4.16)$$

where $E = 2\mu_s + 3\lambda_s$ and aggregate modulus, $H_A = \lambda_s + 2\mu_s$.

The boundary conditions are given by [27]

$$\bar{u}(0, \bar{t}) = 0, \quad (4.17)$$

and

$$\frac{\partial \bar{u}}{\partial \bar{x}} \left(\pm \frac{h}{2}, \bar{t} \right) = -\frac{\alpha_c E}{H_A} \bar{C} \left(\pm \frac{h}{2}, \bar{t} \right). \quad (4.18)$$

Following [27], the initial condition is given as

$$\bar{u}(\bar{x}, 0) = 0. \quad (4.19)$$

Note that equation (4.16) describes the changes in the solid displacement \bar{u} as a function of time \bar{t} and thickness \bar{x} . Note that for the solution of equation (4.16), we need solution of $\bar{C}(\bar{x}, \bar{t})$. It is important to remark that setting the power-law index n as one and assuming the constant permeability in (4.16), we recover the dimensional governing equation (12) of Myers *et al* [27]. The equation for interstitial pressure $\bar{p}(\bar{x}, \bar{t})$ in component form is found by combining equation (4.10) and equation (4.11)

$$\frac{\partial \bar{p}}{\partial \bar{x}} = \frac{H_A}{(\alpha + 1)} \frac{\partial^2 \bar{u}}{\partial \bar{x}^2} + \frac{\alpha_c E}{(\alpha + 1)} \frac{\partial \bar{C}}{\partial \bar{x}}, \quad (4.20)$$

subject to boundary conditions

$$\bar{p} \left(\pm \frac{h}{2}, \bar{t} \right) = 0. \quad (4.21)$$

Equation (4.20) is the required dimensional governing equation for interstitial fluid pressure as a function of thickness \bar{x} and time \bar{t} . The fluid pressure can be determined once the ion concentration $\bar{C}(\bar{x}, \bar{t})$ and solid displacement $\bar{u}(\bar{x}, \bar{t})$ are known. In order to complete all aspects of this problem it is important to mention the diffusion problem for internal salt concentration for the tissue. Following [27], the diffusion problem is assumed to be uncoupled from the solid displacement and fluid pressure for salt concentration. Moreover, the diffusion of salt is independent of convection effects due to body forces and fluid flow. Note that thickness is very small as compared to length and width of specimen of the cartilage, and NaCl diffusion in one dimension can be written as

$$D \frac{\partial^2 \bar{C}}{\partial \bar{x}^2} = \frac{\partial \bar{C}}{\partial \bar{t}}, \quad (4.22)$$

where D is the diffusion coefficient of salt in articular cartilage and \bar{C} is the molar concentration of salt. subject to the following initial and boundary conditions

$$\bar{C}(\bar{x}, 0) = 0, \quad \frac{\partial \bar{C}}{\partial \bar{x}}(0, \bar{t}) = 0, \quad \bar{C}\left(\pm \frac{h}{2}, \bar{t}\right) = C_0 H(\bar{t}). \quad (4.23)$$

where C_0 is the step rise in concentration of salt imposed on sample of cartilage and $H(\bar{t})$ is the Heaviside step function. It is worth mentioning that solution for the ion concentration $\bar{C}(\bar{x}, \bar{t})$ is determined from equations (4.22) and (4.23) and then used in equations (4.16) and (4.20) to get the solution for solid displacement $\bar{u}(\bar{x}, \bar{t})$ and interstitial fluid pressure $\bar{p}(\bar{x}, \bar{t})$ respectively for the articular cartilage.

4.4 Non-dimensionalization

The following set of normalized quantities are used to non-dimensionalize the solid displacement, fluid pressure and ion concentration equations

$$u = \frac{\bar{u}}{h/2}, \quad (4.24)$$

$$x = \frac{\bar{x}}{h/2}, \quad (4.25)$$

$$p = \frac{\bar{p}}{p_0}, \quad (4.26)$$

$$C = \frac{\bar{C}}{C_0}, \quad (4.27)$$

$$k = \frac{\bar{k}}{k_0}, \quad (4.28)$$

$$t = \frac{\bar{t}D}{(h/2)^2}. \quad (4.29)$$

The equation of solid displacement (4.16) takes the following dimensionless form

$$\frac{\partial u}{\partial t} = R\eta \left[\exp\left(m \frac{du}{dx}\right) \right]^{\frac{1}{n}} \left[\frac{\partial^2 u}{\partial x^2} + Q \frac{\partial C}{\partial x} \right]^{1/n}, \quad (4.30)$$

along with the following initial and boundary conditions

$$u(x, 0) = 0, \quad (4.31)$$

$$u(0, t) = 0, \quad (4.32)$$

$$\frac{\partial u}{\partial x}(\pm 1, t) = -Q, \quad (4.33)$$

where $\eta = \left(\frac{2\kappa_0 H_A}{h}\right)^{\frac{1}{n}-1}$, $Q = \frac{\alpha_c C_0 E}{H_A}$ and $R = \frac{\kappa_0 H_A}{D}$. Choosing $\eta = 1$, a natural length h for the present problem can be written as

$$h = 2\kappa_0 H_A, \quad (4.34)$$

which is the product of power-law velocity and time.

Similarly the dimensionless equation of interstitial fluid pressure (4.20) can be written as

$$\frac{\partial p}{\partial x} = \frac{H}{p_0(\alpha + 1)} \left(\frac{\partial^2 u}{\partial x^2} + Q \frac{\partial C}{\partial x} \right), \quad (4.35)$$

subject to conditions

$$p(\pm 1, t) = 0. \quad (4.36)$$

The equation (4.35) for pressure gradient on integrating and using (4.36), yields

$$p(x, t) = \frac{H_A}{p_0(\alpha + 1)} \left(\frac{\partial u}{\partial x} + QC \right). \quad (4.37)$$

The contribution of power law index n , in the fluid pressure comes from the numerical solution of gradient of solid displacement. Similarly, ion concentration equation can be written as

$$\frac{\partial^2 C}{\partial x^2} = \frac{\partial C}{\partial t}, \quad (4.38)$$

and the conditions

$$C(x, 0) = 0, \quad (4.39)$$

$$\frac{\partial C}{\partial x}(0, t) = 0, \quad (4.40)$$

$$C(\pm 1, t) = H(t). \quad (4.41)$$

The above system of governing equations (4.30), (4.35) and (4.38), subject to boundary conditions (4.31-4.33), (4.36) and (4.39-4.41) closes our system and solution procedure will be discussed in the following section.

4.5 Solution Procedure

First, we discuss the solution for the ion concentration due to dependence of solid displacement and fluid pressure on it. The analytical solution of equation (4.38) is found by using eigenfunction expansion approach. It is worth mentioning here that eigenfunction expansion method may not be used on the relation (4.38) since boundary conditions for the ion-concentration are non-homogeneous. However, this problem can be solved by introducing a new function

$$m(x, t) = H(t) - C(x, t). \quad (4.42)$$

The system for $m(x, t)$ can be written as

$$\begin{cases} m_{xx}(x, t) = m_t(x, t), \\ m(x, 0) = 0, \\ \frac{\partial m}{\partial x}(0, t) = 0. \\ m(1, t) = 0. \end{cases} \quad (4.43)$$

Using separation of variables method by assuming $m(x, t) = X(x)T(t)$, and connecting to a common constant $-\delta$, we get the system of ordinary differential equations (ODEs)

$$\begin{cases} X'' + \delta X = 0, & \text{with } X_x(0) = 0, \quad X(1) = 0, \\ T' + \delta T = 0. \end{cases} \quad (4.44)$$

Auxiliary equation for X is $D^2 + \delta = 0$, whereas auxiliary equation for T is $D + \delta = 0$.

Hence, sum of solutions of $m(x, t)$ satisfying the above boundary conditions have the following form

$$m(x, t) = \sum_{q=0}^{\infty} B_q \cos\left(\frac{(2q+1)\pi x}{2}\right) \exp\left(-\frac{(1+2q)^2\pi^2}{4}t\right), \quad (4.45)$$

where B_q are the constants. Now, we can write a continuous function $f(x)$ on $[0, 1]$ as

$$f(x) = \frac{B_0}{2} + \sum_{q=1}^{\infty} B_q \cos\left(\frac{(2q+1)\pi x}{2}\right), B_q = 2 \int_0^1 f(x) \cos\left(\frac{(2q+1)\pi x}{2}\right) dx, \quad (4.46)$$

where $B_0 = \int_0^1 f(x) dx$. It is worth mentioning here that

1. For $m = n$

$$\int_0^1 \cos(m\pi x) \cos(n\pi x) dx = \frac{1}{2}. \quad (4.47)$$

2. For integers $m \neq n$

$$\int_0^1 \cos(m\pi x) \cos(n\pi x) dx = 0. \quad (4.48)$$

3.

$$f(x) = \begin{cases} -1 & 0 < x < \frac{1}{2} \\ 1 & \frac{1}{2} < x < 1 \end{cases} \quad (4.49)$$

Hence, fourier series for function $f(x)$ can be written as

$$f(x) = \sum_{q=0}^{\infty} B_q \cos\left(\frac{(2q+1)\pi x}{2}\right), \quad B_q = \frac{4(-1)^q}{(1+2q)\pi}. \quad (4.50)$$

Combining equations (4.49), (4.50) with (4.42), we obtain

$$C(x, t) = 1 - \frac{4}{\pi} \sum_{q=0}^{\infty} \frac{(-1)^q}{1+2q} \cos\left(\frac{(2q+1)\pi x}{2}\right) \exp\left(-\frac{(1+2q)^2 \pi^2}{4} t\right). \quad (4.51)$$

Equation (4.38) is solved numerically using Method of Lines (MOL) approach. First, we discretize the space derivative appearing in the equation by employing the central finite difference formula. As a result equation (4.38) takes the following

form

$$\frac{dC_j}{dt} = \frac{C_{j+1} - 2C_j + C_{j-1}}{dx^2}, \quad j = 1, 2, 3, \dots, N, \quad (4.52)$$

where value of C_0 and C_{N+1} are obtained from the left (4.40) and the right (4.41) boundary conditions, respectively, and can be written as

$$C_0 = \frac{4u_2 - u_3}{3}, \quad C_{N+1} = 1, \quad (4.53)$$

and

$$C_j = C(x_j, t), \quad dx = \frac{1}{N}, \quad x_j = jdx.$$

The value of initial condition at each node can be calculated from the equation (4.39) as

$$C(x_j, 0) = 0. \quad (4.54)$$

Thus, we have a system of N ordinary differential equations (4.52) with N initial conditions given in equation (4.54), which is solved for any time t using MATLAB's solver *ode23*. Similarly, equation for solid displacement (4.30) is solved using Method of Lines. We discretize the space derivative and combine the solution given in relation (4.51), we get

$$\begin{aligned} \frac{du_j}{dt} = R \left[\exp \left(m \frac{u_{j+1} - u_{j-1}}{2dx} \right) \right]^{\frac{1}{n}} \times \\ \left[\frac{u_{j+1} - 2u_j + u_{j-1}}{dx^2} + 2Q \sum_{q=0}^{\infty} (-1)^q \sin \left(\frac{(2q+1)\pi x}{2} \right) \exp \left(\frac{-(1+2q)^2 \pi^2 t}{4} \right) \right]^{\frac{1}{n}}, \quad (4.55) \\ j = 1, 2, 3, \dots, N, \end{aligned}$$

where value of u_0 and u_{N+1} are obtained from the left (4.32) and the right (4.33) boundary conditions, respectively, and can be expressed as

$$u_0 = 0, \quad u_{N+1} = \frac{4u_N - u_{N-1} - 2dxQ}{3}, \quad (4.56)$$

and

$$u_j = u(x_j, t), \quad dx = \frac{1}{N}, \quad x_j = jdx.$$

The value of initial condition at each node can be calculated from the equation (4.31) as

$$u(x_j, 0) = 0. \quad (4.57)$$

Thus, we have a system of N ODEs (4.55) with N initial conditions given in relation (4.57), which is solved using efficient MATLAB's solver *ode23*. Similarly, we discretize the space derivative involved in governing equation of fluid pressure (4.37) as

$$P(x_j, t) = \frac{H_A}{p_0(\alpha + 1)} \left[\frac{u_{j+1} - u_{j-1}}{2dx} + Q \left(1 - \frac{4}{\pi} \sum_{q=0}^{\infty} \frac{(-1)^q}{1 + 2q} \cos \left(\frac{(2q + 1)\pi x_j}{2} \right) \exp \left(-\frac{(1 + 2q)^2 \pi^2}{4} t \right) \right) \right]. \quad (4.58)$$

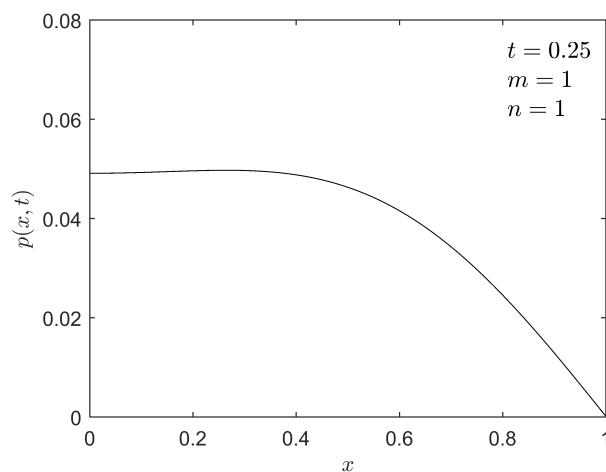


FIGURE 4.2: Interstitial Fluid Pressure $p(x, t)$ against distance x when power law index $n = 1.0$ at time $t = 0.25$.

The fluid pressure can be determined once the solid displacement is known. We recalled the solution of solid displacement $u(x, t)$ in the above equation and using the MATLAB command `plot(x,p(end,:),'-')` to get the solution for fluid pressure $p(x, t)$.

The values of different parameters for the biological tissues considered here are $\alpha = 0.3$, $Q = 0.03630$, $H_A = 4$, $R = 0.4$ and $p_o = 1$ [167]. It is worth mentioning here that by substituting the power-law index $n = 1$ in equation (4.37), the graph of fluid pressure $p(x, t)$ for the time $t = 0.25$ reported by Myers *et al.* [27], is recovered successfully as shown in Figure 4.2.

Below we will focus our attention to summarize the outcome of the above system.

4.6 Results and Discussion

This section represents the output of our numerical simulations for the solid displacement $u(x, t)$, ion-concentration $C(x, t)$, and interstitial fluid pressure $p(x, t)$ for cartilage. The effect of power-law index n on solid displacement and fluid pressure for the constant and non-linear permeability is illustrated graphically.

4.6.1 Ion Concentration Profile

Figure 4.3 represents ion-concentration in the articular cartilage as a function of distance x at various values of time $t = 0.1, 0.3, 1.0, 4$. At $t = 0.1, 0.3$, the curves show almost concave up behavior. Whereas at $t = 1.0$, curve shows linear behavior. Due to continuous supply of salt solution, ionic concentration in the cartilage increases with time and attains a maximum value at time $t = 4$. After which the salt bath does not affect the ionic concentration.

Figure 4.3 also compares the exact and MOL solution for the salt concentration $C(x, t)$ in the tissue. An excellent agreement can be noticed for different values of time.

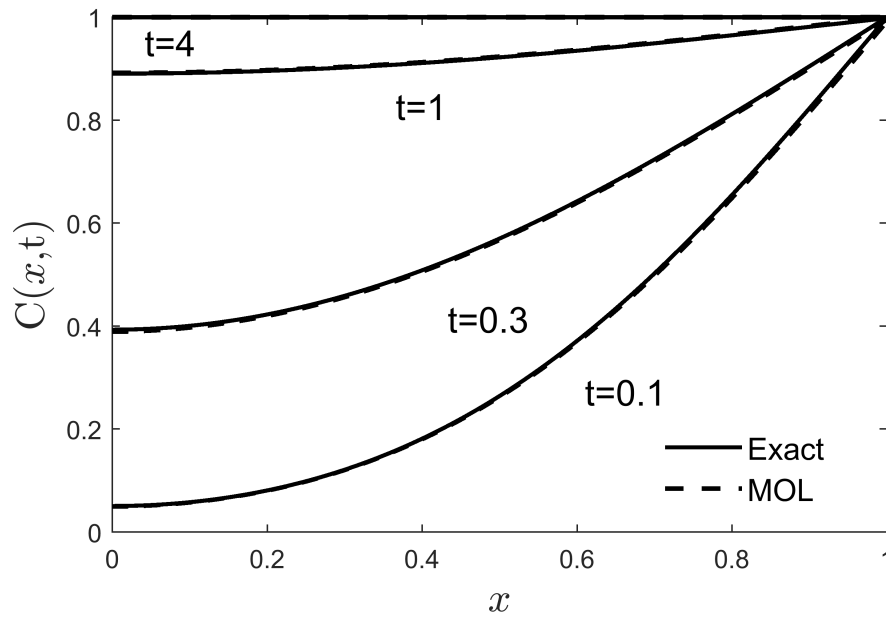


FIGURE 4.3: Theoretical prediction of the ion concentration as a function of distance x at time $t = 0.1, 0.3, 1.0, 4$. Exact (solid line) and numerical (dashed line) solution are plotted for ion-concentration to compare two solutions.

Figure 4.4 shows the effect of power-law index n on solid displacement for time $t = 0.1$ as a function of distance x . Moreover, three different values of the power-law index n are used along with strain dependent nonlinear permeability ($m \neq 0$). Solid displacement decreases for shear-thinning and Newtonian fluids from the center line of the cartilage. This observation is consistent with the earlier related study [119] for non-Newtonian fluid flow in porous tissue. Shear-thickening fluid ($n > 1$) induces more deformation as compared to Newtonian ($n = 1$) and shear-thinning ($0 < n < 1$) fluids. Therefore, our model predicts that salt influx causes cartilage contraction due to which fluid extrudes from tissue. Interestingly, exudation of shear-thinning fluid is more than shear-thickening fluid. This general observation is consistent with the fact that increases of salt concentration increases the strain rates, ultimately decreases the effective viscosity of shear-thinning fluid and increases the effective viscosity of shear-thickening fluid. The slope of the Newtonian fluid ($n = 1$) in a final state is found to be $-Q$, as predicted in earlier study [14] and slope of curve from $x = 0$ to $x = 0.4$ for shear-thinning fluid shows that there may be an expansion of the cartilage before final contraction.

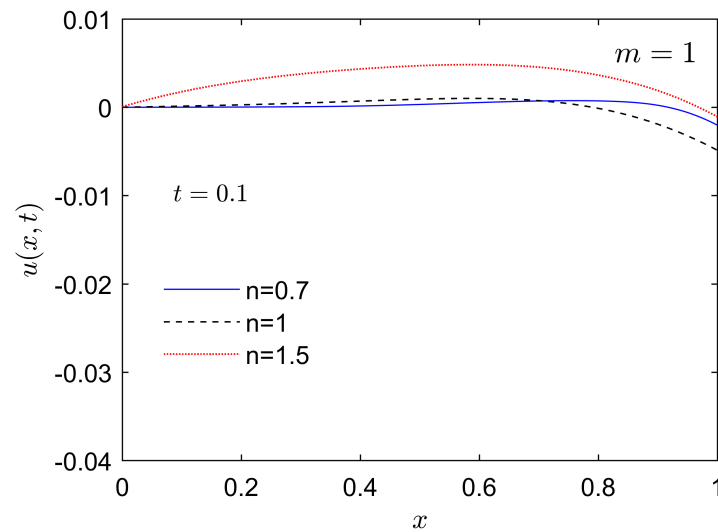


FIGURE 4.4: Solid displacement $u(x,t)$ against distance x for various power-law indices at time $t = 0.1$

Surprisingly, we have found from Figure 4.5 and Figure 4.6 that graphical illustration of solid displacement $u(x,t)$ shows almost the same results for constant ($m = 0$) and strain dependent nonlinear permeability ($m \neq 0$) for shear-thinning or shear-thickening fluid. Therefore, a comparison of different permeability parameters is not shown in the present work. It seems that salt concentration and power-law index n play a major role in the solid deformation. This is due to the fact that there is no external force other than the showering of salt-solution.

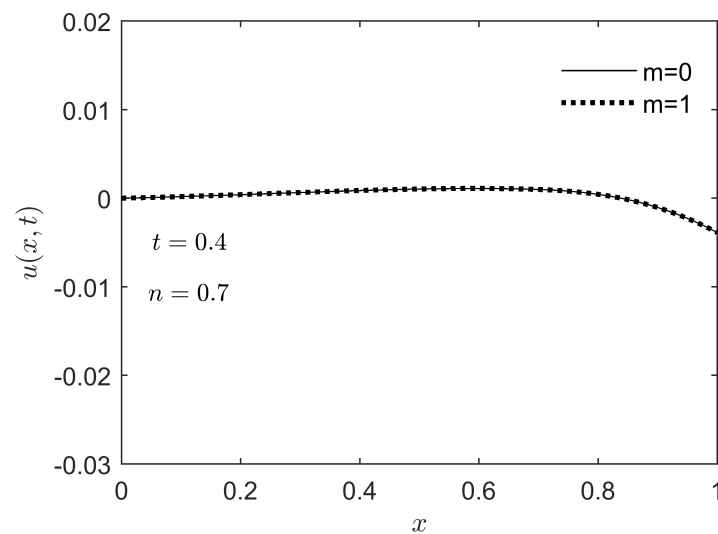


FIGURE 4.5: Solid displacement $u(x,t)$ against distance x for permeability parameters $m = 0, 1$ when power-law index $n = 0.7$ at time $t = 0.1$

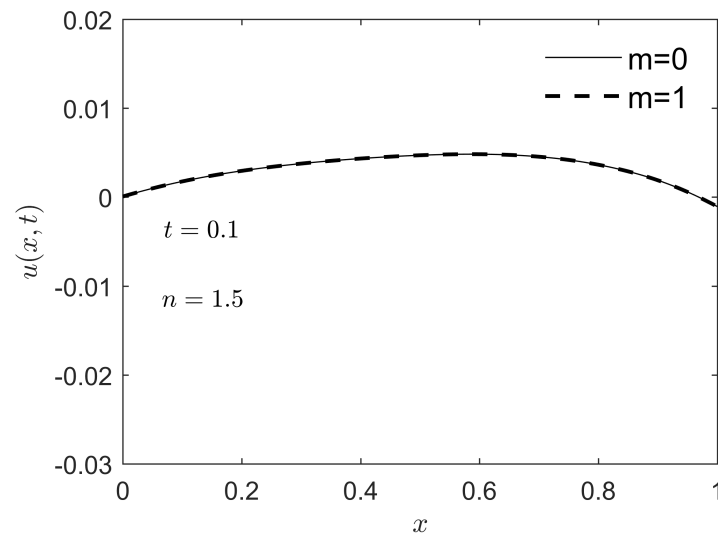


FIGURE 4.6: Solid displacement $u(x, t)$ against distance x for permeability parameters $m = 0, 1$ when power-law index $n = 1.5$ at time $t = 0.1$

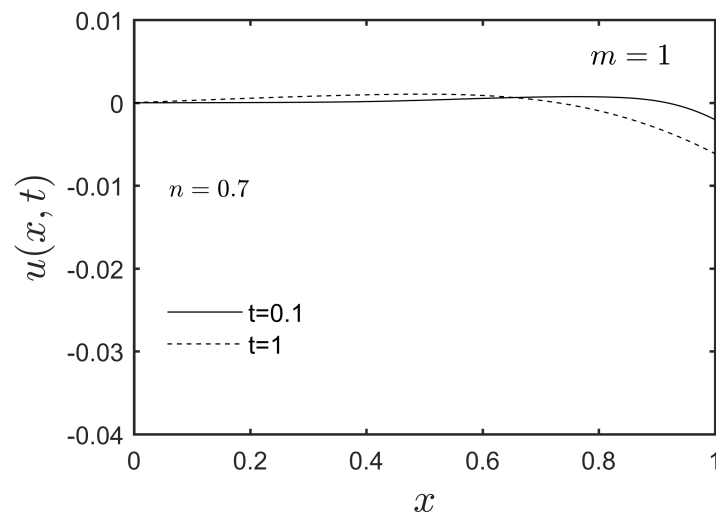


FIGURE 4.7: Solid displacement $u(x, t)$ against distance x when power law index $n = 0.7$ at times $t = 0.1, 1.0$.

Figure 4.7 and Figure 4.8 show the comparison of solid displacement profiles between shear-thinning ($0 < n < 1$) and shear-thickening ($n > 1$) fluids for non-linear permeability ($m = 1$) at various values of time $t = 0.1, 1.0$ as a function of distance x . Graphical illustration for shear-thinning fluid shows that solid deformation decreases as the time increases. But, reverse process can be observed for shear-thickening fluid. This observation is consistent with the recognition that salt

concentration of cartilage increases as the time increases and causes the cartilage to shrink and similar dynamics was observed in [27]. For the case of shear-thinning fluid, due to showering of salt solution, cells of cartilage lose fluid due to osmosis and cause shrinking of tissue. For the case of shear-thickening fluid, strain rate increases due to salt concentration and viscosity of fluid also increases. This prevents the flow of fluid through cartilage and causes expansion in the tissue.

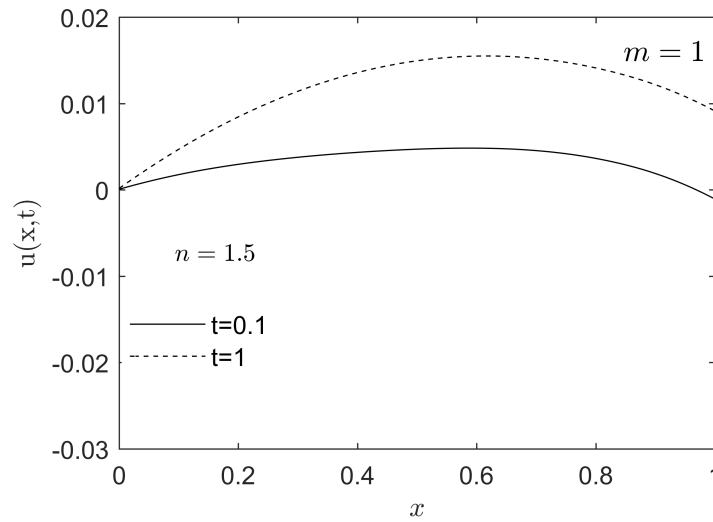


FIGURE 4.8: Solid displacement $u(x, t)$ against distance x when power law index $n = 1.5$. at times $t = 0.1, 1.0$.

Figure 4.9 and Figure 4.10 describe the effect of power-law index n on fluid pressure (as a function of distance x) at various times $t = 0.1, 1.2$ for shear-thinning and shear-thickening fluids. For shear-thinning and shear-thickening fluids, interstitial fluid pressure $p(x, t)$ vanishes slowly as ionic concentration attains its maximum value. Due to contraction of cartilage, discharge of shear-thinning fluid causes the decrease of interstitial fluid pressure with distance x . Myers *et al.* [27] presented the similar observation in the case of Newtonian fluid ($n = 1$). As shear-thickening fluid induces expansion in the cartilage, which causes a less increase in fluid pressure as compared to shear-thinning fluid. The subsequent depressurization in fluid pressure for shear-thinning and shear-thickening fluids is due to fluid exudation across the articular cartilage surface. Pressurization effects are more in shear-thinning fluid as compared to shear-thickening fluid as shear-thickening fluid extrudes faster than shear-thinning fluid which allows the cartilage to relax.

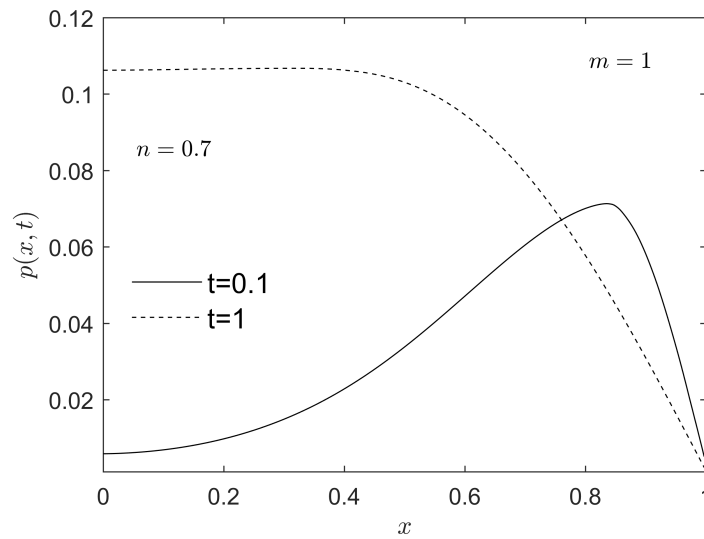


FIGURE 4.9: Interstitial Fluid Pressure $p(x, t)$ against distance x when power-law index $n = 0.7$ at times $t = 0.1, 1.0$.

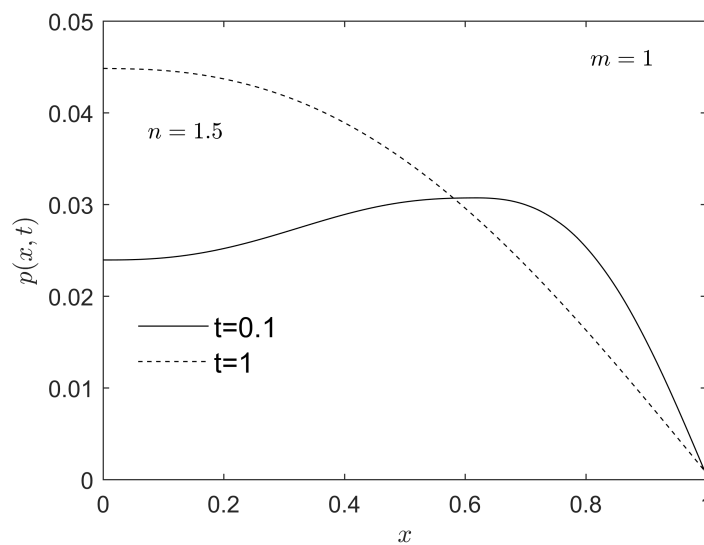


FIGURE 4.10: Interstitial Fluid Pressure $p(x, t)$ against distance x when power-law index $n = 1.5$ at times $t = 0.1, 1.0$.

4.7 Conclusion

In this chapter, we have analyzed the ion-induced deformation of soft biological tissue (articular cartilage). Our new contribution is a collection of numerical and analytical results that details the effects of power-law index (n) on deformation

of cartilage and fluid pressure. In particular, dimensions of a rectangular strip of cartilage was measured in a continuous supply of sodium chloride (NaCl) solution. Our results of ion-induced deformation are analogous to the classical results [14, 27] for ion-induced deformation of cartilage.

To model the problem, we used continuum theory of mixtures by considering the cartilage as a deformable porous material. Ion concentration term was incorporated in the solid stress equation to examine the results under a continuous sodium chloride (NaCl) shower. A parabolic PDE was considered which is uncoupled from the fluid pressure and solid displacement for the salt concentration in a cartilage. The summary of the results are as follows

- Graphical illustration shows that ionic concentration in the cartilage increases with time and attains a maximum value at time $t = 4$. After which the salt bath does not affect the ionic concentration.
- Graphical illustrations on Cartesian geometry show that solid displacement in articular cartilage decreased for the case of shear-thinning and Newtonian fluids.
- Solid displacement increased in articular cartilage for the case of shear-thickening fluid.
- Solid deformation of cartilage was significantly decreased for Newtonian fluid as compared to shear-thinning fluid.
- Shear-thickening fluid induces less fluid pressure as compared to shear thinning fluid.

Present work is an effort to incorporate mixture theory along with power modeling to understand the behavior of soft tissues like articular cartilage. The basic features of power-law fluid flow in a porous media like consistency index and power-law index may be of interest in a variety of different fields. The further questions that can be addressed are incorporation of additional features such as

evaporation, multidimensional fluid pressure, multidimensional solid deformation and more sophisticated interaction between solid, liquid and ionic concentration of NaCl. In this study, Non-Newtonian fluid models other than the power-law model can also be considered.

Chapter 5

Compressive Stress Relaxation Behavior of Articular Cartilage and its Effects on Fluid Pressure and Solid Displacement due to non-Newtonian Flow

5.1 Introduction

The aim of this chapter is to investigate the effects of the permeability parameter and power-law index on the deformation of the articular cartilage due to non-Newtonian fluid flow under stress-relaxation in compression. Ramp displacement is imposed on the surface of hydrated tissue. Fluid pressure and deformation of the cartilage is examined for the fast and slow rate of compression. A linear biphasic mixture theory has been employed to model the compressive stress-relaxation behavior of articular cartilage. The governing set of coupled equation in terms of fluid pressure and solid displacement are non-dimensionalized using suitable

normalized quantities. The solid displacement equation has been solved using numerical technique Method of Lines with *ode23t*. The effects of various parameters such as power-law index and permeability parameter on the pressure and displacement profile are illustrated graphically. Moreover, a graphical comparison of fast and slow rate of compression is also provided. In Section 5.2, a mathematical model is developed using biphasic mixture theory approach. Moreover, initial and boundary conditions are presented in Section 5.3. Non-dimensionalization is explained in Section 5.4 followed by solution methodology in Section 5.5. Section 5.6 is devoted to results and discussion. Concluding remarks are presented in the Section 5.7.

5.2 Mathematical Formulation

For the problem under discussion, a rectangular strip of articular cartilage mounted in a special device which is used in the displacement-controlled compression mode called Rheometric Mechanical spectrometer is considered. Cartilage dimensions are measured in non-Newtonian fluid and physiological Ringer's solution, interfaced with a $6 \times 10^{-5}m$ draining free rigid porous filter and maintained at constant temperature of $20^\circ C$ [92].

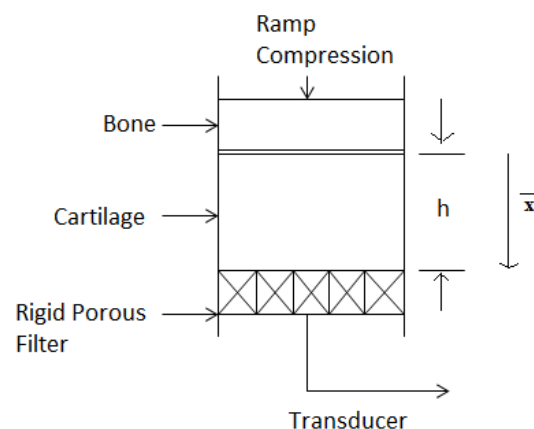


FIGURE 5.1: Illustration of a test related to confined compression stress-relaxation. During time $0 \leq \bar{t} \leq t_0$, a ramp compression is applied at the cartilage surface which is confined on the lateral surface, so that deformation occurs only in the \bar{x} direction.

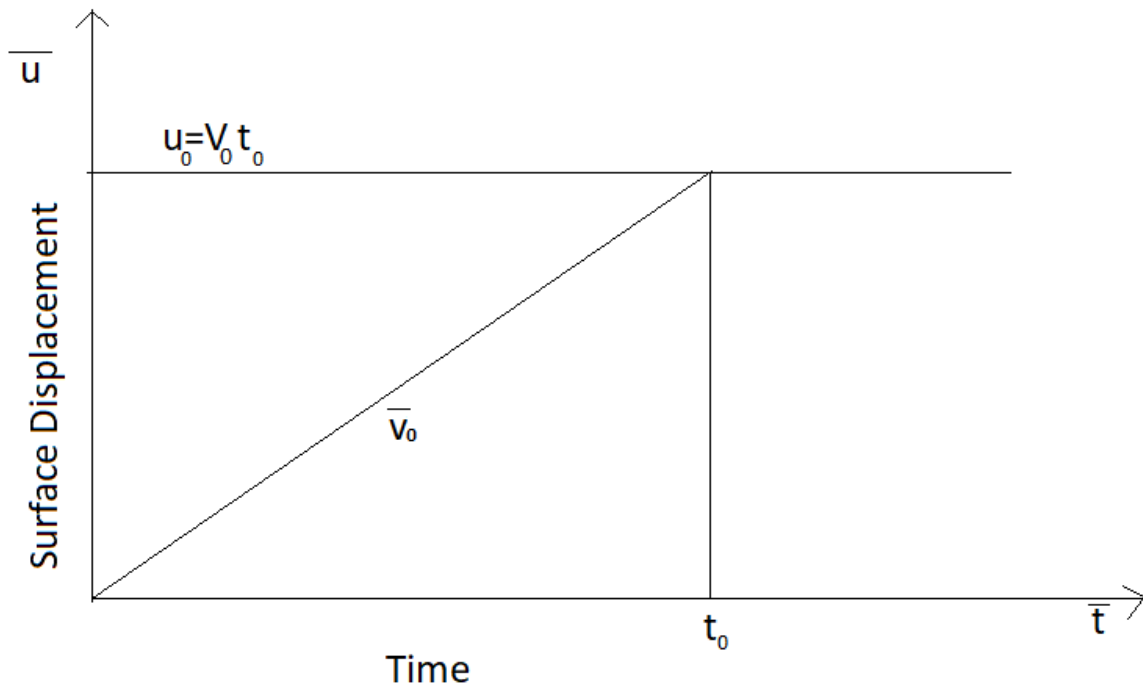


FIGURE 5.2: Graphical representation of a ramp displacement.

Lai *et al.* [96] have shown the measurements by experiments i.e., the average pore size of the articular cartilage decreases with compression make it difficult for the fluid to flow through tissue thereby permeability of the cartilage decreases. This is given by a mathematical equation of the form:

$$\bar{\kappa} = \kappa_0 \exp \left(m \frac{\partial \bar{u}}{\partial \bar{x}} \right), \quad (5.1)$$

where m and κ_0 are constants, value of m ranges from 1 to 20, $\kappa_0 = O(10^{-15})m^4 N^{-1} s^{-1}$, $\bar{u}(\bar{x}, \bar{t})$ represents the solid displacement, and $\frac{\partial \bar{u}}{\partial \bar{x}}$ is the dilation. Equation (5.1) shows that compression of solid matrix of tissue limits the rate of fluid flow in cartilage. Mow *et al.* [168] modeled the articular cartilage by considering it as a mixture composed of two phases: an interstitial fluid and porous solid matrix. This successful theory is based on the following assumptions: 1) each constituent of the cartilage is continuous and at each instant of time occupies each point in the space, 2) the two components of cartilage solid matrix and fluid are intrinsically incompressible, 3) the solid organic matrix is isotropic, homogeneous and linearly

elastic, 4) the viscosity of fluid component of cartilage is negligible for its contribution to the gravitational and osmotic forces except for its role to diffusional drag force, 5) the solid organic matrix of cartilage and coefficient of diffusive resistance are independent of deformation. Under the assumptions of infinitesimal strains, Mow *et al.* [92] presented the relationship between deformation of permeable, porous, intrinsically incompressible solid phase and the apparent stress on the solid matrix is

$$\mathbf{T}^s = -\alpha\bar{p}\mathbf{I} + 2\mu_s\mathbf{e} + \lambda_s e\mathbf{I} + 2\bar{\mu}_s\mathbf{D}^s + \bar{\lambda}_s\nabla \cdot (\mathbf{v}^s)\mathbf{I} - 2K_c\boldsymbol{\tau}, \quad (5.2)$$

and the linearized relationship between apparent stress on the interstitial fluid and flow field of incompressible fluid phase is

$$\mathbf{T}^f = -\bar{p}\mathbf{I} + 2\mu^f\mathbf{D}^f + \lambda^f\nabla \cdot (\mathbf{v}^f)\mathbf{I} + 2K_c\boldsymbol{\tau}. \quad (5.3)$$

Here, \mathbf{D}^s and \mathbf{e} are rate of deformation tensor and infinitesimal strain, respectively; α is the ratio from solid volume fraction to fluid volume fraction; \bar{p} is the fluid pressure; \mathbf{D}^f and \mathbf{v}^f is the rate of deformation tensor and fluid velocity respectively; dynamic and bulk viscosities of the interstitial fluid can be represented by μ^f and λ^f respectively; $\boldsymbol{\tau}$ is the spin tensor of the organic solid material relative to the interstitial fluid phase; viscoelastic and isotropic moduli of the solid phase can be represented by $\bar{\mu}_s$, $\bar{\lambda}_s$ and μ_s , λ_s , respectively; $e = \text{trace}(\mathbf{e})$, a diffusive couple interaction between interstitial fluid phase and solid organic matrix is represented by constant K_c .

The conservation of mass for the mixture of fluid and solid phases is written as [165]

$$\nabla \cdot \mathbf{v}^f + \alpha\nabla \cdot \mathbf{v}^s = 0. \quad (5.4)$$

where α is the ratio from solid volume fraction to fluid volume fraction. The momentum balance for the fluid phase and solid phase yields the following equation

of motion

$$\rho^\beta \left(\frac{\partial \mathbf{v}^\beta}{\partial t} + (\mathbf{v}^\beta \cdot \nabla) \mathbf{v}^\beta \right) = \nabla \cdot \mathbf{T}^\beta + \rho^\beta \mathbf{b}^\beta + \boldsymbol{\pi}^\beta, \quad (5.5)$$

where $(\beta = s, f)$ denotes solid phase and fluid phase, respectively. Here, ρ^β is the density, \mathbf{v}^β the velocity, \mathbf{T}^β the stress tensor, \mathbf{b}^β the net body force and $\boldsymbol{\pi}^\beta$ is the drag force for each phase. The body forces are neglected due to negligible mass of cartilage. For a particular choice of time scale, Barry and Aldis [165] have neglected the inertial terms appearing in equation (5.5) but we have neglected these terms due to small deformations and velocities of both phases that reduces the momentum balance to the following form

$$\nabla \cdot \mathbf{T}^\beta + \boldsymbol{\pi}^\beta = 0, \quad (5.6)$$

due to internal frictional forces, Newton's third law of motion implies that $\boldsymbol{\pi}^s + \boldsymbol{\pi}^f = 0$. The drag force due to local interaction between fluid phase and solid phase is written as [9]

$$\boldsymbol{\pi}^s = -\boldsymbol{\pi}^f = K |\mathbf{v}^f - \mathbf{v}^s|^{n-1} (\mathbf{v}^f - \mathbf{v}^s) + \dot{\mathbf{b}} \nabla e. \quad (5.7)$$

Here, capillary force within the cartilage is represented by $\dot{\mathbf{b}}$, diffusive drag coefficient is represented by K . The permeability $\bar{\kappa}$ is related to drag coefficient K by the expression [96]

$$\bar{\kappa} = \frac{1}{(1 + \alpha)^{n+1} K}. \quad (5.8)$$

It is worth mentioning that permeability $\bar{\kappa}$ for Newtonian case can be recovered when we set power law index n equals to unity in the above equation. It is important to note that permeability $\bar{\kappa}$ can also defined by the relationship given by equation (5.1). To use equations (5.1)-(5.8), the infinitesimal theory and power-law index effects described by a solid-fluid mixture, we need eleven parameters ($n, K, \dot{\mathbf{b}}, \alpha, \lambda_s, \bar{\lambda}_s, \mu^f, \mu_s, \bar{\mu}_s, K_c, \lambda^f$). It is very difficult to assess all these parameters to analyze the solid-fluid mixture. Therefore, Mow et al. [168] presented a biphasic

model for soft tissue by assuming: 1) Solid phase of cartilage is linearly elastic so, $\bar{\mu}^s = \bar{\lambda}^s = 0$; 2) the capillary force within the cartilage is negligible so $\dot{b} = 0$; 3) diffusive interaction within the constituents of mixture is considered to be negligible so $K_c = 0$; 4) $\alpha = \phi^s / \phi^l = \text{constant}$; $\mu^f = \lambda^f = 0$.

The stress-relaxation and creep phenomena are described by non-linear equations in power law index n governing the fluid pressure and solid displacement, and these processes are due to stress relaxation (fluid distribution) and creep (fluid exudation) within the cartilage. In this chapter, we will extend the work by Holmes *et al.* "analysis of non-linear, flow dependent compressive stress relaxation of soft tissue" to "flow of power-law fluid through cartilage." by considering the constant ($m = 0$) and non-linear strain dependent ($m \neq 0$) permeability. The deformation within the cartilage is given in one-dimensional form by $v^s = (v^s, 0, 0)$ and $v^f = (v^f, 0, 0)$. The surface of the cartilage specimen from $\bar{x} = 0$ to $\bar{x} = h$ defines the depth of cartilage. Now integrating equation (5.4) w.r.t \bar{x} , we get

$$v^f = -\alpha v^s, \quad (5.9)$$

where constant of integration is zero, as the boundary at $\bar{x} = h$ is assumed to be impermeable and rigid (these conditions are true for adult joints only). After combining equations (5.2), (5.3), (5.6) and (5.7) with above assumptions may be written as

$$-\alpha \frac{\partial \bar{p}}{\partial \bar{x}} + H_A \frac{\partial^2 \bar{u}}{\partial \bar{x}^2} = -K |v^f - v^s|^{n-1} (v^f - v^s), \quad (5.10)$$

and

$$\frac{\partial \bar{p}}{\partial \bar{x}} = -K |v^f - v^s|^{n-1} (v^f - v^s), \quad (5.11)$$

where

$$H_A = 2\mu_s + \lambda_s,$$

and \bar{u} is the \bar{x} component of the cartilage displacement vector. Equations (5.9) and (5.10) may be simplified to eliminate v^f

$$-\alpha \frac{\partial \bar{p}}{\partial \bar{x}} + H_A \frac{\partial^2 \bar{u}}{\partial \bar{x}^2} = K(\alpha v^s + v^s)^n. \quad (5.12)$$

Similarly, combination of (5.9) and (5.11) gives

$$\frac{\partial \bar{p}}{\partial \bar{x}} = K(\alpha v^s + v^s)^n, \quad (5.13)$$

Equations (5.12) and (5.13) may now be combined to eliminate $\partial \bar{p} / \partial \bar{x}$

$$H_A \frac{\partial^2 \bar{u}}{\partial \bar{x}^2} = (\alpha + 1)^{n+1} K (v^s)^n. \quad (5.14)$$

Substituting relations (5.1), (5.8) and $v^s = \frac{\partial \bar{u}}{\partial \bar{t}}$ in above equation yields the following governing equation for solid displacement \bar{u}

$$\left(\frac{\partial \bar{u}}{\partial \bar{t}} \right) = \left(\kappa_o \exp \left(m \frac{\partial \bar{u}}{\partial \bar{x}} \right) H_A \frac{\partial^2 \bar{u}}{\partial \bar{x}^2} \right)^{\frac{1}{n}}. \quad (5.15)$$

Again (5.12) and (5.13) may be simplified to yield

$$\frac{\partial \bar{p}}{\partial \bar{x}} = \frac{H_A}{(\alpha + 1)} \frac{\partial^2 \bar{u}}{\partial \bar{x}^2}. \quad (5.16)$$

On integrating the equation (5.16) and using boundary condition $\bar{p}(h, \bar{t}) = 0$, we get the governing equation in fluid pressure as

$$\bar{p}(\bar{x}, \bar{t}) = \frac{H_A}{(\alpha + 1)} \left[\frac{\partial \bar{u}(\bar{x}, \bar{t})}{\partial \bar{x}} - \frac{\partial \bar{u}(h, \bar{t})}{\partial \bar{x}} \right]. \quad (5.17)$$

5.3 Initial and Boundary Conditions

In this section, for the stress-relaxation behavior of articular cartilage, we outline the initial and boundary conditions needed to solve governing equations given in previous section.

We consider the same initial and boundary conditions as in [92]:

$$\bar{u}(\bar{x}, 0) = 0, \quad (5.18)$$

$$\bar{u}(h, \bar{t}) = 0, \quad (5.19)$$

and

$$\bar{u}(0, \bar{t}) = \begin{cases} V_0 \bar{t} & \text{for } 0 \leq \bar{t} \leq t_0 \quad (\text{compression stage}) \\ V_0 t_0 & \text{for } t_0 \leq \bar{t}. \quad (\text{relaxation stage}) \end{cases} \quad (5.20)$$

Note that the solid displacement condition given by (5.20) for stress-relaxation studies is defined by ramp function. As it turns out, the fractional drag due to exudation of non-Newtonian fluid is greater than measured stress at the cartilage surface in accordance with equations (5.9) and (5.20). Hence, the magnitude of $\frac{\partial \bar{u}}{\partial \bar{x}}$ is controlled by the rate of compression V_0 such that the theory of infinitesimal strain remains valid. Precise and controlled experimental value of rate of compression is $4 \times 10^{-8} \text{ms}^{-1}$ [92].

5.4 Non-Dimensionalization

To analyze the nonlinear governing equations for solid displacement (5.15) and fluid pressure (5.17), it is first necessary to non-dimesnionalize the problem, which we do by considering

$$\bar{x} = hx, \quad (5.21)$$

$$\bar{t} = t_0 t, \quad (5.22)$$

$$\bar{u} = u_0 u(x, t), \quad (5.23)$$

$$\bar{u} = V_0 t_0 u(x, t), \quad (5.24)$$

$$\bar{p}(\bar{x}, \bar{t}) = p(x, t) p_0, \quad (5.25)$$

where $p_0=1$ pascal.

On substituting above parameters in equation (5.15), we get

$$\left(\frac{\partial u(x, t)}{\partial t} \right) = (\epsilon)^{1/n} \delta \left(R^2 \exp \left(\epsilon m \frac{\partial u}{\partial x} \right) \frac{\partial^2 u(x, t)}{\partial x^2} \right)^{\frac{1}{n}}, \quad (5.26)$$

where

$$\epsilon = \frac{V_0 t_0}{h}, \quad (5.27)$$

$$\delta = \left(\frac{h u_0^{-n}}{t_0^{1-n}} \right)^{1/n}, \quad (5.28)$$

$$R^2 = \frac{H_A \kappa_0 t_0}{h^2}. \quad (5.29)$$

Different parameters involving in above equation (5.26) may differ in value among

biological tissues [99]. Equation (5.26) is required parabolic and non-linear governing equation in terms of solid displacement u as a function of non-dimensional space variable x and time t . Choosing the parameter $\delta = 20$ in equation (5.26), a natural length scale h for the present problem can be written as

$$h = 20^n v_0^n t_0. \quad (5.30)$$

It is worth mentioning that using simple dimensional analysis, right side of equation (5.30) can be shown to have the dimensions of product of power-law velocity and time. Moreover, stress relaxation behavior of cartilage for Newtonian fluid case [92] can be recovered by setting power-law index n equals to one in equation (5.26).

Solid displacement is subject to following initial and boundary conditions in one dimensional form

$$u(x, 0) = 0, u(1, t) = 0, \quad (5.31)$$

$$u(0, t) = \begin{cases} t & \text{for } 0 \leq t \leq 1 \\ 1 & \text{for } 1 \leq t. \end{cases} \quad (5.32)$$

The dimensionless interstitial fluid pressure can be written as

$$p(x, t) = \frac{H_A \epsilon}{(1 + \alpha) p_o} \left(\frac{\partial u(x, t)}{\partial x} - \frac{\partial u(1, t)}{\partial x} \right). \quad (5.33)$$

Compression is considered as fast rate of compression, if the time of compression is less than 1000s and value of R is less than 1. Similarly, compression is considered as slow rate of compression, if time of compression is more than 1000s and value of R is greater than 1.

5.5 Solution Procedure

The resulting governing equations for the solid displacement (5.26) and the fluid pressure (5.33) along with initial and boundary conditions are nonlinear and analytical solutions are difficult to obtain. Non-linearity is sought out by applying the numerical technique Method of Lines (MOL). The main idea of this technique is to discretize the space variable and leaving the time variable continuous. Thus, we discretize the space derivative given in relation (5.26), we get

$$\frac{du_j}{dt} = (\epsilon)^{1/n} \delta \left[R^2 \exp \left(\epsilon m \frac{u_{j+1} - u_{j-1}}{2dx} \right) \frac{u_{j+1} - 2u_j + u_{j-1}}{dx^2} \right]^{1/n}, \quad (5.34)$$

$$j = 1, 2, 3, \dots, N,$$

where value of u_0 and u_{N+1} are obtained from the left and right boundaries respectively, and

$$u_j = u(x_j, t), \quad dx = \frac{1}{N}, \quad x_j = jdx.$$

The value of initial condition at each node can be calculated from the equation (5.31) as

$$u(x_j, 0) = 0. \quad (5.35)$$

Thus, we have a system of N ordinary differential equations (5.34) with N initial conditions given in relation (5.35), which is solved for any time t using MATLAB's solver *ode23t*. Similarly, governing equation for fluid pressure (5.33) can be written

as

$$p(x, t) = \frac{H_A \epsilon}{(1 + \alpha) p_o} \left(\frac{u_{j+1} - u_{j-1}}{2dx} - \frac{u_{j-1} - 4u_j + 3u_{j+1}}{2dx} \right). \quad (5.36)$$

Using the command `plot(x,p(end,:), '')`, after recalling the solution of solid displacement $u(x, t)$ in above equation, gives solution for fluid pressure.

The average value of k_o , H_A and h for normal bovine cartilage are $k_o = 4 \times 10^{-15} m^4/N.s$, $H_A = 5.5 \times 10^5 Nm^{-2}$, $\alpha = 0.3$, $\epsilon = 0.05$ and $h = 1.5 \times 10^{-3} m$ [169]. It is worth mentioning here that by substituting the power-law index $n = 1$ in equation (5.26), the graph of solid displacement $u(x, t)$ for the time $t = 0.5$ reported by Holmes *et al.* [92], is recovered successfully as shown in Figure 5.3.

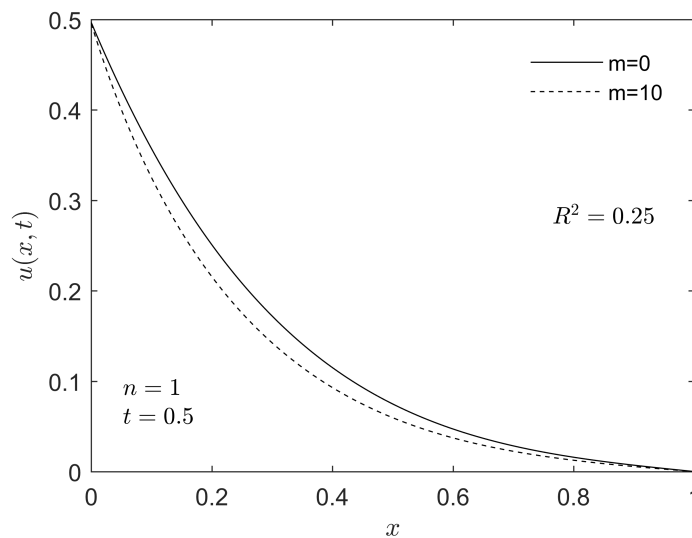


FIGURE 5.3: Solid displacement $u(x, t)$ against distance x when power-law index $n = 1.0$ at time $t = 0.5$.

5.6 Results and Discussion

This section presents the output of our numerical simulations for the solid displacement $u(x, t)$ and interstitial fluid pressure $p(x, t)$ for cartilage. The effects of power law index n , constant permeability $m = 0$ and non-linear permeability $m \neq 0$ on solid displacement and fluid pressure are illustrated graphically.

Figure 5.4 and Figure 5.5 represent the dimensionless solid displacement for shear-thinning ($0 < n < 1$), Newtonian ($n = 1$) and shear-thickening ($n > 1$) fluids during the fast ($R^2 = 0.25$) and slow rate ($R^2 = 4$) of compression for linear permeability ($m = 0$) at $t = 1$. Both cases show that solid displacement increases with the rise in power-law index n . A similar profile was observed by Holmes *et al.* [92] for a Newtonian case with a difference of shear-thickening and shear-thinning fluid which is an important point of this study. During the fast rate of compression, solid displacement for shear-thinning fluid will fall faster than a shear-thickening fluid. This general observation is consistent with the recognition that during the fast rate of compression, strain rates are the largest and, hence, the effective viscosity of the shear-thinning viscosity decreases while that for the shear-thickening fluid will increase. Eventually, shear-thinning fluid exudes faster than Newtonian and shear-thickening fluid. During the slow rate of compression, the strain rate increases, but at a slow rate. So shear-thinning fluid exudes from cartilage at a slow rate. Moreover, these results are consistent with the previous experimental [170] and numerical [131, 171] studies on the compression of the articular cartilage.

Figure 5.6 and Figure 5.7 show solid displacement $u(x, t)$ as a function of distance x for different values of permeability parameter $m = 0, 5, 10$ for shear-thinning and shear-thickening fluids for the fast rate of compression ($R^2 = 0.25$) at $t = 1$, respectively. Generally, the value of permeability parameter m for biological tissues ranges from 1 to 10 [99, 119].

It is important to note that the effect of linear permeability $m = 0$ as well as non-linear permeability $m \neq 0$ on solid displacement is more profound in the case of shear-thickening fluid as compared to the shear-thinning fluid. It is clear from Figure 5.6 that solid displacement falls uniformly with the increase in permeability parameter for shear-thinning fluid. Moreover, solid displacement shows negligible inflection even for large permeability parameter m for shear-thickening fluid. Constant permeability $m = 0$ induces greater solid deformation as compared to non-linear permeability $m \neq 0$.

This suggests that the cartilage will experience a contraction with an increase in the permeability parameter and this result is consistent with the previous study [92]. This is due to fact that high permeability parameter, allows more fluid to flow out of the cartilage. Due to this reason, contraction of cartilage occurred and ultimately solid displacement decreases.

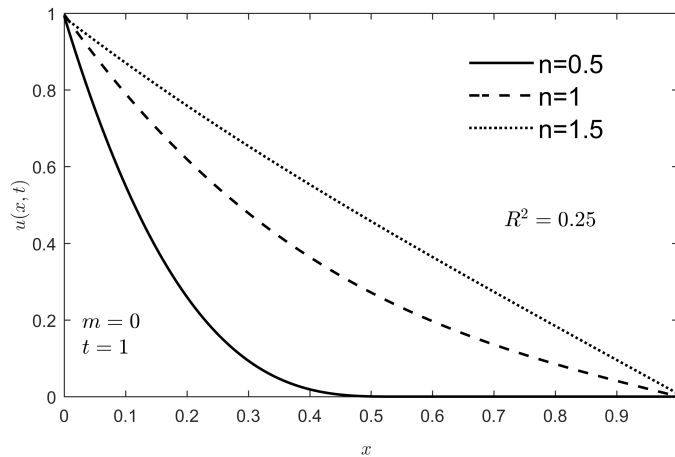


FIGURE 5.4: Dimensionless Solid displacement $u(x, t)$ profile vs distance x for power law index $n = 0.5$, $n = 1$ and $n = 1.5$ during the fast rate of compression for linear permeability ($m = 0$) at time $t = 1$.

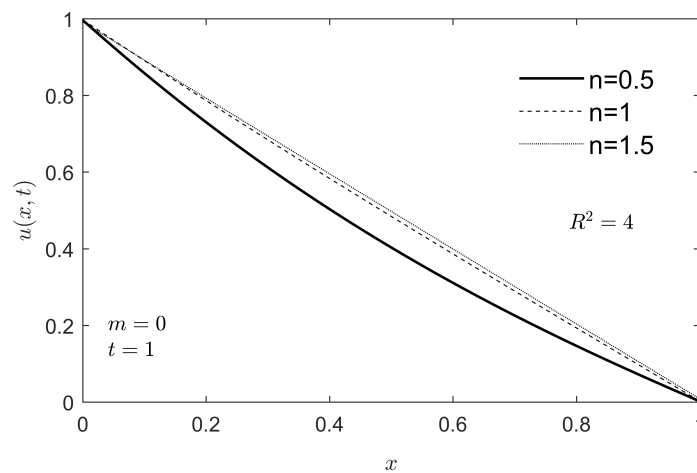


FIGURE 5.5: Dimensionless Solid displacement $u(x, t)$ profile vs distance x for power law index $n = 0.5$, $n = 1$ and $n = 1.5$ during the slow rate of compression for linear permeability ($m = 0$) at time $t = 1$.

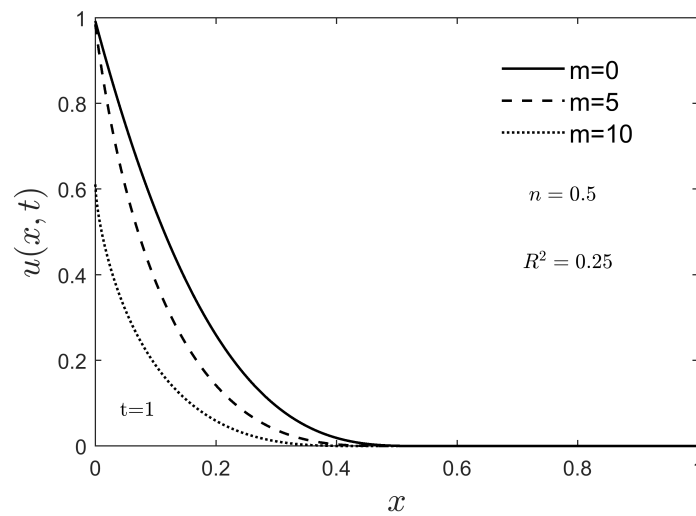


FIGURE 5.6: Solid displacement vs distance for various permeability parameters when $n = 0.5$ during fast rate of compression ($R^2 = 0.25$)

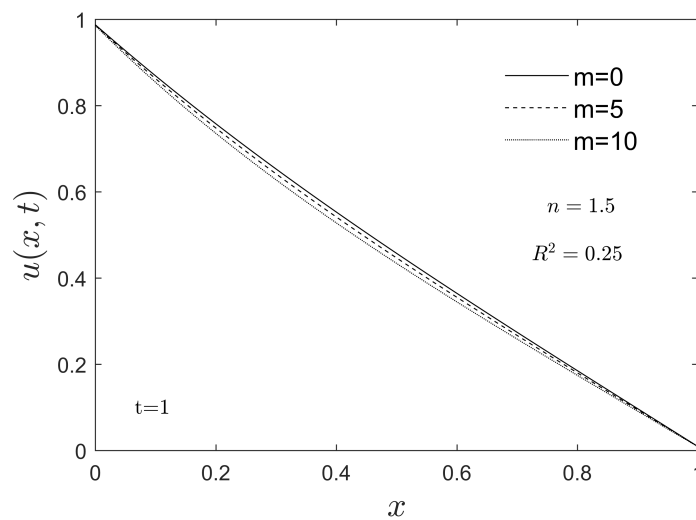


FIGURE 5.7: Solid displacement vs distance for various permeability parameters when $n = 1.5$ during fast rate of compression ($R^2 = 0.25$).

Figure 5.8 and Figure 5.9 show profile of fluid pressure $p(x, t)$ as a function of distance x for linear permeability $m = 0$ at $t = 0.01$ for shear-thinning, Newtonian and shear-thickening during fast ($R^2 = 0.5$) and slow rate of compression ($R^2 = 1.1$), respectively. Fluid pressure decreases with an increase in power-law index n . But pressure effects are more profound in the fast rate of compression as compared to the slow rate of compression. Fluid pressure increases linearly for both cases of shear-thinning fluid ($0 < n < 1$), but for the fast rate of compression

fluid pressure increases significantly. This is due to the fact that the viscosity of shear-thinning fluid decreases under shear stress. It is important to note that for all cases of power-law indexes $n = 0.5, 1, 1.2$, behavior show at $x = 0$ is totally opposite of profile of fluid pressure at $x = 1$. Moreover, high fluid pressure causes more exudation of fluid, due to which fluid pressure for shear-thinning fluid drops significantly as compared to Newtonian and shear-thickening fluid. This result is consistent with previous studies of the interstitial flow field in the tissue [172].

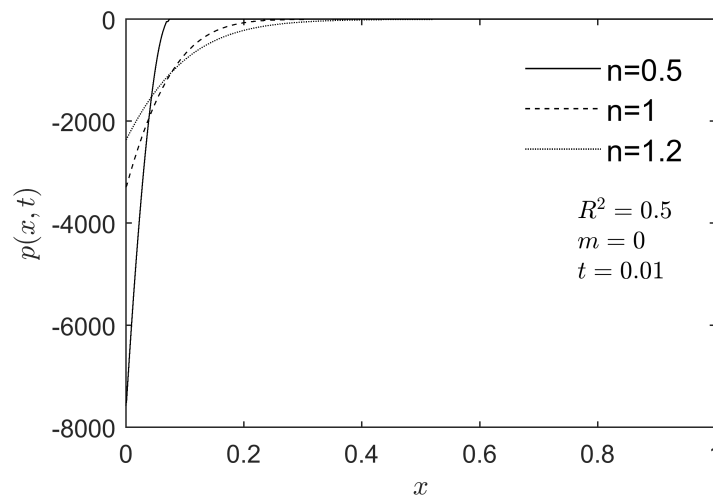


FIGURE 5.8: Dimensionless Fluid Pressure $p(x, t)$ profile vs distance x for power law index $n = 0.5, n = 1$ and $n = 1.2$ during the fast rate of compression ($R^2 = 0.5$) for linear permeability ($m = 0$) at time $t = 0.01$.

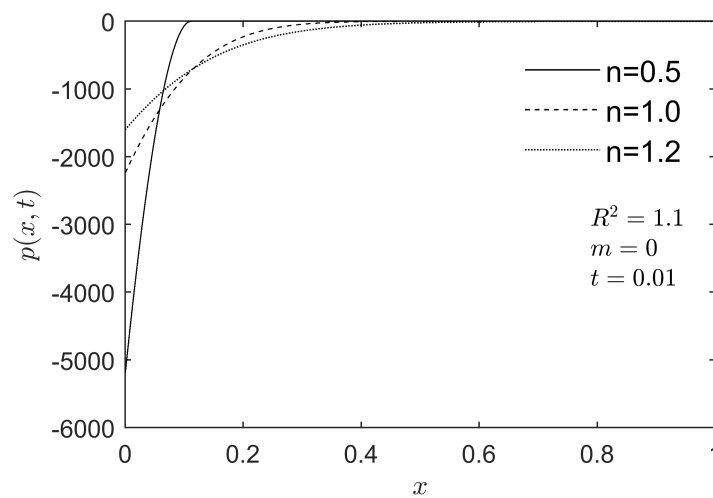


FIGURE 5.9: Dimensionless Fluid pressure $p(x, t)$ profile vs distance x for power law index $n = 0.5, n = 1$ and $n = 1.2$ during the slow rate of compression ($R^2 = 1.1$) for linear permeability ($m = 0$) at time $t = 0.01$.

Figure 5.10, Figure 5.11, Figure 5.12 and Figure 5.13 show the solid deformation and fluid pressure of shear-thinning ($0 < n < 1$) and shear-thickening fluids ($n > 1$) for linear permeability $m = 0$ at $t = 0.1, 0.4$ during fast rate of compression, respectively.

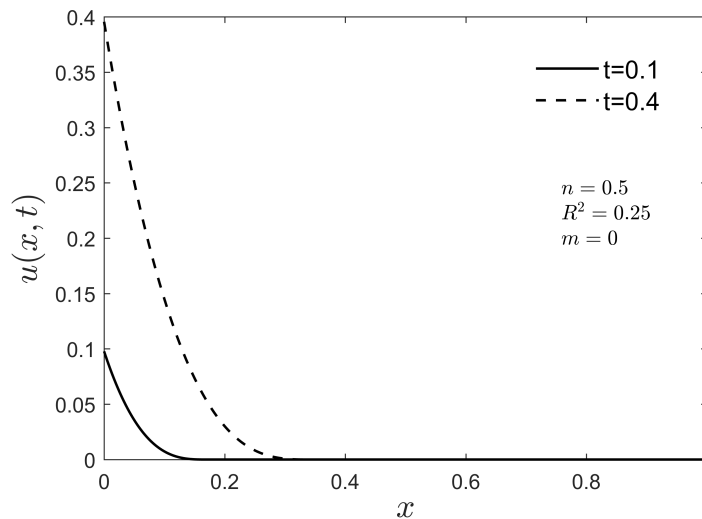


FIGURE 5.10: Solid displacement versus distance for power law index $n = 0.5$ for linear permeability ($m = 0$) at $t = 0.1, 0.4$ during fast rate of compression.

Solid deformation increases with an increase in time from $t = 0.1$ to $t = 0.4$ for shear-thinning and shear-thickening fluids, but profound effects are found in deformation for shear-thickening fluid at $t = 0.4$, as in shear-thickening fluid viscosity increases with increase in strain rate.

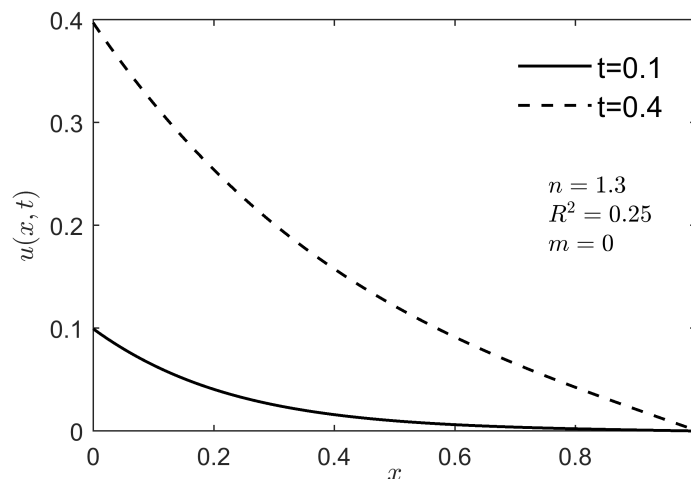


FIGURE 5.11: Solid displacement versus distance for power law index $n = 1.3$ for linear permeability ($m = 0$) at $t = 0.1, 0.4$ during fast rate of compression.

Results show that shear-thinning fluid induces more fluid pressure as compared to the shear-thickening but drops before $x = 1$. It can be seen that shear-thickening fluid resists the change and possesses more inertia than shear-thinning fluid. Fluid pressure increases with increase in time from $t = 0.1$ to $t = 0.4$ and this result is consistent with the previous study [131].

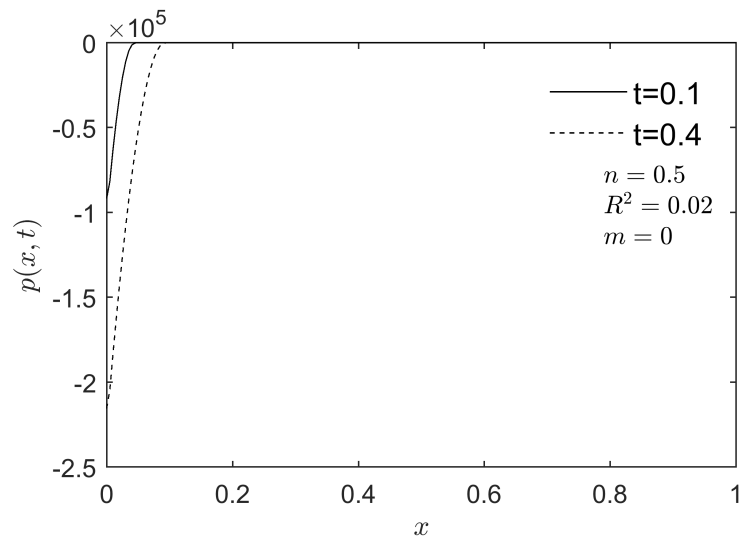


FIGURE 5.12: Fluid Pressure versus distance for power law index $n = 0.5$ for linear permeability ($m = 0$) at $t = 0.1, 0.4$ during fast rate of compression.

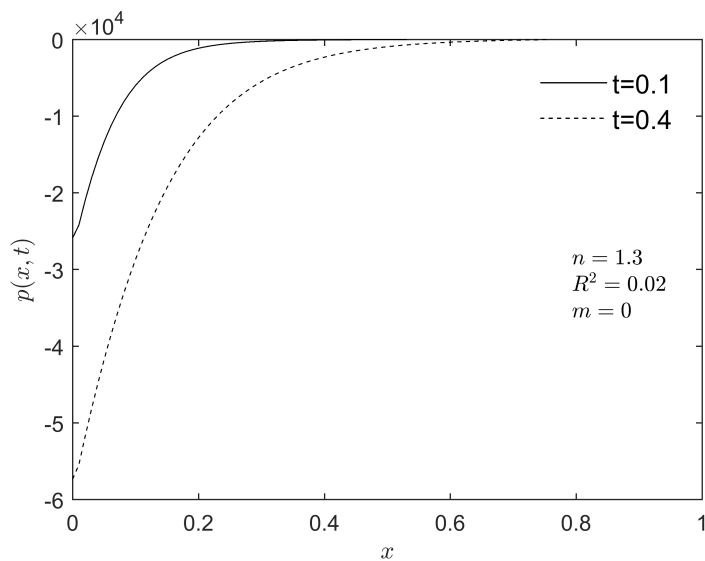


FIGURE 5.13: Fluid Pressure versus distance for power-law index $n = 1.3$ for linear permeability ($m = 0$) at $t = 0.1, 0.4$ during fast rate of compression.

5.7 Concluding Remarks

In this chapter, we have investigated the non-Newtonian flow-dependent compressive stress relaxation behavior of soft biological tissue (articular cartilage). In particular, a flow of non-Newtonian fluid through rectangular specimen of articular cartilage is considered. A ramp-displacement is imposed on the surface of hydrated, soft tissue. Fluid pressure and solid deformation are examined during the slow and fast rate of compression.

We have used biphasic mixture theory to develop a mathematical model for a mixture of cartilage and non-Newtonian fluid. This modeling approach was previously used by Siddique and Anderson (2011). The summary of the results are as follows

- The solid deformation increases with an increase in power-law index n .
- Shear-thickening fluid ($n > 1$) induces more deformation as compared to the shear-thinning fluid ($0 < n < 1$) and the Newtonian fluid ($n = 1$) during the fast and slow rate of compression.
- Numerical results also show that linear permeability ($m = 0$) induces more deformation as compared to the strain-dependent nonlinear permeability ($m \neq 0$) for shear-thinning and shear-thickening fluids.
- Solid displacement as a function of distance increases with an increase in time for shear-thinning and shear-thickening fluids. But more profound effects of change in time for solid displacement can be found in shear-thickening fluid as compared to the shear-thinning fluid.
- Numerical results show that shear-thinning fluid induces more fluid pressure as compared to Newtonian and shear-thickening fluids during the fast and slow rate of compression. .

We have explored the compressive stress-relaxation behavior of cartilage due to non-Newtonian flow. Numerical results suggest that the findings of the numerical study can be further improved both experimentally and theoretically. An

accurate and realistic mathematical model can be developed by adding additional features such as chemical interaction between non-Newtonian fluid and cartilage, evaporation, different permeability relations, and different geometries. A direct comparison of experimental work with our divine theoretical model will assist in answering many critical questions.

Chapter 6

Flow-Dependent Compressive Stress-Relaxation Behavior of Articular Cartilage with MHD Effects

6.1 Introduction

Based on the geometry of the previous problem, a mathematical model has been developed for the deformation of the solid phase of the cartilage due to the flow of the electrically conducting fluid from it. The model is based on the biphasic mixture theory which incorporates the nonlinear strain-dependent permeability found earlier from various experiments. In this investigation, solid and fluid phases were assumed to be non-dissipative and also intrinsically incompressible. The system of coupled partial differential equations was developed for the fluid pressure and solid deformation for the slow and fast rate of compression in the presence of the Lorentz forces. The resulting system is solved numerically using Method of Lines (MOL) and graphs are produced to highlight the effects of the magnetic parameter

on fluid pressure and solid displacement. In Section 6.2, the mathematical modeling of the problem using continuum mixture theory approach is introduced. The solution procedure is presented in Section 6.3. Section 6.4 is devoted to the solution methodology. Results and discussions are presented in Section 6.5 followed by the concluding remarks in Section 6.6.

6.2 Mathematical Formulation

We study the problem of flow dependent compressive stress-relaxation behavior of articular cartilage with MHD effects as shown in the Figure 6.1. The specimen of the soft tissue is mounted in Rheometric Mechanical spectrometer used for the displacement controlled compression mode. Physiological Ringer's solution is used to bath specimen, maintained at 20^0 C and interfaced with a 60μ m free draining rigid porous filter. The cartilage is compressed on the lateral surface such that deformation occurs in the \bar{x} direction only. During time $0 \leq \bar{t} \leq t_0$, a ramp displacement is applied at the specimen tissue surface.

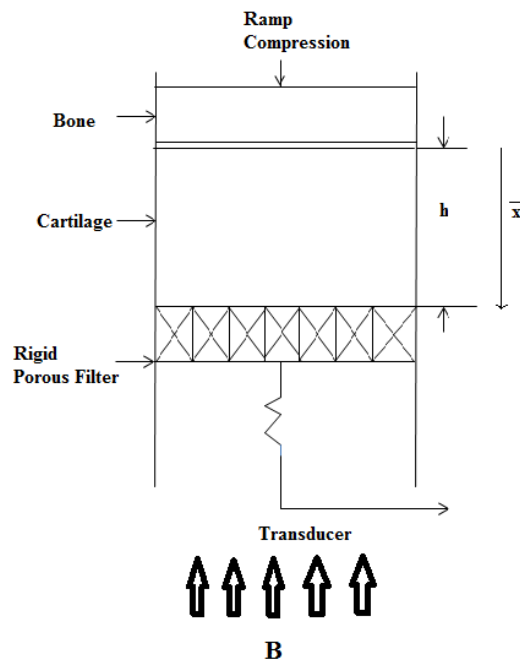


FIGURE 6.1: Schematic representation of one-dimensional confined compression used for the stress-relaxation test.

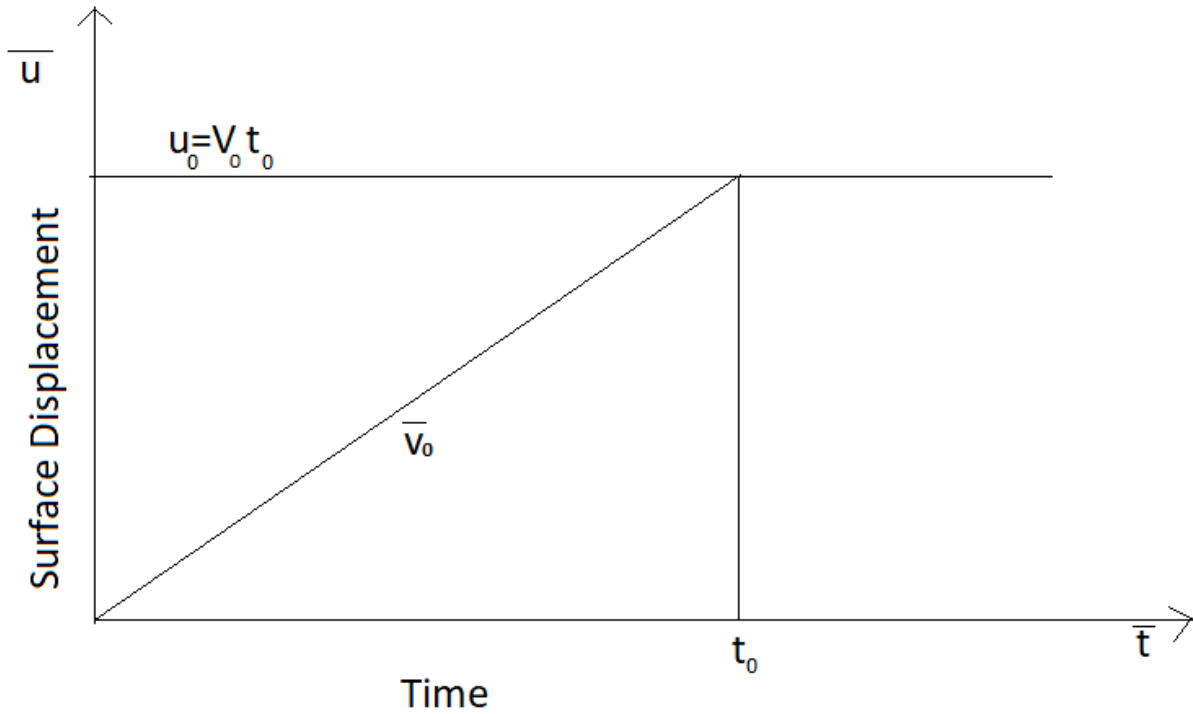


FIGURE 6.2: Graphical representation of a ramp displacement.

For the development of the model, we used biphasic mixture theory approach. The main idea behind the mixture theory is that each constituent of the mixture is continuous and occupies each point in the mixture. Furthermore, Mow *et al.* [168] has shown that, even for small rate of compression, mechanical response of the articular cartilage is extremely sensitive. Moreover, the permeability of the cartilage decreases significantly with the magnitude of the compression. This is given by the following mathematical relation:

$$\bar{\kappa} = \kappa_0 \exp \left(m \frac{\partial \bar{u}}{\partial \bar{x}} \right), \quad (6.1)$$

where κ_0 and m are material constants, $\bar{u}(\bar{x}, \bar{t})$ represents the solid displacement, $\kappa_0 = O(10^{-15})m^4 N^{-1}/s$, $\frac{\partial \bar{u}}{\partial \bar{x}}$ is the dilation, and the value of m ranges from 1 to 10 [92]. The conservation of mass for the incompressible binary mixture of solid and fluid can be written as

$$\nabla \cdot \mathbf{v}^f = -\alpha \nabla \cdot \mathbf{v}^s, \quad (6.2)$$

where \mathbf{v}^f and \mathbf{v}^s represent the velocity of fluid and solid, respectively, and α is the ratio from solid volume fraction to fluid volume fraction. The solid volume fraction is represented by $\phi^s = V^s/V$, and the fluid volume fraction (porosity) is $\phi^f = V^f/V$, where $V^s + V^f = V$ or $\phi^s + \phi^f = 1$. Equation (6.2) is deduced for a constant α (0.2 for an adult joint) and has been used by many authors in their studies [27, 92, 173]. The equation of momentum balance for the mixture can be written as

$$\rho^\beta \left(\frac{\partial \mathbf{v}^\beta}{\partial t} + (\mathbf{v}^\beta \cdot \nabla) \mathbf{v}^\beta \right) = \nabla \cdot \mathbf{T}^\beta + \rho^\beta \mathbf{b}^\beta + \boldsymbol{\pi}^\beta + \mathbf{J} \times \mathbf{B}, \quad (6.3)$$

where $\beta = f$, denotes the fluid, and $\beta = s$, the solid phase of the mixture. Here, ρ^β is the density, \mathbf{v}^β the velocity, \mathbf{T}^β the stress tensor, \mathbf{b}^β the net body force and $\boldsymbol{\pi}^\beta$ is the drag force for each phase. Furthermore, \mathbf{J} and \mathbf{B} represent the current density and magnetic flux density, respectively. The body forces are assumed zero except the magnetic field. Inertial terms appearing in equation (6.3) can usually be neglected for a particular choice of time scale [165] but our assumptions to neglect these terms due to small velocities and solid deformation rates, we get

$$\nabla \cdot \mathbf{T}^\beta = -\boldsymbol{\pi}^\beta - \mathbf{J} \times \mathbf{B}, \quad (6.4)$$

whereas Newton's third law implies that $\boldsymbol{\pi}^s = -\boldsymbol{\pi}^f$. Now, the generalized Ohms's law along with the Maxwell's equations can be written as (see Appendix A for details).

Moreover, when fluid flow becomes significant, viscoelastic effects, i.e. creep and stress relaxation caused by the diffusive resistance or frictional drag of relative fluid flow. In compression, many researchers [165, 168] have shown that this biphasic mechanism is a source for the viscoelastic behavior of the cartilage. The drag or diffusive resistant force between the constituents is given by the relation [92]

$$\boldsymbol{\pi}^s = K(\mathbf{v}^f - \mathbf{v}^s) + \dot{\mathbf{b}} \nabla e = -\boldsymbol{\pi}^f, \quad (6.5)$$

where K is the drag coefficient and $\dot{\mathbf{b}}$ the capillary force within the cartilage. It is

important to note that transfer of linear momentum between the constituents of mixture, i.e., fluid phase and solid phase is governed by the relative motion $v^f - v^s$ of fluid and solid phases. For slow flows, many authors [27, 92, 96, 168] have used the following relation in their studies that relates K with tissue permeability $\bar{\kappa}$ as

$$K = \frac{1}{\bar{\kappa}(1 + \alpha)^2}. \quad (6.6)$$

The linear biphasic modeling for cartilage is based on the assumptions that it consists of linearly elastic solid phase and linearly viscous fluid phase [168]. Linear elasticity is a branch of continuum mechanics and another mathematical approach to analyze how cartilage deforms. In compression, solid becomes internally stressed due to loading conditions. This theory is actually simplified form of non-linear theory of elasticity [174]. The fundamental assumptions of this theory are: 1) linearized relationship between the components of strain and stress; 2) small deformations or infinitesimal strain; 3) stress do not produce yielding in the material. Due to these assumptions, this theory is applied extensively in structural analysis such as biological tissues, buildings, bridges, furniture and vehicles, by using finite element analysis.

In 1660, Robert Hooke [175] introduced the classical relationship between strain and stress. Modern theory of elasticity generalized the Hooke's by saying "strain is directly proportional to the stress applied to it." Moreover, constant of proportionality is a tensor in a form of matrix with entries of real numbers. This matrix depends on the solid material that falls into the category of seven crystal classes [176]. Elastic solids can be categorized into two types, i.e., anisotropic and isotropic. The solid material considered in this study is a isotropic. This type of material exhibits properties that are independent of orientation (or direction). On the other hand, anisotropic is material having properties, change with direction along the material object. Several studies have been carried out using soft tissues by considering their solid phase as an isotropic material and the reference therein [92, 100]. Under the assumptions of linear elasticity, the solid stress \mathbf{T}^s of an isotropic, porous, intrinsically incompressible, permeable material filled with

fluid is given as [168]

$$\mathbf{T}^s = -\alpha\bar{p}\mathbf{I} + \lambda_s e\mathbf{I} + 2\mu_s \mathbf{e} + \bar{\lambda}_s \text{div}(\mathbf{v}^s)\mathbf{I} + 2\bar{\mu}_s \mathbf{D}^s - 2K_c \boldsymbol{\tau}, \quad (6.7)$$

where \bar{p} is a fluid pressure, \mathbf{I} is an identity tensor, \mathbf{e} the infinitesimal strain tensor, $e = \text{trace}(\mathbf{e})$, \mathbf{D}^s the rate of deformation tensor, $\boldsymbol{\tau}$ the spin tensor of the solid phase relative to the fluid phase whereas λ_s and μ_s are isotropic moduli, $\bar{\lambda}_s$ and $\bar{\mu}_s$ are viscoelastic moduli. Moreover, diffusive interaction between the fluid phase and the solid phase is represented by K_c . The stress Tensor \mathbf{T}^f of an incompressible fluid is given as [92]

$$\mathbf{T}^f = -\bar{p}\mathbf{I} + \lambda^f \text{div}(\mathbf{v}^f)\mathbf{I} + 2\mu^f \mathbf{D}^f + 2K_c \boldsymbol{\tau}, \quad (6.8)$$

where λ^f and μ^f are the bulk velocity and the dynamic velocity of the fluid, respectively. To model the compressive stress-relaxation behavior of cartilage, under the MHD effects would be very difficult using all material parameters ($\lambda_s, \mu_s, \bar{\lambda}_s, \bar{\mu}_s, K_c, \lambda^f, \mu^f, \dot{\mathbf{b}}, K$). Mow *et al.* [168] suggested a linear biphasic model for cartilage by assuming: 1) the solid matrix and fluid phase are strictly linearly elastic, i.e., $\bar{\lambda}_s = \bar{\mu}_s = 0, \lambda^f = \mu^f = 0$; 2) $K_c = 0$; 3) the material parameter for the capillary force coefficient $\dot{\mathbf{b}} = 0$; 4) $\alpha = \text{constant}$. Under these conditions, the resulting equations have been successfully applied to model the one-dimensional stress relaxation behavior of cartilage, nasal septum and meniscus. With these assumptions, the value of permeability constant has been calculated to be $O(10^{-15} \text{m}^4 \text{N}^{-1} \text{s}^{-1})$, almost similar to those calculated from permeability experiments [177, 178]. The linear equation governing the displacement component has been used to describe stress-relaxation and creep processes, and the processes are due to fluid distribution (stress-relaxation) and from the fluid exudation (creep) within the cartilage. However, Lai *et al.* [165] showed from a detailed comparison of the linear biphasic theory and the stress-relaxation experimental results that certain inconsistencies can be occurred if this theory is modified to include nonlinear (strain-dependent) permeability given in equation (6.1). Thus in our work, we will extend linear biphasic theory by including the relation of nonlinear permeability, under MHD

effects. For this, using generalized Ohm's law (A.4) and Maxwell's equations (A.7) along with equation (6.5) in equation (6.4), we obtain the following equations for solid and fluid phase as

$$\nabla \cdot \mathbf{T}^s = -K(\mathbf{v}^f - \mathbf{v}^s) + \sigma_0 B_0^2 \mathbf{v}^s, \quad (6.9)$$

$$\nabla \cdot \mathbf{T}^f = K(\mathbf{v}^f - \mathbf{v}^s) + \sigma_0 B_0^2 \mathbf{v}^f, \quad (6.10)$$

where B_0 represents the constant magnetic flux. Moreover, the contribution of the MHD effects to the modeling of the fluid flow through a deformable porous material is represented by the last term appearing in equations (6.9) and (6.10) [126]. Inserting the stress relations (6.7) and (6.8) into (6.9) and (6.10), yields

$$-\alpha \nabla \bar{p} + \lambda_s \nabla e + 2\mu_s \nabla \cdot \mathbf{e} + K(\mathbf{v}^f - \mathbf{v}^s) - \sigma_0 B_0^2 \mathbf{v}^s = 0, \quad (6.11)$$

$$\nabla \bar{p} = -K(\mathbf{v}^f - \mathbf{v}^s) - \sigma_0 B_0^2 \mathbf{v}^f. \quad (6.12)$$

Substituting equation (6.12) into equation (6.11), we get

$$K(1 + \alpha)(\mathbf{v}^f - \mathbf{v}^s) + \sigma_0 B_0^2(\alpha \mathbf{v}^f - \mathbf{v}^s) + 2\mu_s \nabla \cdot \mathbf{e} + \lambda_s \nabla e = 0. \quad (6.13)$$

Following Holmes *et al.* [92], the confined compression of the cartilage is one-dimensional, i.e., $\mathbf{v}^s = (v^s, 0, 0)$ and $\mathbf{v}^f = (v^f, 0, 0)$. The surface of the specimen tissue from $\bar{x} = 0$ plane to $\bar{x} = h$ defines the depth of the cartilage. With these assumptions, integrating the continuity equation (6.2) with respect to \bar{x} yields

$$v^f = -\alpha v^s + c, \quad (6.14)$$

where $v^f(\bar{x}, \bar{t})$ and $v^s(\bar{x}, \bar{t})$ represent respectively the solid velocity component and fluid velocity component in \bar{x} direction and c is the constant of integration. In (6.14), c equals to zero as the boundary at $\bar{x} = h$ is assumed to be impermeable and rigid (these conditions are true for adult joints only). Keeping in view equation

(6.14) and taking $v^s = \frac{\partial \bar{u}}{\partial \bar{t}}$, we obtain

$$v^f = -\alpha \frac{\partial \bar{u}}{\partial \bar{t}}, \quad (6.15)$$

where \bar{u} represents the dimensional axial solid displacement and \bar{t} the dimensional time. Using above equation, we can write equation (6.13) in scalar form as

$$K(\alpha + 1)^2 \frac{\partial \bar{u}}{\partial \bar{t}} + \sigma_0 B_0^2 (\alpha^2 + 1) \frac{\partial \bar{u}}{\partial \bar{t}} - (\lambda_s + 2\mu_s) \frac{\partial^2 \bar{u}}{\partial \bar{x}^2} = 0, \quad (6.16)$$

where \bar{x} is the dimensional coordinate in the axial direction. Using the relation for drag coefficient K from (6.6), equation (6.16) may be simplified to yield

$$\left(\frac{1 + \bar{\kappa} \sigma_0 B_0^2 (1 + \alpha^2)}{\bar{\kappa}} \right) \frac{\partial \bar{u}}{\partial \bar{t}} - (\lambda_s + 2\mu_s) \frac{\partial^2 \bar{u}}{\partial \bar{x}^2} = 0. \quad (6.17)$$

Using the relation (6.1) into equation (6.17), we obtain

$$\frac{\partial \bar{u}}{\partial \bar{t}} = \frac{\kappa_0 \exp\left(m \frac{d\bar{u}}{d\bar{x}}\right)}{1 + M \exp\left(m \frac{d\bar{u}}{d\bar{x}}\right)} \left(H_A \frac{\partial^2 \bar{u}}{\partial \bar{x}^2} \right), \quad (6.18)$$

where $M = \kappa_0 \sigma_0 B_0^2 (\alpha^2 + 1)$ represents the dimensionless magnetic parameter, $H_A = \lambda_s + 2\mu_s$ is the aggregate modulus. Equation (6.18) is required governing partial differential equation in terms of dimensional solid displacement \bar{u} as a function of distance \bar{x} and time \bar{t} . It is worth mentioning here that by substituting the magnetic parameter M equals to zero in equation (6.18), we recover the dimensional displacement equation in Holmes *et al.* [92]. Equation (6.18) is subject to the following initial condition

$$\bar{u}(\bar{x}, 0) = 0. \quad (6.19)$$

Moreover, a ramp displacement function defined the left boundary condition imposed on the $\bar{x} = 0$ surface as

$$\bar{u}(0, \bar{t}) = \begin{cases} V_0 \bar{t} & \text{for } 0 \leq \bar{t} \leq t_0 \quad (\text{for the compression stage}) \\ V_0 t_0 & \text{for } t_0 \leq \bar{t}. \quad (\text{for the relaxation stage}) \end{cases} \quad (6.20)$$

where V_0 is the rate of compression and t_0 represents the length of time for the compression stage. At the tissue/ calcified tissue junction, we have

$$\bar{u}(h, \bar{t}) = 0. \quad (6.21)$$

above equation represents dimensional boundary condition.

Furthermore, equations (6.11) and (6.12) may be simplified to yield

$$-\nabla \bar{p}(1 + \alpha) + 2\mu_s \nabla \cdot \mathbf{e} + \lambda \nabla e - \sigma_0 B_0^2 (\mathbf{v}^f + \mathbf{v}^s) = 0. \quad (6.22)$$

Using again the equation (6.15) and the relation $v^s = \frac{\partial \bar{u}}{\partial \bar{t}}$, we can write equation (6.22) in scalar form as

$$\frac{\partial \bar{p}}{\partial \bar{x}} = \frac{H_A}{1 + \alpha} \frac{\partial^2 \bar{u}}{\partial \bar{x}^2} - \frac{\sigma_0 B_0^2 (1 - \alpha)}{1 + \alpha} \frac{\partial \bar{u}}{\partial \bar{t}}. \quad (6.23)$$

After elimination of the $\frac{\partial \bar{u}}{\partial \bar{t}}$ from equations (6.18) and (6.23), we obtain

$$\frac{\partial \bar{p}}{\partial \bar{x}} = \frac{H_A}{1 + \alpha} \left\{ 1 - \frac{M(1 - \alpha) \exp\left(m \frac{d\bar{u}}{d\bar{x}}\right)}{(1 + \alpha^2) (1 + M \exp\left(m \frac{d\bar{u}}{d\bar{x}}\right))} \right\} \frac{\partial^2 \bar{u}}{\partial \bar{x}^2}, \quad (6.24)$$

subject to the following condition

$$\bar{p}(h, \bar{t}) = 0. \quad (6.25)$$

Equation (6.24) on integration and using the boundary condition (6.25) with $m = 0$, yields

$$\bar{p}(\bar{x}, \bar{t}) = \frac{H_A}{1 + \alpha} \left\{ 1 - \frac{M(1 - \alpha)}{(1 + \alpha^2) (1 + M)} \right\} \left(\frac{\partial \bar{u}(\bar{x}, \bar{t})}{\partial \bar{x}} - \frac{\partial \bar{u}(h, \bar{t})}{\partial \bar{x}} \right). \quad (6.26)$$

Note that on setting the magnetic parameter M equals to zero in the above equation, we recover the fluid pressure equation in Holmes *et al.* [92] in dimensional form. The mechanical response of the cartilage is extremely sensitive to the rate of compression V_0 . This behavior is due to the internal frictional dissipation, which

is the direct result of the fluid flow within the cartilage. This movement of the fluid within the cartilage can cause compaction of the solid matrix [96], and this deformation of the cartilage can influence the fluid flow.

Thus, analysis of the stress-relaxation behavior of cartilage with strain dependent permeability in compression, which is governed by the exudation of the interstitial fluid and redistribution of fluid within the cartilage, could help to understand additional insights into nonlinear solid fluid interaction process [168].

6.3 Non-Dimensionalization

The following set of normalized quantities are used to non-dimensionalize the solid displacement equation (6.18) and fluid pressure equation (6.26)

$$x = \frac{\bar{x}}{h}, \quad (6.27)$$

$$t = \frac{\bar{t}}{t_0}, \quad (6.28)$$

$$p = \frac{\bar{p}}{p_0}, \quad (6.29)$$

$$u = \frac{\bar{u}}{u_0} \quad (6.30)$$

where $u_0 = V_0 t_0$ and $p_0 = 1$ pascal.

The resulting PDEs take the following form, i.e., solid displacement

$$\frac{\partial u}{\partial t} = \frac{R^2 \exp\left(\epsilon m \frac{\partial u}{\partial x}\right)}{1 + M \exp\left(\epsilon m \frac{\partial u}{\partial x}\right)} \frac{\partial^2 u}{\partial x^2}, \quad (6.31)$$

where $R^2 = \frac{\kappa_0 t_0 H_A}{h^2}$ and $\epsilon = \frac{u_0}{h}$ are dimensionless parameters. From the equation (6.20), we have

$$u(0, t) = \begin{cases} t & \text{for } 0 \leq t \leq 1 \\ 1 & \text{for } 1 \leq t. \end{cases} \quad (6.32)$$

and, from equations (6.19) and (6.21),

$$u(x, 0) = 0, \quad (6.33)$$

$$u(1, t) = 0. \quad (6.34)$$

Moreover, utilizing the dimensionless parameters (6.27-6.30) in equation (6.26), we have the following dimensionless form of fluid pressure

$$p(x, t) = \frac{\epsilon H_A}{p_0(1 + \alpha)} \left\{ 1 - \frac{M(1 - \alpha)}{(1 + \alpha^2)(1 + M)} \right\} \left(\frac{\partial u(x, t)}{\partial x} - \frac{\partial u(1, t)}{\partial x} \right). \quad (6.35)$$

6.4 Solution Procedure

The governing equation for the solid displacement (6.31) is nonlinear due to presence of the nonlinear permeability $\exp\left(m\epsilon\frac{\partial u}{\partial x}\right)$, which makes it very difficult to solve analytically. In this problem, we employ Method of Lines (MOL). Generally, MOL is a semi-analytic technique used to solve time-dependent parabolic or elliptic PDEs [172, 179].

In order to complete all aspects of the problem for MOL, we discretize the spatial derivatives involved in governing equation using finite difference technique and leaving the time variable continuous to convert the PDE (6.31) into a system of

ODEs, we get

$$\frac{du_j}{dt} = \frac{R^2 \exp\left(m\epsilon \frac{u_{j+1}-u_{j-1}}{2dx}\right)}{1 + M \exp\left(m\epsilon \frac{u_{j+1}-u_{j-1}}{2dx}\right)} \left(\frac{u_{j+1} - 2u_j + u_{j-1}}{dx^2} \right), \quad j = 1, 2, 3, \dots, N, \quad (6.36)$$

where value of u_0 and u_{N+1} are obtained from left and right boundaries respectively, and

$$u_j = u(x_j, t), \quad dx = \frac{1}{N}, \quad x_j = jdx. \quad (6.37)$$

The value of initial condition at each node can be calculated from the equation (6.33) as

$$u(x_j, 0) = 0. \quad (6.38)$$

Thus, we have a system of N differential equations (6.36) with N initial conditions given in relation (6.38). These resulting ODE's are solved numerically using MATLAB's *ode23s* solver. Note that equation (6.35) gives the solution for fluid pressure $p(x, t)$ in the cartilage once the solid displacement $u(x, t)$ is known. For this, we discretize the space derivative in equation (6.35), we get

$$p(x_j, t) = \frac{\epsilon H_A}{p_0(1+\alpha)} \left(1 - \frac{M(1-\alpha)}{(1+\alpha^2)(1+M)} \right) \left(\frac{u_{j+1} - u_{j-1}}{2dx} - \frac{u_{N-1} + 3u_{N+1} - 4u_N}{2dx} \right). \quad (6.39)$$

On recalling the solution of solid displacement $u(x, t)$ in the above equation and using the MATLAB command `plot(x,p(end,:),'-')` to get the solution for fluid pressure $p(x, t)$. For an adult healthy cartilage the average values of H_A , κ_0 , ϵ , and h are $5.5 \times 10^5 \text{ Nm}^{-2}$, $4 \times 10^{-15} \text{ m}^4/\text{Ns}$, 0.05 and $1.5 \times 10^{-3} \text{ m}$, respectively [94]. On substituting these values, we get $R = 0.0313 \sqrt{t_0}$. Consequently, value of R is extremely small (< 1), if the time of compression is less than 1000 s. In this case, at the end of compression ($t = 1$), the deformation of the cartilage has not reached the tidemark and considered as fast rate of compression.

Furthermore, the value of R is greater than 1, if t_0 approaches the value much more greater than 1000 s and considered as slow rate of compression. It is worth mentioning here that by substituting the power-law index $n = 1$ and $M = 0$

in equation (6.31), the graph of solid displacement $u(x, t)$ for the time $t = 0.25$ reported by Holmes *et al.* [92], is recovered successfully as shown in Figure 6.3.

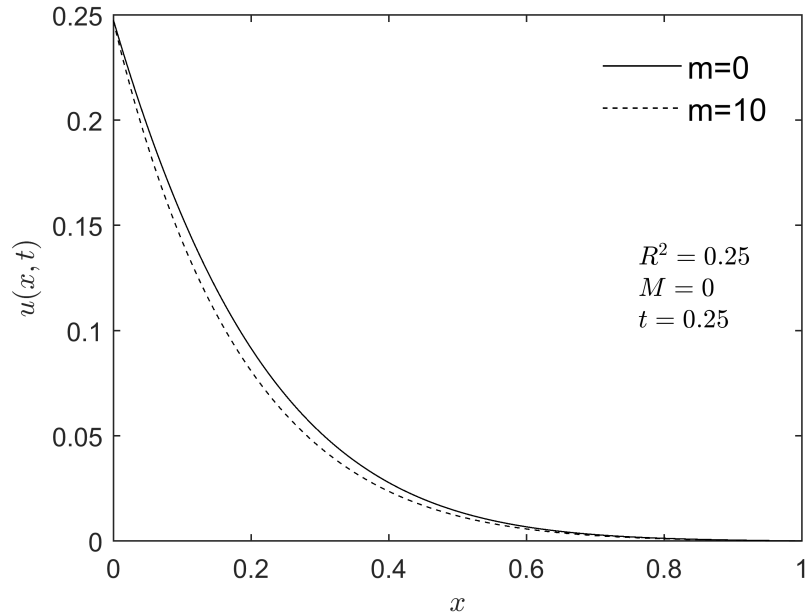


FIGURE 6.3: Solid displacement as a function of x at time $t = 0.25$ during fast rate of compression ($R^2 = 0.25$) when $M = 0$.

6.5 Results and Discussions

In this section, we outline the results of numerical simulations for solid displacement and fluid pressure for different values of magnetic parameter. In particular, graphical profiles are presented to highlight the effects of various values of magnetic parameter for linear permeability as well as for nonlinear permeability. Results are incorporated along with fast and slow rate of compression.

Figure 6.4 describes the influence of magnetic parameter M on solid displacement $u(x, t)$ for various times as a function of space for linear permeability $m = 0$. In particular, result shows for the fast rate of compression ($R^2 = 0.25$). This plot shows that the solid displacement decreases during fast rate of compression and drops off more rapidly with an increase of magnetic parameter.

Exudation of fluid from the cartilage increases due to Lorentz force associated with the magnetic field. This happens due to the fact that increase in strength of magnetic field reduces the viscosity of fluid and hence the exudation of fluid increases. Thus, strength of magnetic field can be used to control the fluid flow in cartilage. Moreover, for the fixed value of M , solid displacement increases with time and falls due to exudation of fluid. This behavior is consistent with the previous study [92], when magnetic effects are not present (i.e. $M = 0$).

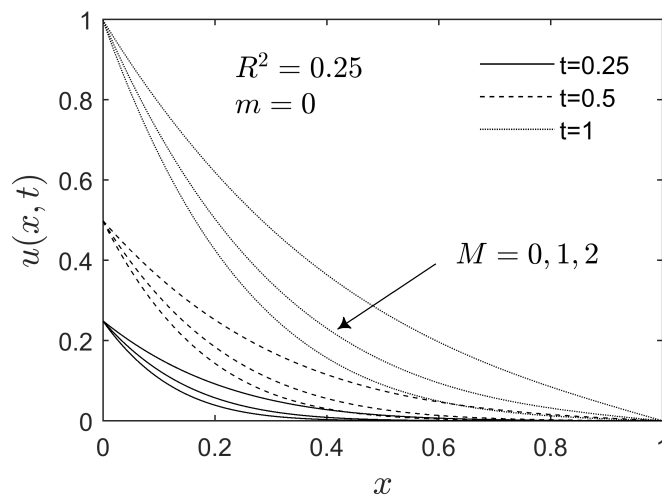


FIGURE 6.4: Solid displacement as a function of x for different values of M during fast rate of compression ($R^2 = 0.25$) at $t = 0.25, 0.5, 1.0$ when $m = 0$.

Figure 6.5 describes the influence of magnetic parameter M on solid displacement $u(x, t)$ for various times as a function of space for linear permeability $m = 0$. In particular, result shows for the slow rate of compression ($R^2 = 4$). As compared to the fast rate of compression, slow rate of compression slows down the exudation of the fluid, consequently solid deformation drops slowly. Interestingly, profile of solid displacement shows a similar behavior, but an increase in strength of the magnetic field has little effect on solid deformation as compared to fast rate of compression.

These effects are more profound in the middle of process and become linear at the end. This is due to the fact that fast rate of compression induces more charge as compared to the slow rate of compression.

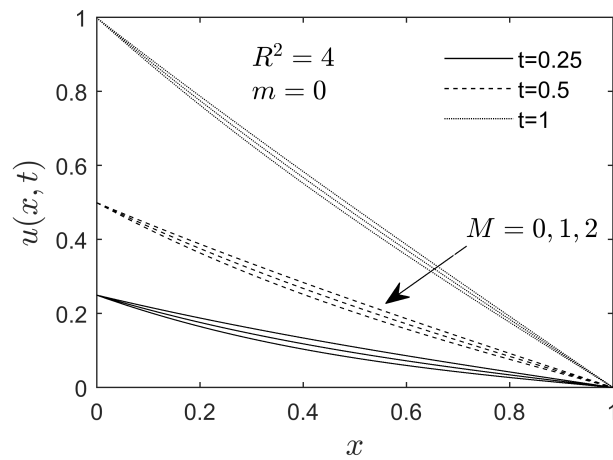


FIGURE 6.5: Solid displacement as a function of x for different values of M during slow rate of compression ($R^2 = 4$) at $t = 0.25, 0.5, 1.0$ when $m = 0$.

Figure 6.6 shows the effect of permeability parameter (m) on the solid displacement $u(x, t)$ in the presence of the magnetic field ($M \neq 0$) for the fast rate of compression. Graph suggests that strain-dependent permeability ($m \neq 0$) induces less solid deformation as compared to the linear permeability ($m = 0$). This predicts that strain-dependent permeability increases the permeability of the tissue, allows more fluid to flow, results in the reduction of the solid displacement. Note that for the fixed value of (m), solid deformation decreases with time. These observations are consistent with the previous study [92], when magnetic field ($M = 0$) is not present.

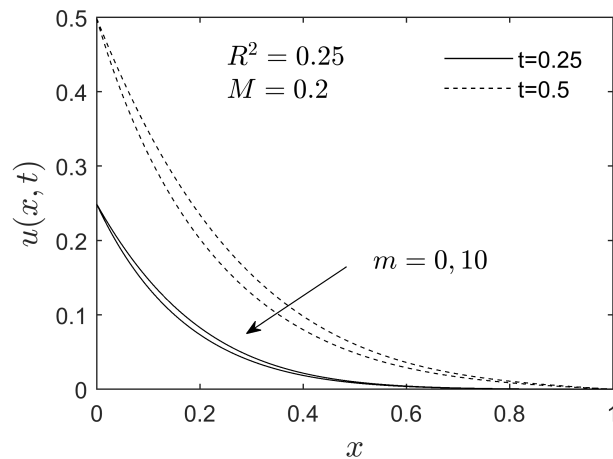


FIGURE 6.6: Solid displacement as a function of x for various values of permeability parameter m during fast rate of compression ($R^2 = 0.25$) at $t = 0.25, 0.5$ when $M = 0.2$.

Figure 6.7 shows the effect of permeability parameter (m) in the presence of the magnetic field ($M \neq 0$) for the slow rate of compression. Strain-dependent non-linear permeability induces less solid deformation as compared to the linear permeability. Interestingly, this effect is negligible as compared to the fast rate of compression. This predicts that rate of compression is also contributing with the permeability parameter in the permeability of the tissue.

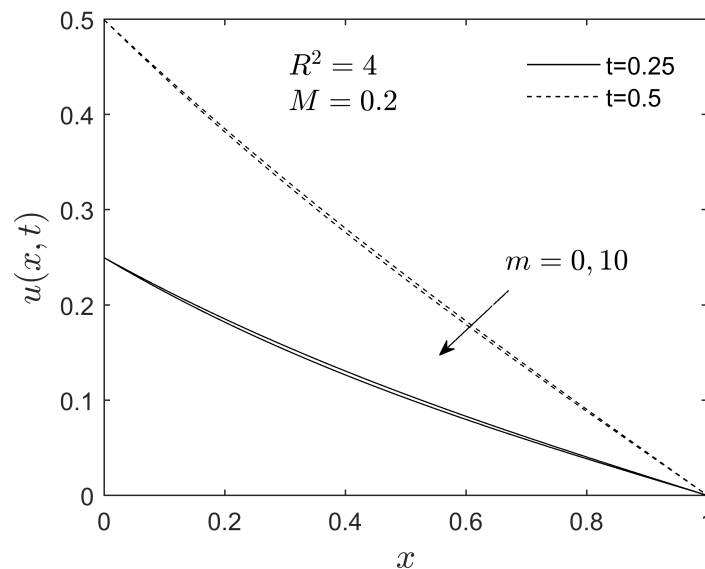


FIGURE 6.7: Solid displacement as a function of x for various values of permeability parameter m during slow rate of compression ($R^2 = 4$) at $t = 0.25, 0.5$ when $M = 0.2$.

Figure 6.8 describes the effect of magnetic parameter M for fast rate of compression ($R^2 = 0.25$) on the fluid pressure as a function of space x for linear permeability ($m = 0$) at $t = 0.1$.

The fluid pressure in the tissue increases with increase in magnetic parameter. This predicts that high strength in the magnetic field allows more fluid to flow through cartilage and induces more fluid pressure and this result is consistent with the previous discussion on solid deformation.

For the fixed value of magnetic parameter, the fluid pressure increases in the tissue for given time due to compression of the tissue and vanishes due to exudation of the fluid.

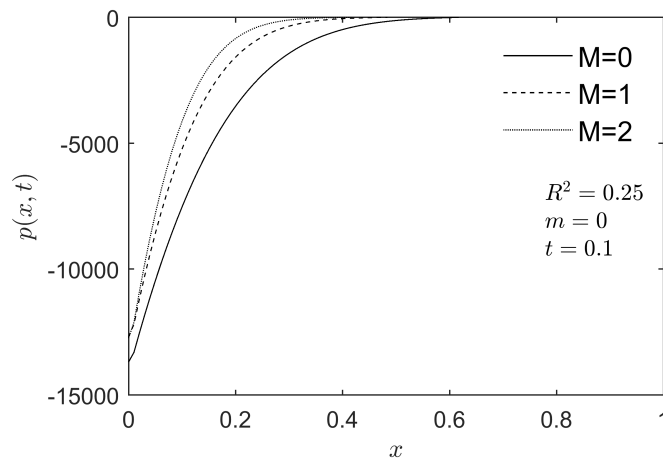


FIGURE 6.8: Fluid pressure as a function of x for various values of magnetic parameter M during fast rate of compression ($R^2 = 0.25$) at $t = 0.1$ when $m = 0$.

Figure 6.9 describes the effect of magnetic parameter M for the slow rate of compression ($R^2 = 1.2$) on the fluid pressure as a function of space x for linear permeability ($m = 0$) at $t = 0.01$. Graph shows that the increase in the magnetic field induces more fluid pressure vanishes quickly to zero as compared to the case when magnetic field is not present ($M = 0$). This is due to the fact that increase in the magnetic field increases the permeability and causes decrease in the solid deformation.

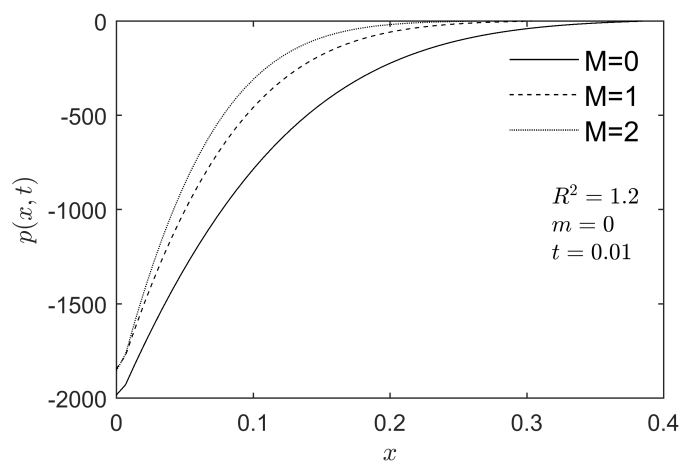


FIGURE 6.9: Fluid pressure as a function of x for various values of magnetic parameter M during slow rate of compression ($R^2 = 1.2$) at $t = 0.01$ when $m = 0$.

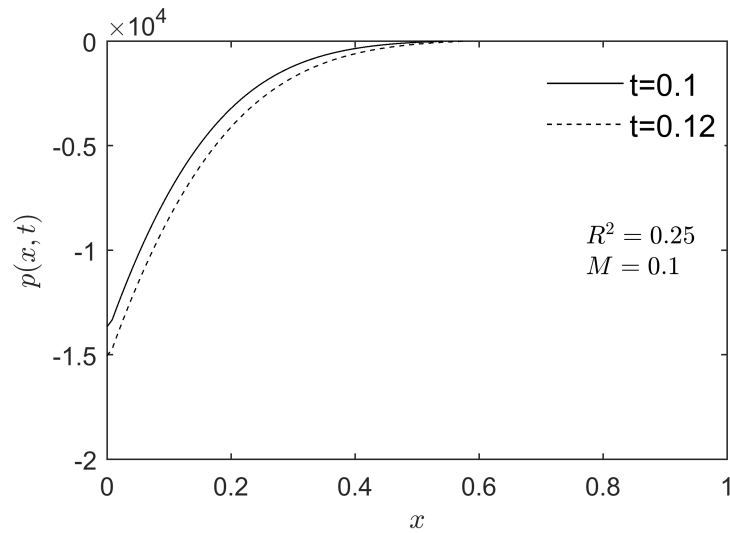


FIGURE 6.10: Fluid pressure as a function of x for various values of time t during fast rate of compression ($R^2 = 0.25$) when $M = 0.1$.

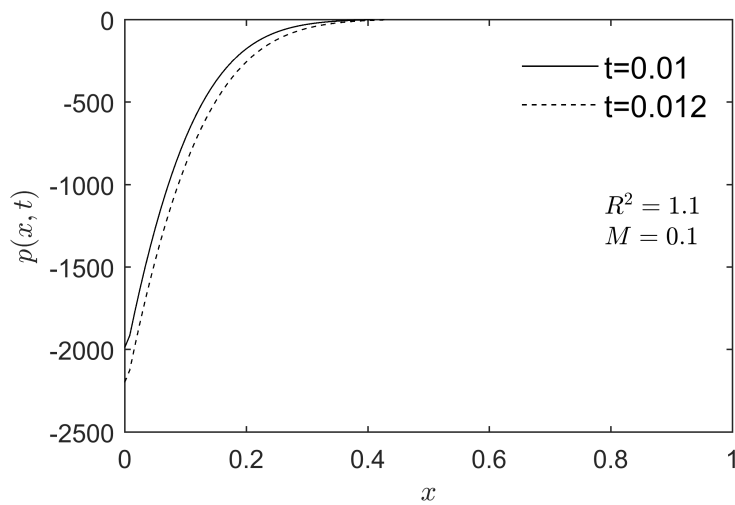


FIGURE 6.11: Fluid pressure as a function of x for various values of time t during slow rate of compression ($R^2 = 1.1$) when $M = 0.1$.

Figure 6.10 shows the profile of fluid pressure $p(x, t)$ as a function of distance x during the fast rate of compression ($R^2 = 0.25$) at time $t = 0.1, 0.12$ in the presence of magnetic parameter ($M = 0.1$). As time evolved, process moved towards equilibrium state. Curves show that pressure increases and becomes linear by attaining the equilibrium state. These curves show that pressure fluctuation is directly proportional to value of time t . Increase in time delays the equilibrium state.

Figure 6.11 shows the profile of fluid pressure $p(x, t)$ as a function of distance x during the slow rate of compression ($R^2 = 1.1$) at time $t = 0.01, 0.012$ in the presence of magnetic parameter ($M = 0.1$). As time evolved, process moved towards equilibrium state. Curves show that pressure increases and becomes linear by attaining the equilibrium state. These curves show that pressure fluctuation is directly proportional to value of time t . Increase in time delays the equilibrium state.

6.6 Conclusion

In this chapter, we have analyzed the stress relaxation behavior of the articular cartilage during compression under an applied magnetic field. The tissue considered in this study is assumed to be homogeneous, isotropic and linearly elastic. Mathematical model was developed using continuum mixture theory on the assumption that solid deformation is infinitesimal small. A numerical technique Method of Lines (MOL) was employed to solve the parabolic partial differential equation in terms of solid displacement which was then used to solve fluid pressure. Results are analyzed for the various values of magnetic and permeability parameters during fast and slow rate of compression. The summary of the results are as follows

- The strength of magnetic field behaves as a resistive force during fluid flow through the articular cartilage.
- The solid displacement decreases by increasing the magnetic parameter and this result is more profound during the fast rate of compression.
- For the fixed value of magnetic parameter, solid displacement increases by increasing the time range for the fast and slow rate of compression.
- Strain-dependent nonlinear permeability allows more fluid to pass through cartilage as compared to the linear permeability during compression.

- Fluid pressure increases and becomes linear by attaining the equilibrium state.
- For the fixed value of magnetic parameter, fluid pressure increases by increasing the time range.

We have explored the stress relaxation behavior of the cartilage with nonlinear permeability and MHD effects. Numerical results can be further improved theoretically and experimentally using sophisticated forms of permeability. Mathematical model can be further enhanced by adding additional features such as different geometries, evaporation and chemical interaction between fluid and articular cartilage.

Chapter 7

Conclusion and Future Work

In this thesis, we studied the non-Newtonian fluid flow and electrically conducting fluid flow through deformable porous materials and biological tissues. The modeling of these problems is based on continuum mixture theory. Below we summarize the conclusion of each problems along with the future directions.

7.1 Conclusion

Over the past four decades, interest to examine flow in deformable porous material has been developed due to its practical applications in industrial as well as a biological science. In this dissertation, compression molding process, ion-induced deformation and compressive stress relaxation behavior of articular cartilage are modeled using continuum mixture theory approach. Partial differential equations for the solid volume fraction, solid displacement and fluid pressure are obtained using Navier-Stokes equation and conservation of mass. Dimensional PDEs are non-dimensionalized using suitable choice of dimensionless parameters. Dimensionless PDEs are solved analytically as well as numerically using *pdepe* and Method of Lines. The solution of these problems are presented graphically. Below we summarize the main findings of this dissertation.

7.1.1 Non-Newtonian Flow in Deformable Porous Media: Modeling and Simulations of Compression Molding Processes

- Power-law fluids can be used for manufacturing of composite materials using compression molding process.
- Mathematical modeling of the compression molding process can be achieved using dynamics controlled either by pressure applied on piston or velocity of piston.
- In pressure driven dynamics, for shear-thinning fluid, there is sudden increase in solid volume fraction near the draining surface which increases with compression and brings the pre-impregnated pile to stage in which solid volume fraction is greatly inhomogeneous. There is increase in solid volume fraction for shear-thickening fluid but final state of pre-impregnated pile is homogeneous.
- Imbibition of fluid for pressure driven dynamics in a pre-impregnated pile can be observed in both cases of power law fluid.

7.1.2 Ion-induced Swelling Behavior of Articular Cartilage due to Non-Newtonian flow and its Effects on Fluid Pressure and Solid Displacement

- The salt concentration in articular cartilage increases with time and attains its maximum value at $t = 4$. After which the salt bath does not affect the ionic concentration.
- Under salt bath, the solid displacement in the cartilage decreased for shear-thinning and Newtonian fluid, but increased for the case of shear-thickening fluid.

- Shear-thinning fluid induces more fluid pressure as compared to the shear-thickening fluid.

7.1.3 Compressive Stress Relaxation Behavior of Articular Cartilage and its Effects on Fluid Pressure and Solid Displacement due to non-Newtonian Flow

- The solid displacement increases with an increase in power-law index during fast and slow rate of compression under stress-relaxation in compression.
- It is also observed that linear permeability induces more solid displacement as compared to the strain dependent nonlinear permeability.
- It is observed that shear-thinning fluid induces more fluid pressure as compared to the shear-thickening and Newtonian fluid.
- The solid deformation increases with an increase in power-law index n during compressive stress relaxation behavior of articular cartilage.
- Shear-thickening fluid induces more deformation as compared to the shear-thinning fluid and the Newtonian fluid during the fast and slow rate of compression.
- Numerical results also show that linear permeability induces more deformation as compared to the strain-dependent nonlinear permeability for shear-thinning and shear-thickening fluids.

7.1.4 Flow-Dependent Compressive Stress-Relaxation Behavior of Articular Cartilage with MHD Effects

- The strength of magnetic field behaves as a resistive force during fluid flow through the articular cartilage.
- The solid displacement decreases by increasing the magnetic parameter and this result is more profound during the fast rate of compression.

- For the fixed value of magnetic parameter, solid displacement increases by increasing the time range for the fast and slow rate of compression.
- For the fixed value of magnetic parameter or permeability parameter, fluid pressure increases by increasing the time range.

7.2 Future Direction

In the present work, continuum mixture theory is used to address some unsolved problems in industry and biomechanics. However, still there are many possible questions that need to be addressed and could be investigated theoretically and experimentally

- The effect of magnetohydrodynamics fluid on compression molding process can be considered.
- The non-Newtonian magnetohydrodynamics modeling of compression molding process may be undertaken.
- In this dissertation, we assumed that articular cartilage is isotropic and homogeneous, however, anisotropy and in-homogeneity of cartilage can also be considered for more accurate results.
- Consideration of evaporation, multidimensional solid displacement, multidimensional fluid pressure, and different permeability functions can improve the understanding of the solid-fluid interaction in articular cartilage.
- Consideration of non-Newtonian models other than the power-law model can also be investigated.
- In last, it is worth mentioning here that theoretical models are presented in this dissertation, however, a direct comparison of our divine models with experimental work will helpful in answering many interesting questions.

Bibliography

- [1] J. D. Humphrey, “Continuum biomechanics of soft biological tissues,” *Proceedings of the Royal Society of London. Series A: Mathematical, Physical and Engineering Sciences*, vol. 459, no. 2029, pp. 3–46, 2003.
- [2] X. Lopez, P. H. Valvatne, and M. J. Blunt, “Predictive network modeling of single-phase non-newtonian flow in porous media,” *Journal of colloid and interface science*, vol. 264, no. 1, pp. 256–265, 2003.
- [3] N. Petford, “Rheology of granitic magmas during ascent and emplacement,” *Annual Review of Earth and Planetary Sciences*, vol. 31, no. 1, pp. 399–427, 2003.
- [4] C. D. Tsakiroglou, “Correlation of the two-phase flow coefficients of porous media with the rheology of shear-thinning fluids,” *Journal of non-newtonian fluid mechanics*, vol. 117, no. 1, pp. 1–23, 2004.
- [5] E. S. Boek, J. Chin, and P. V. Coveney, “Lattice boltzmann simulation of the flow of non-newtonian fluids in porous media,” *International Journal of Modern Physics B*, vol. 17, no. 1, pp. 99–102, 2003.
- [6] D.-k. TONG and L. SHI, “The generalized flow analysis of non-newtonian visco-elastic fluid flows in porous media [j],” *Journal of Hydrodynamics, Ser. A*, vol. 18, no. 6, pp. 695–701, 2004.
- [7] S. J. Haward and J. A. Odell, “Viscosity enhancement in non-newtonian flow of dilute polymer solutions through crystallographic porous media,” *Rheologica acta*, vol. 42, no. 6, pp. 516–526, 2003.

-
- [8] T. Sochi, “Flow of non-newtonian fluids in porous media,” *Journal of Polymer Science Part B: Polymer Physics*, vol. 48, no. 23, pp. 2437–2767, 2010.
- [9] J. Siddique and D. Anderson, “Capillary rise of a non-newtonian liquid into a deformable porous material,” *Journal of Porous Media*, vol. 14, no. 12, 2011.
- [10] J. I. Siddique, F. A. Landis, and M. R. Mohyuddin, “Dynamics of drainage of power-law liquid into a deformable porous material,” *Open Journal of Fluid Dynamics*, vol. 4, no. 04, p. 403, 2014.
- [11] A. Farina, P. Cocito, and G. Boretto, “Flow in deformable porous media: modelling and simulations of compression moulding processes,” *Mathematical and Computer Modelling*, vol. 26, no. 11, pp. 1–15, 1997.
- [12] E. Masad, A. Al Omari, and H.-C. Chen, “Computations of permeability tensor coefficients and anisotropy of asphalt concrete based on microstructure simulation of fluid flow,” *Computational Materials Science*, vol. 40, no. 4, pp. 449–459, 2007.
- [13] T. B. Anderson and R. Jackson, “Fluid mechanical description of fluidized beds. equations of motion,” *Industrial & Engineering Chemistry Fundamentals*, vol. 6, no. 4, pp. 527–539, 1967.
- [14] T. Myers, G. Aldis, and S. Naili, “Ion induced deformation of soft tissue,” *Bulletin of mathematical biology*, vol. 57, no. 1, pp. 77–98, 1995.
- [15] A. Fick, “Ueber diffusion,” *Annalen der Physik*, vol. 170, no. 1, pp. 59–86, 1855.
- [16] J. Stefan, “Über das gleichgewicht und die bewegung, insbesondere die diffusion von gasgemengen, sitzungsberichte der mathematisch-naturwissenschaftlichen classe der kaiserlichen akademie der wissenschaften wien. 63 (abteilung ii): 63–124,” 1871.
- [17] W. Darcy, “Continuum mixture theory,” *Z Angew Math Mech*, vol. 1, pp. 121–151, 1851.

- [18] C. Truesdell and W. Noll, “The non-linear field theories of mechanics,” in *The non-linear field theories of mechanics*. Springer, 2004, pp. 1–579.
- [19] I. Müller, “A thermodynamic theory of mixtures of fluids,” *Archive for Rational Mechanics and Analysis*, vol. 28, no. 1, pp. 1–39, 1968.
- [20] R. Atkin and R. Craine, “Continuum theories of mixtures: basic theory and historical development,” *The Quarterly Journal of Mechanics and Applied Mathematics*, vol. 29, no. 2, pp. 209–244, 1976.
- [21] R. Bowen, “Theory of mixtures in continuum physics,” *Mixtures and Electromagnetic Field Theories*, vol. 3, 1976.
- [22] A. Bedford and D. S. Drumheller, “Theories of immiscible and structured mixtures,” *International Journal of Engineering Science*, vol. 21, no. 8, pp. 863–960, 1983.
- [23] K. Rajagopal and L. Tao, “Mechanics of mixtures,” *Journal of Fluid Mechanics*, vol. 323, pp. 410–410, 1996.
- [24] U. Farooq and J. Siddique, “Non-newtonian flow in deformable porous media: Modeling and simulations of compression molding processes,” *Journal of Porous Media*, vol. 23, no. 5, 2020.
- [25] S. M. Hosseini-Nasab, M. Taal, P. L. Zitha, and M. Sharifi, “Effect of newtonian and non-newtonian viscosifying agents on stability of foams in enhanced oil recovery. part i: under bulk condition,” *Iranian Polymer Journal*, vol. 28, no. 4, pp. 291–299, 2019.
- [26] N. A. Sami, D. S. Ibrahim, and A. A. Abdulrazaq, “Investigation of non-newtonian flow characterization and rheology of heavy crude oil,” *Petroleum Science and Technology*, vol. 35, no. 9, pp. 856–862, 2017.
- [27] E. Myers, W. Lai, and V. Mow, “A continuum theory and an experiment for the ion-induced swelling behavior of articular cartilage,” *Journal of biomechanical engineering*, vol. 106, no. 2, pp. 151–158, 1984.

- [28] J. Savins, "Non-newtonian flow through porous media," *Industrial & Engineering Chemistry*, vol. 61, no. 10, pp. 18–47, 1969.
- [29] A. Scheidegger, "The physics of flow through porous media, 1974," *University of Toronto, Toronto*, 1974.
- [30] R. B. Bird, E. N. Lightfoot, and W. E. Stewart, *Notes on Transport Phenomena. Transport Phenomena. By RB Bird, Warren E. Stewart, Edwin N. Lightfoot. A Rewritten and Enlarged Edition of "Notes on Transport Phenomena".* John Wiley & Sons, 1960.
- [31] W. Gogarty *et al.*, "Mobility control with polymer solutions," *Society of Petroleum Engineers Journal*, vol. 7, no. 02, pp. 161–173, 1967.
- [32] C. U. Ikoku and H. J. Ramey, "Transient flow of non-newtonian power-law fluids in porous media," *Society of Petroleum Engineers Journal*, vol. 19, no. 03, pp. 164–174, 1979.
- [33] A. Odeh, H. Yang *et al.*, "Flow of non-newtonian power-law fluids through porous media," *Society of Petroleum Engineers Journal*, vol. 19, no. 03, pp. 155–163, 1979.
- [34] C. U. Ikoku, H. J. Ramey Jr *et al.*, "Wellbore storage and skin effects during the transient flow of non-newtonian power-law fluids in porous media," *Society of Petroleum Engineers Journal*, vol. 20, no. 01, pp. 25–38, 1980.
- [35] O. Lund, C. U. Ikoku *et al.*, "Pressure transient behavior of non-newtonian/newtonian fluid composite reservoirs," *Society of Petroleum Engineers Journal*, vol. 21, no. 02, pp. 271–280, 1981.
- [36] C. U. Ikoku, "Well test analysis for enhanced oil recovery projects," *ASME J. Energy Resour. Technol*, vol. 104, no. 2, pp. 142–148, 1982.
- [37] C. Gencer and C. Ikoku, "Well test analysis for two-phase flow of non-newtonian power-law and newtonian fluids," *Journal of energy resources technology*, vol. 106, no. 2, pp. 295–305, 1984.

- [38] S. Vongvuthipornchai, R. Raghavan *et al.*, “Pressure falloff behavior in vertically fractured wells: Non-newtonian power-law fluids,” *SPE Formation Evaluation*, vol. 2, no. 04, pp. 573–589, 1987.
- [39] H. Van Poolen, J. Jargon *et al.*, “Steady-state and unsteady-state flow of non-newtonian fluids through porous media,” *Society of Petroleum Engineers Journal*, vol. 9, no. 01, pp. 80–88, 1969.
- [40] G. R. Kefayati, H. Tang, A. Chan, and X. Wang, “A lattice boltzmann model for thermal non-newtonian fluid flows through porous media,” *Computers & Fluids*, vol. 176, pp. 226–244, 2018.
- [41] P. K. Yadav and A. K. Verma, “Analysis of immiscible newtonian and non-newtonian micropolar fluid flow through porous cylindrical pipe enclosing a cavity,” *The European Physical Journal Plus*, vol. 135, no. 8, pp. 1–35, 2020.
- [42] Z. Cheng, Z. Ning, and S. Dai, “The electroviscous flow of non-newtonian fluids in microtubes and implications for nonlinear flow in porous media,” *Journal of Hydrology*, vol. 590, p. 125224, 2020.
- [43] S. Omirbekov, H. Davarzani, and A. Ahmadi-Senichault, “Experimental study of non-newtonian behavior of foam flow in highly permeable porous media,” *Industrial & Engineering Chemistry Research*, vol. 59, no. 27, pp. 12 568–12 579, 2020.
- [44] M. Kaczmarek and T. Hueckel, “Chemo-mechanical consolidation of clays: analytical solutions for a linearized one-dimensional problem,” *Transport in Porous Media*, vol. 32, no. 1, pp. 49–74, 1998.
- [45] M. Kaczmarek, “Chemically induced deformation of a porous layer coupled with advective–dispersive transport. analytical solutions,” *International journal for numerical and analytical methods in geomechanics*, vol. 25, no. 8, pp. 757–770, 2001.

- [46] G. P. Peters and D. W. Smith, “Solute transport through a deforming porous medium,” *International Journal for Numerical and Analytical Methods in Geomechanics*, vol. 26, no. 7, pp. 683–717, 2002.
- [47] K. Chen and L. Scriven, “Liquid penetration into a deformable porous substrate,” *Tappi journal*, vol. 73, no. 1, pp. 151–161, 1990.
- [48] A. Fitt, P. Howell, J. King, C. Please, and D. Schwendeman, “Multiphase flow in a roll press nip,” *European Journal of Applied Mathematics*, vol. 13, no. 3, pp. 225–259, 2002.
- [49] M. Spiegelman, “Flow in deformable porous media. part 1 simple analysis,” *Journal of Fluid Mechanics*, vol. 247, pp. 17–38, 1993.
- [50] J. Feng and S. Weinbaum, “Lubrication theory in highly compressible porous media: the mechanics of skiing, from red cells to humans,” *Journal of Fluid Mechanics*, vol. 422, pp. 281–317, 2000.
- [51] P. Johnson, M. Vaccaro, V. Starov, and A. Trybala, “Formation of sodium dodecyl sulfate foams by compression of soft porous material,” *Journal of Surfactants and Detergents*, 2021.
- [52] M. A. Biot, “General theory of three-dimensional consolidation,” *Journal of applied physics*, vol. 12, no. 2, pp. 155–164, 1941.
- [53] ———, “Consolidation settlement under a rectangular load distribution,” *Journal of Applied Physics*, vol. 12, no. 5, pp. 426–430, 1941.
- [54] M. A. Biot and F. Clingan, “Consolidation settlement of a soil with an impervious top surface,” *Journal of Applied Physics*, vol. 12, no. 7, pp. 578–581, 1941.
- [55] O. L. Manzoli, P. R. Cleto, M. Sánchez, L. J. Guimarães, and M. A. Maedo, “On the use of high aspect ratio finite elements to model hydraulic fracturing in deformable porous media,” *Computer Methods in Applied Mechanics and Engineering*, vol. 350, pp. 57–80, 2019.

- [56] X. Mou and Z. Chen, "Pore-scale simulation of heat and mass transfer in deformable porous media," *International Journal of Heat and Mass Transfer*, vol. 158, p. 119878, 2020.
- [57] H. H. Bui and G. D. Nguyen, "A coupled fluid-solid sph approach to modelling flow through deformable porous media," *International Journal of Solids and Structures*, vol. 125, pp. 244–264, 2017.
- [58] D. Purslow and R. Childs, "Autoclave moulding of carbon fibre-reinforced epoxies," *Composites*, vol. 17, no. 2, pp. 127–136, 1986.
- [59] R. K. Upadhyay and E. W. Liang, "Consolidation of advanced composites having volatile generation," *Polymer composites*, vol. 16, no. 1, pp. 96–108, 1995.
- [60] C. Hieber, "Injection and compression molding fundamentals," *ISATEV A I. Marael Dekker*, 1987.
- [61] P. K. Mallick, *Fiber-reinforced composites: materials, manufacturing, and design*. CRC press, 2007.
- [62] R. A. Tatara, "Compression molding," in *Applied plastics engineering handbook*. Elsevier, 2017, pp. 291–320.
- [63] M. Kamal, M. Ryan, and A. Isayev, "Injection and compression molding fundamentals," *Marcel Dekker, New York*, 1987.
- [64] P. Beardmore, J. Harwood, K. Kinsman, and R. Robertson, "Fiber-reinforced composites: Engineered structural materials," *Science*, pp. 833–840, 1980.
- [65] M. Biron, "Thermoplastics and thermoplastic composites. william andrew," 2012.
- [66] A. C. Long, *Composites forming technologies*. Elsevier, 2014.
- [67] D. G. Baird and D. I. Collias, *Polymer processing: principles and design*. John Wiley & Sons, 2014.

- [68] P. Dumont, L. Orgéas, D. Favier, P. Pizette, and C. Venet, “Compression moulding of smc: In situ experiments, modelling and simulation,” *Composites Part A: Applied Science and Manufacturing*, vol. 38, no. 2, pp. 353–368, 2007.
- [69] M. Miura, K. Hayashi, K. Yoshimoto, and N. Katahira, “Development of thermoplastic cfrp for stack frame,” SAE Technical Paper, Tech. Rep., 2016.
- [70] A. D. Bruce and T. Oswald, *Compression molding*. Hanser Publications: Cincinnati, OH, USA, 2003.
- [71] T. A. Osswald and C. L. Tucker III, “A boundary element simulation of compression mold filling,” *Polymer Engineering & Science*, vol. 28, no. 7, pp. 413–420, 1988.
- [72] S. G. Advani and C. L. Tucker III, “A numerical simulation of short fiber orientation in compression molding,” *Polymer composites*, vol. 11, no. 3, pp. 164–173, 1990.
- [73] A. Rios, B. Davis, and P. Gramann, “Computer aided engineering in compression molding,” in *CFA Technical Conference, Tampa Bay*, 2001.
- [74] M. Barone and D. Caulk, “A model for the flow of a chopped fiber reinforced polymer compound in compression molding,” 1986.
- [75] A. Ahmed and A. N. Alexandrou, “Compression molding using a generalized eulerian–lagrangian formulation with automatic remeshing,” *Advances in Polymer Technology: Journal of the Polymer Processing Institute*, vol. 11, no. 3, pp. 203–211, 1992.
- [76] D. E. Smith, D. A. Tortorelli, and C. L. Tucker III, “Analysis and sensitivity analysis for polymer injection and compression molding,” *Computer Methods in Applied Mechanics and Engineering*, vol. 167, no. 3-4, pp. 325–344, 1998.
- [77] I. Kim, S. Park, S. Chung, and T. Kwon, “Numerical modeling of injection/compression molding for center-gated disk: Part i. injection molding

- with viscoelastic compressible fluid model,” *Polymer Engineering & Science*, vol. 39, no. 10, pp. 1930–1942, 1999.
- [78] M. Dweib and C. Ó. Brádaigh, “Compression molding of glass reinforced thermoplastics: Modeling and experiments,” *Polymer composites*, vol. 21, no. 5, pp. 832–845, 2000.
- [79] A. Y. Yi and A. Jain, “Compression molding of aspherical glass lenses—a combined experimental and numerical analysis,” *Journal of the American Ceramic Society*, vol. 88, no. 3, pp. 579–586, 2005.
- [80] N. Meyer, L. Schöttl, L. Bretz, A. Hrymak, and L. Kärger, “Direct bundle simulation approach for the compression molding process of sheet molding compound,” *Composites Part A: Applied Science and Manufacturing*, vol. 132, p. 105809, 2020.
- [81] B.-A. Behrens, S. Hübner, C. Bonk, F. Bohne, and M. Micke-Camuz, “Development of a combined process of organic sheet forming and gmt compression molding,” *Procedia engineering*, vol. 207, pp. 101–106, 2017.
- [82] M. Jayavardhan, B. B. Kumar, M. Doddamani, A. K. Singh, S. E. Zeltmann, and N. Gupta, “Development of glass microballoon/hdpe syntactic foams by compression molding,” *Composites Part B: Engineering*, vol. 130, pp. 119–131, 2017.
- [83] J.-M. Lee, B.-M. Kim, and D.-C. Ko, “Development of vacuum-assisted prepreg compression molding for production of automotive roof panels,” *Composite Structures*, vol. 213, pp. 144–152, 2019.
- [84] W. Cao, Y. Shen, P. Wang, H. Yang, S. Zhao, and C. Shen, “Viscoelastic modeling and simulation for polymer melt flow in injection/compression molding,” *Journal of Non-Newtonian Fluid Mechanics*, vol. 274, p. 104186, 2019.
- [85] K. Chuaynukul, M. Nagarajan, T. Prodpran, S. Benjakul, P. Songtipya, and L. Songtipya, “Comparative characterization of bovine and fish gelatin films

- fabricated by compression molding and solution casting methods,” *Journal of Polymers and the Environment*, vol. 26, no. 3, pp. 1239–1252, 2018.
- [86] D. E. Kenyon, “The theory of an incompressible solid-fluid mixture,” *Archive for Rational Mechanics and Analysis*, vol. 62, no. 2, pp. 131–147, 1976.
- [87] D. Kenyon, “Transient filtration in a porous elastic cylinder,” *Journal of Applied Mechanics*, vol. 43, no. 4, pp. 594–598, 1976.
- [88] —, “Consolidation in compressible mixtures,” *Journal of Applied Mechanics*, vol. 45, no. 4, pp. 727–732, 1978.
- [89] G. Jayaraman, “Water transport in the arterial wall—a theoretical study,” *Journal of biomechanics*, vol. 16, no. 10, pp. 833–840, 1983.
- [90] R. Jain and G. Jayaraman, “A theoretical model for water flux through the artery wall,” *Journal of biomechanical engineering*, vol. 109, no. 4, pp. 311–317, 1987.
- [91] M. Klanchar and J. Tarbell, “Modeling water flow through arterial tissue,” *Bulletin of mathematical biology*, vol. 49, no. 6, pp. 651–669, 1987.
- [92] M. Holmes, W. Lai, and V. Mow, “Singular perturbation analysis of the nonlinear, flow-dependent compressive stress relaxation behavior of articular cartilage,” *Journal of biomechanical engineering*, vol. 107, no. 3, pp. 206–218, 1985.
- [93] V. C. Mow and W. Lai, “Mechanics of animal joints,” *Annual review of Fluid mechanics*, vol. 11, no. 1, pp. 247–288, 1979.
- [94] V. C. Mow, M. H. Holmes, and W. M. Lai, “Fluid transport and mechanical properties of articular cartilage: a review,” *Journal of biomechanics*, vol. 17, no. 5, pp. 377–394, 1984.
- [95] V. C. Mow and J. M. Mansour, “The nonlinear interaction between cartilage deformation and interstitial fluid flow,” *Journal of biomechanics*, vol. 10, no. 1, pp. 31–39, 1977.

- [96] W. M. Lai and V. C. Mow, "Drag-induced compression of articular cartilage during a permeation experiment," *Biorheology*, vol. 17, no. 1-2, pp. 111–123, 1980.
- [97] S. Kuei, W. Lai, and V. Mow, "A biphasic rheological model of articular cartilage," *Adv. Bioeng., AH Burstein, ed., ASME, New York*, pp. 17–18, 1978.
- [98] G. Ateshian, H. Wang, and W. Lai, "The role of interstitial fluid pressurization and surface porosities on the boundary friction of articular cartilage," *Journal of Tribology*, vol. 120, no. 2, pp. 241–248, 1998.
- [99] S. Barry and G. Aldis, "Flow-induced deformation from pressurized cavities in absorbing porous tissues," *Bulletin of mathematical biology*, vol. 54, no. 6, pp. 977–997, 1992.
- [100] —, "Comparison of models for flow induced deformation of soft biological tissue," *Journal of biomechanics*, vol. 23, no. 7, pp. 647–654, 1990.
- [101] M. R. Glucksberg, "Mechanics of the perialveolar interstitium of the lung," *Applied Cardiopulmonary Pathophysiology*, vol. 3, no. 3, pp. 247–251, 1990.
- [102] C. Oomens, D. Van Campen, and H. Grootenboer, "A mixture approach to the mechanics of skin," *Journal of biomechanics*, vol. 20, no. 9, pp. 877–885, 1987.
- [103] M. Friedman, "General theory of tissue swelling with application to the corneal stroma," *Journal of theoretical biology*, vol. 30, no. 1, pp. 93–109, 1971.
- [104] W. M. Lai, J. Hou, and V. C. Mow, "A triphasic theory for the swelling and deformation behaviors of articular cartilage," *Journal of biomechanical engineering*, vol. 113, no. 3, pp. 245–258, 1991.
- [105] W. Gu, W. Lai, and V. Mow, "A triphasic analysis of negative osmotic flows through charged hydrated soft tissues," *Journal of biomechanics*, vol. 30, no. 1, pp. 71–78, 1997.

- [106] D. Sun, W. Gu, X. Guo, W. Lai, and V. Mow, "A mixed finite element formulation of triphasic mechano-electrochemical theory for charged, hydrated biological soft tissues," *International Journal for Numerical Methods in Engineering*, vol. 45, no. 10, pp. 1375–1402, 1999.
- [107] I. Muir, "The chemistry of the ground substance of joint cartilage," in *The joints and synovial fluid*. Elsevier, 1980, pp. 27–94.
- [108] A. Maroudas, "Biophysical chemistry of cartilaginous tissues with special reference to solute and fluid transport," *Biorheology*, vol. 12, no. 3-4, pp. 233–248, 1975.
- [109] A. Bodine, N. Brown, W. Hayes, and S. Jiminez, "The effect of sodium chloride on the shear modulus of articular cartilage," *Trans ORS*, vol. 5, p. 137, 1980.
- [110] S. M. Elmore, L. Sokoloff, G. Norris, and P. Carmeci, "Nature of " imperfect" elasticity of articular cartilage," *Journal of Applied Physiology*, vol. 18, no. 2, pp. 393–396, 1963.
- [111] W. Gu, W. Lai, and V. Mow, "A mixture theory for charged-hydrated soft tissues containing multi-electrolytes: passive transport and swelling behaviors," *Journal of Biomechanical Engineering*, vol. 120, no. 2, pp. 169–180, 1998.
- [112] T. Ricken, A. Schwarz, and J. Bluhm, "A triphasic theory for growth in biological tissue—basics and applications," *Materialwissenschaft und Werkstofftechnik: Entwicklung, Fertigung, Prüfung, Eigenschaften und Anwendungen technischer Werkstoffe*, vol. 37, no. 6, pp. 446–456, 2006.
- [113] W. Gu, W. M. Lai, and V. C. Mow, "Generalized triphasic theory for multi-electrolyte transport in charged hydrated soft tissues," in *Proceedings of the 1994 International Mechanical Engineering Congress and Exposition*. ASME, 1994, pp. 217–218.

-
- [114] A. J. H. Frijns, J. Huyghe, and J. D. Janssen, “A validation of the quadriphasic mixture theory for intervertebral disc tissue,” *International Journal of Engineering Science*, vol. 35, no. 15, pp. 1419–1429, 1997.
- [115] C. Cyron and J. Humphrey, “Growth and remodeling of load-bearing biological soft tissues,” *Meccanica*, vol. 52, no. 3, pp. 645–664, 2017.
- [116] M. Latorre and J. D. Humphrey, “A mechanobiologically equilibrated constrained mixture model for growth and remodeling of soft tissues,” *ZAMM-Journal of Applied Mathematics and Mechanics/Zeitschrift für Angewandte Mathematik und Mechanik*, vol. 98, no. 12, pp. 2048–2071, 2018.
- [117] T. J. Truster and A. Masud, “A unified mixture formulation for density and volumetric growth of multi-constituent solids in tissue engineering,” *Computer Methods in Applied Mechanics and Engineering*, vol. 314, pp. 222–268, 2017.
- [118] M. Pourjafar, B. Taghilou, S. Taghavi, and K. Sadeghy, “On the use of biphasic mixture theory for investigating the linear stability of viscous flow through a channel lined with a viscoelastic porous bio-material,” *International Journal of Non-Linear Mechanics*, vol. 105, pp. 200–211, 2018.
- [119] A. Ahmed, J. Siddique, and A. Mahmood, “Non-newtonian flow-induced deformation from pressurized cavities in absorbing porous tissues,” *Computer methods in biomechanics and biomedical engineering*, vol. 20, no. 13, pp. 1464–1473, 2017.
- [120] U. Farooq and J. Siddique, “Compressive stress relaxation behavior of articular cartilage and its effects on fluid pressure and solid displacement due to non-newtonian flow,” *Computer Methods in Biomechanics and Biomedical Engineering*, vol. 24, no. 2, pp. 161–172, 2021.
- [121] D. Ambrosi and L. Preziosi, “On the closure of mass balance models for tumor growth,” *Mathematical Models and Methods in Applied Sciences*, vol. 12, no. 05, pp. 737–754, 2002.

- [122] L. Preziosi and G. Vitale, “A multiphase model of tumor and tissue growth including cell adhesion and plastic reorganization,” *Mathematical Models and Methods in Applied Sciences*, vol. 21, no. 09, pp. 1901–1932, 2011.
- [123] L. Preziosi, *Cancer modelling and simulation*. CRC Press, 2003.
- [124] D. Ambrosi, L. Preziosi, and G. Vitale, “The insight of mixtures theory for growth and remodeling,” *Zeitschrift für angewandte Mathematik und Physik*, vol. 61, no. 1, pp. 177–191, 2010.
- [125] G. Ateshian and J. Humphrey, “Continuum mixture models of biological growth and remodeling: past successes and future opportunities,” *Annual review of biomedical engineering*, vol. 14, pp. 97–111, 2012.
- [126] N. T. Eldabe, G. Saddeek, and K. Elagamy, “Magnetohydrodynamic flow of a bi-viscosity fluid through porous medium in a layer of deformable material,” *Journal of Porous Media*, vol. 14, no. 3, 2011.
- [127] J. Siddique and A. Kara, “Capillary rise of magnetohydrodynamics liquid into deformable porous material.” *Journal of Applied Fluid Mechanics*, vol. 9, no. 6, 2016.
- [128] A. Naseem, A. Mahmood, J. Siddique, and L. Zhao, “Infiltration of mhd liquid into a deformable porous material,” *Results in physics*, vol. 8, pp. 71–75, 2018.
- [129] S. Sreenadh, K. Prasad, H. Vaidya, E. Sudhakara, G. G. Krishna, and M. Krishnamurthy, “Mhd couette flow of a jeffrey fluid over a deformable porous layer,” *International Journal of Applied and Computational Mathematics*, vol. 3, no. 3, pp. 2125–2138, 2017.
- [130] A. Ahmed and J. I. Siddique, “The effect of magnetic field on flow induced-deformation in absorbing porous tissues,” *Mathematical Biosciences and Engineering*, vol. 16, no. 2, pp. 603–618, 2019.

- [131] U. Ali and J. I. Siddique, "Visco-elastic behavior of articular cartilage under applied magnetic field and strain-dependent permeability," *Computer Methods in Biomechanics and Biomedical Engineering*, pp. 1–12, 2020.
- [132] M. Zahn and K. Shenton, "Magnetic fluids bibliography," *IEEE Transactions on Magnetism*, vol. 16, no. 2, pp. 387–415, 1980.
- [133] C. Brighton, Z. Friedenber, E. Mitchell, and R. Booth, "Treatment of nonunion with constant direct current." *Clinical orthopaedics and related research*, no. 124, pp. 106–123, 1977.
- [134] J. Bagwell, J. Klawitter, B. Sauer, and A. Weinstein, "A study of bone growth into porous polyethylene," in *Sixth Annual Biomaterials Symposium, Clemson University, Clemson, SC, USA*, 1974, pp. 20–24.
- [135] R. Elco and W. Hughes, "Magneto-hydrodynamic pressurization of liquid metal bearings," *Wear*, vol. 5, no. 3, pp. 198–212, 1962.
- [136] Y. Yamamoto and S. Gondo, "Effect of a magnetic field on boundary lubrication," *Tribology international*, vol. 20, no. 6, pp. 342–346, 1987.
- [137] P. Tandon, A. Chaurasia, V. Jain, and T. Gupta, "Application of magnetic fields to synovial joints," *Computers & Mathematics with Applications*, vol. 22, no. 12, pp. 33–45, 1991.
- [138] L. Yiwen, Z. Bailing, L. Yinghong, X. Lianghua, W. Yutian, and H. Guoqiang, "Applications and prospects of magnetohydrodynamics in aeronautical engineering," *Advances in Mechanics*, vol. 47, no. 1, pp. 452–502, 2017.
- [139] S. Rashidi, J. A. Esfahani, and M. Maskaniyan, "Applications of magnetohydrodynamics in biological systems-a review on the numerical studies," *Journal of Magnetism and Magnetic Materials*, vol. 439, pp. 358–372, 2017.
- [140] P. Liu and G.-F. Chen, *Porous materials: processing and applications*. Elsevier, 2014.
- [141] T. Hanai, "Separation of polar compounds using carbon columns," *Journal of Chromatography A*, vol. 989, no. 2, pp. 183–196, 2003.

- [142] C.-W. Huang, Y.-T. Wu, C.-C. Hu, and Y.-Y. Li, “Textural and electrochemical characterization of porous carbon nanofibers as electrodes for supercapacitors,” *Journal of Power Sources*, vol. 172, no. 1, pp. 460–467, 2007.
- [143] R.-B. Lin, S. Xiang, H. Xing, W. Zhou, and B. Chen, “Exploration of porous metal–organic frameworks for gas separation and purification,” *Coordination chemistry reviews*, vol. 378, pp. 87–103, 2019.
- [144] J. Gröttrup, F. Schütt, D. Smazna, O. Lupan, R. Adelung, and Y. K. Mishra, “Porous ceramics based on hybrid inorganic tetrapodal networks for efficient photocatalysis and water purification,” *Ceramics International*, vol. 43, no. 17, pp. 14 915–14 922, 2017.
- [145] F. Su, F. Y. Lee, L. Lv, J. Liu, X. N. Tian, and X. S. Zhao, “Sandwiched ruthenium/carbon nanostructures for highly active heterogeneous hydrogenation,” *Advanced Functional Materials*, vol. 17, no. 12, pp. 1926–1931, 2007.
- [146] B. Lagree, “Modelling of two-phase flow in porous media with volume-of-fluid method,” Ph.D. dissertation, Paris 6, 2014.
- [147] H. P. G. Darcy, *Les Fontaines publiques de la ville de Dijon. Exposition et application des principes à suivre et des formules à employer dans les questions de distribution d’eau, etc.* V. Dalamont, 1856.
- [148] “Medlineplus,” @<https://medlineplus.gov/ency/imagepages/8682.htm>.
- [149] M. L. Bansal, *Magneto Therapy*. Jain Publisher, New Delhi, 1976.
- [150] G. Thirivikraman, S. K. Boda, and B. Basu, “Unraveling the mechanistic effects of electric field stimulation towards directing stem cell fate and function: A tissue engineering perspective,” *Biomaterials*, vol. 150, pp. 60–86, 2018.
- [151] S. Sengupta and V. K. Balla, “A review on the use of magnetic fields and ultrasound for non-invasive cancer treatment,” *Journal of advanced research*, vol. 14, pp. 97–111, 2018.

- [152] X. Guo, W. Li, L. Luo, Z. Wang, Q. Li, F. Kong, H. Zhang, J. Yang, C. Zhu, Y. Du *et al.*, “External magnetic field-enhanced chemo-photothermal combination tumor therapy via iron oxide nanoparticles,” *ACS applied materials & interfaces*, vol. 9, no. 19, pp. 16 581–16 593, 2017.
- [153] J. A. Thorp, K. Thorp, E. K. Lile, and J. Viglione, “Unexpected magnetic attraction: Evidence for an organized energy field in the human body,” 2021.
- [154] M. Epstein, *The elements of continuum biomechanics*. John Wiley & Sons, 2012.
- [155] L. Fusi, A. Farina, and D. Ambrosi, “Mathematical modeling of a solid–liquid mixture with mass exchange between constituents,” *Mathematics and mechanics of solids*, vol. 11, no. 6, pp. 575–595, 2006.
- [156] S. Hamdi, W. E. Schiesser, and G. W. Griffiths, “Method of lines,” *Scholarpedia*, vol. 2, no. 7, p. 2859, 2007.
- [157] Y. R. Kim, S. P. McCarthy, and J. P. Fanucci, “Compressibility and relaxation of fiber reinforcements during composite processing,” *Polymer composites*, vol. 12, no. 1, pp. 13–19, 1991.
- [158] D. Ambrosi and L. Preziosi, “Modelling matrix injection through elastic porous preforms,” *Composites Part A: Applied Science and Manufacturing*, vol. 29, no. 1-2, pp. 5–18, 1998.
- [159] S. Barry, K. Parkerf, and G. Aldis, “Fluid flow over a thin deformable porous layer,” *Zeitschrift für angewandte Mathematik und Physik ZAMP*, vol. 42, no. 5, pp. 633–648, 1991.
- [160] L. Preziosi, “The theory of deformable porous media and its application to composite material manufacturing,” *Surveys on Mathematics for Industry*, vol. 6, no. 3, pp. 167–214, 1996.
- [161] D. M. Anderson, “Imbibition of a liquid droplet on a deformable porous substrate,” *Physics of Fluids*, vol. 17, no. 8, p. 087104, 2005.

- [162] D. E. Kenyon, "A mathematical model of water flux through aortic tissue," *Bulletin of mathematical biology*, vol. 41, no. 1, pp. 79–90, 1979.
- [163] M. Klanchar and J. Tarbell, "Modeling water flow through arterial tissue," *Bulletin of mathematical biology*, vol. 49, no. 6, pp. 651–669, 1987.
- [164] C. Oomens, D. Van Campen, and H. Grootenboer, "A mixture approach to the mechanics of skin," *Journal of biomechanics*, vol. 20, no. 9, pp. 877–885, 1987.
- [165] W. Lai, V. C. Mow, and V. Roth, "Effects of nonlinear strain-dependent permeability and rate of compression on the stress behavior of articular cartilage," *Journal of biomechanical engineering*, vol. 103, no. 2, pp. 61–66, 1981.
- [166] M. K. Kwan, W. M. Lai, and V. C. Mow, "A finite deformation theory for cartilage and other soft hydrated connective tissues—i. equilibrium results," *Journal of biomechanics*, vol. 23, no. 2, pp. 145–155, 1990.
- [167] A. Ahmed and J. Siddique, "Ion-induced deformation of articular cartilage with strain-dependent nonlinear permeability and mhd effects," *Journal of Porous Media*, 2021.
- [168] V. C. Mow, S. Kuei, W. M. Lai, and C. G. Armstrong, "Biphasic creep and stress relaxation of articular cartilage in compression: theory and experiments," *Journal of biomechanical engineering*, vol. 102, no. 1, pp. 73–84, 1980.
- [169] V. C. Mow, M. H. Holmes, and W. M. Lai, "Fluid transport and mechanical properties of articular cartilage: a review," *Journal of biomechanics*, vol. 17, no. 5, pp. 377–394, 1984.
- [170] R. M. Schinagl, D. Gurskis, A. C. Chen, and R. L. Sah, "Depth-dependent confined compression modulus of full-thickness bovine articular cartilage," *Journal of Orthopaedic Research*, vol. 15, no. 4, pp. 499–506, 1997.

- [171] C. C. Wang, C. T. Hung, and V. C. Mow, "An analysis of the effects of depth-dependent aggregate modulus on articular cartilage stress-relaxation behavior in compression," *Journal of Biomechanics*, vol. 34, no. 1, pp. 75–84, 2001.
- [172] R. E. White and V. R. Subramanian, *Computational methods in chemical engineering with maple*. Springer Science & Business Media, 2010.
- [173] C. Armstrong, W. Lai, and V. Mow, "An analysis of the unconfined compression of articular cartilage," *Journal of biomechanical engineering*, vol. 106, no. 2, pp. 165–173, 1984.
- [174] R. W. Ogden, *Non-linear elastic deformations*. Courier Corporation, 1997.
- [175] R. Hooke, *Lectures de potentia restitutiva, or of spring explaining the power of springing bodies*. John Martyn, 2016, no. 6.
- [176] D. Royer and E. Dieulesaint, *Elastic waves in solids I: Free and guided propagation*. Springer Science & Business Media, 1999.
- [177] C. W. McCutchen, "The frictional properties of animal joints," *Wear*, vol. 5, no. 1, pp. 1–17, 1962.
- [178] J. M. Mansour and V. C. Mow, "The permeability of articular cartilage under compressive strain and at high pressures." *The Journal of bone and joint surgery. American volume*, vol. 58, no. 4, pp. 509–516, 1976.
- [179] W. E. Schiesser and G. W. Griffiths, *A compendium of partial differential equation models: method of lines analysis with Matlab*. Cambridge University Press, 2009.
- [180] N. T. Eldabe, G. Saddeek, and K. Elagamy, "Magnetohydrodynamic flow of a bi-viscosity fluid through porous medium in a layer of deformable material," *Journal of Porous Media*, vol. 14, no. 3, 2011.
- [181] V. Rossow, "On flow of electrically conducting fluids over a flat plate in the presence of a transverse magnetic field," *NACA Rept*, no. 1358, 1958.

-
- [182] A. Hussanan, Z. Ismail, I. Khan, A. G. Hussein, and S. Shafie, “Unsteady boundary layer mhd free convection flow in a porous medium with constant mass diffusion and newtonian heating,” *The European Physical Journal Plus*, vol. 129, no. 3, pp. 1–16, 2014.

Appendix A

Magnetohydrodynamics (MHD)

Equations for a Biphasic Mixture of Solid Phase and a Fluid Phase

A deformable porous material is considered which is assumed to be a continuous mixture of an incompressible solid phase and a magnetic fluid phase. Each point in the binary mixture is occupied by constituents of the mixture. Conservation of balance of mass for the solid and a fluid phase can be written as [99]

$$\frac{\partial \rho^s}{\partial t} + \nabla \cdot (\rho^s \mathbf{v}^s) = 0, \quad (\text{A.1})$$

$$\frac{\partial \rho^f}{\partial t} + \nabla \cdot (\rho^f \mathbf{v}^s) = -\gamma p, \quad (\text{A.2})$$

where \mathbf{v}^s , \mathbf{v}^f are the velocities, and ρ^s , ρ^f are the densities of solid and fluid phases, respectively, p be the fluid pressure and γ is a constant of proportionality. Conservation of balance of linear momentum for solid and fluid phases can be written as

$$\rho^\beta \left(\frac{\partial \mathbf{v}^\beta}{\partial t} + (\mathbf{v}^\beta \cdot \nabla) \mathbf{v}^\beta \right) = \nabla \cdot \mathbf{T}^\beta + \rho^\beta \mathbf{b}^\beta + \boldsymbol{\pi}^\beta + \mathbf{J} \times \mathbf{B}, \quad (\text{A.3})$$

where $\beta = s$ represents the solid phase and $\beta = f$ represents the fluid phase, $\mathbf{T}^\beta = -\phi^\beta p \mathbf{I} + \boldsymbol{\sigma}^\beta$ represents stress tensor for the β phase, \mathbf{I} is the identity tensor, ϕ^β represents volume fraction of β phase, here $\boldsymbol{\pi}^s = -\boldsymbol{\pi}^f = K (\mathbf{v}^f - \mathbf{v}^s) + p \nabla \phi^s$ is the friction force term which satisfies $\boldsymbol{\pi}^f + \boldsymbol{\pi}^s = 0$. Here K is the drag coefficient of relative motion between solid and fluid phases and $\boldsymbol{\sigma}^\beta$ is the stress of β phase. Moreover, \mathbf{b}^β is the net force, whereas gravitational forces are neglected, current density is represented by \mathbf{J} and magnetic flux density is represented by \mathbf{B} . Now, the generalized Ohm's law along with the Maxwell's equations are [180]

$$\mathbf{J} = \sigma_o (\mathbf{E} + \mathbf{v}^\beta \times \mathbf{B}), \quad (\text{A.4})$$

$$\text{div} \mathbf{B} = 0, \quad (\text{A.5})$$

$$\text{curl} \mathbf{B} = \mu_c \mathbf{J}, \quad (\text{A.6})$$

$$\text{curl} \mathbf{E} = -\frac{\partial \mathbf{B}}{\partial t}, \quad (\text{A.7})$$

where σ_o is the electric conductivity of fluid, μ_c corresponds to the permeability of free space and \mathbf{E} is the electric field. The term $\mathbf{J} \times \mathbf{B}$ of Lorentz force in the momentum balance equation (A.3) can be written in terms of Ohm's law as

$$\mathbf{J} \times \mathbf{B} = \sigma_o (\mathbf{E} + \mathbf{v}^\beta \times \mathbf{B}) \times \mathbf{B}, \quad (\text{A.8})$$

the decomposition of total magnetic field \mathbf{B} is given as [181, 182], $\mathbf{B} = \mathbf{b} + \mathbf{B}_o$, where \mathbf{b} represents the induced magnetic field and \mathbf{B}_o is the imposed magnetic field. It is worth mentioning that \mathbf{b} may be ignored due to low magnetic field Reynolds number. After neglecting electric and magnetic fields, equation (A.8) takes the following form

$$\mathbf{J} \times \mathbf{B} = \sigma_o (\mathbf{E} + \mathbf{v}^\beta \times \mathbf{B}_o) \times \mathbf{B}_o, \quad (\text{A.9})$$

Equation (A.9) on using relation

$$(\mathbf{F} \times \mathbf{G}) \times \mathbf{H} = \mathbf{G}(\mathbf{F} \cdot \mathbf{H}) - \mathbf{F}(\mathbf{G} \cdot \mathbf{H}),$$

gives

$$\mathbf{J} \times \mathbf{B} = \sigma_o (\mathbf{B}_o (\mathbf{v}^\beta \cdot \mathbf{B}_o) - \mathbf{v}^\beta (\mathbf{B}_o \cdot \mathbf{B}_o)). \quad (\text{A.9})$$

Assuming velocity vector \mathbf{v}^β is perpendicular to the magnetic field lines B_o (i.e. $\mathbf{v}^\beta \cdot \mathbf{B}_o = 0$) and dimensional form of $\mathbf{B}_o = (0, B_o, 0)$, where B_o represents the strength of imposed magnetic field \mathbf{B}_o , equation (A.9) takes the following form

$$\mathbf{J} \times \mathbf{B} = -\sigma_o B_o^2 \mathbf{v}^\beta. \quad (\text{A.10})$$

Thus, conservation of the momentum (A.3) can be written as

$$\rho^\beta \left(\frac{\partial \mathbf{v}^\beta}{\partial t} + (\mathbf{v}^\beta \cdot \nabla) \mathbf{v}^\beta \right) = \nabla \cdot \mathbf{T}^\beta + \rho^\beta \mathbf{b}^\beta + \boldsymbol{\pi}^\beta - \sigma_o B_o^2 \mathbf{v}^\beta.$$

The conservation of the momentum equation (A.3) for the solid phase, on substituting the value of $\boldsymbol{\pi}^s$, gives

$$\rho^s \left(\frac{\partial \mathbf{v}^s}{\partial t} + (\mathbf{v}^s \cdot \nabla) \mathbf{v}^s \right) = \nabla \cdot \mathbf{T}^s + \rho^s \mathbf{b}^s + K (\mathbf{v}^f - \mathbf{v}^s) + p \nabla \phi^s - \sigma_o B_o^2 \mathbf{v}^s. \quad (\text{A.10})$$

Similarly, the conservation of the momentum equation (A.3) for the fluid phase, on substituting the value of $\boldsymbol{\pi}^s$, gives

$$\rho^f \left(\frac{\partial \mathbf{v}^f}{\partial t} + (\mathbf{v}^f \cdot \nabla) \mathbf{v}^f \right) = \nabla \cdot \mathbf{T}^f + \rho^f \mathbf{b}^f - K (\mathbf{v}^f - \mathbf{v}^s) - p \nabla \phi^s - \sigma_o B_o^2 \mathbf{v}^f. \quad (\text{A.11})$$